Towards the Spectroscopy of Giant Exoplanets with Nulling Interferometry: Fabrication & Characterisation of the Mid-Infrared 4-Telescope Photonic Beam Combiner of NOTT/VLTI

INAUGURAL-DISSERTATION

zur
Erlangung des Doktorgrades
der Mathematisch-Naturwissenschaftlichen Fakultät
der Universität zu Köln

vorgelegt von

Sayed Ahmed Islam Sanny
aus Dhaka, Bangladesch
Köln 2024

Towards the Spectroscopy of Giant Exoplanets with Nulling Interferometry: Fabrication & Characterisation of the Mid-Infrared 4-Telescope Photonic Beam Combiner of NOTT/VLTI

By

Sayed Ahmed Islam Sanny

A thesis submitted to Macquarie University
for the degree of Doctor of Philosophy
Faculty of Science and Engineering
School of Mathematical and Physical Sciences
October 2024

Typeset in LaTeX 2_ε.

This thesis is submitted to Macquarie University and University of Cologne in accordance with the Cotutelle agreement dated 01 March 2020.

To the best of my knowledge and belief, the thesis contains no material previously published or written by another person except where due reference is made in the thesis itself.

Sayed Ahmed Islam Sanny

Acknowledgements

I am fortunate to have had the opportunity to be part of two exceptional research groups at MQ Photonics Research Centre (Macquarie University, Australia) and Institute for Astrophysics (University of Cologne, Germany) as a Cotutelle PhD student. This experience has taken me across two continents of the planet Earth's north and south hemispheres to develop astrophotonic devices for the module NOTT of the upcoming visitor instrument ASGARD at the Very Large Telescope Interferometer (VLTI), aimed at detecting and characterizing exoplanets in the mid-infrared.

I extend my deepest gratitude to my supervisors, Lucas Labadie, Simon Gross, and Michael Withford, for entrusting me with the opportunity to work on this significant project under their guidance and unwavering support throughout my PhD journey. Their support was particularly invaluable during the disruptions caused by the COVID-19 global pandemic, which significantly affected my PhD timeline, rendering my journey quite unconventional. Once again, I thank Lucas Labadie for our daily discussions and Simon Gross for his invaluable comments and suggestions during the thesis writing process. Without their critical input, this thesis would not have been completed.

Moreover, I am grateful to the members of my cross-continental research groups, whom I encountered during my nearly four-year PhD journey. In particular, I would like to thank Marie, Alexander, Kevin, and Chinmaya for our varied conversations and activities at the University of Cologne. I thank Ben, Toney, and Thomas at Macquarie University for stimulating discussions during my stay in Sydney. There is a separate thanks to my friends Anita, Murtala, and Wei Ming. I am also thankful to my extended

collaborators from the ASGARD project and friends whom I met and lost outside of the work during the timeline of my PhD candidature.

Lastly, I wish to express my gratitude to my family and parents. I also thankfully remember my grandma, whom I lost a year before starting my PhD journey. Her memory remains a source of inspiration and motivation for me.

Abstract

Nulling Observations of exoplaneTs and dusT, or in short 'NOTT', is the first long-baseline self-calibrated nulling interferometer based on a photonic beam combiner as part of the upcoming visitor instrument ASGARD at the VLTI (Paranal, Chile). The NOTT instrument aims to detect and characterise young exoplanets in the mid-infrared astronomical L' band using nulling interferometry. The photonic or integrated optic beam combiner for NOTT is fabricated using Ultrafast Laser Inscription (ULI) in chalcogenide glass. ULI uses an ultrashort pulsed laser to form single-mode waveguides for the mid-infrared region within the bulk of the substrate. The integrated optics beam combiner follows the "Double-Bracewell" architecture and consists of three cascaded directional couplers with 50/50 achromatic splitting. The first two directional couplers produce a null signal each, which are then coherently combined by the central directional coupler. This central directional coupler creates two nulled signals with mirrored transmission maps, where their difference produces a self-calibrated astrophysical null. The beam combiner's unique 3D architecture allows each individual telescope beam to first pass through a side-step to suppress uncoupled stray light. Asymmetric Y-junctions then sample the corresponding flux to provide simultaneous photometric information for each input enabling the most accurate estimation of the null depth.

This thesis presents the step-by-step development and characterisation of directional couplers, Y-junctions, a 2-telescope beam combiner and up to NOTT's 4-telescope beam combiner, all fabricated in Gallium-Lanthanum-Sulphide (GLS) glass using ULI.

It includes the first detailed mid-infrared laboratory characterisation of such a photonic device using 4 beams across a wavelength band between 3.65 and 3.85 μm. Detailed characterisation and optimisation of the directional couplers has resulted in achromatic splitting ratio close to 50/50 across the L' band with good reproducibility. These directional couplers feature null depths in the range of 10^{-2} using polychromatic light from a supercontinuum source without any polarisation control. Y-junctions have been engineered for achromatic 50/50 splitting for the 2-telescope beam combiner and achromatic 20/80 splitting to meet the requirements for NOTT's 4-telescope beam combiner. For the 4-telescope beam combiner, a self-calibrated null of 10^{-4} is demonstrated within the limitation of the interferometric test bench at room temperature. The beam combiner will be installed in the NOTT instrument during the first deployment phase. Although the current 4T-Nuller falls slightly short of the ideal specifications, a second-generation beam combiner will eventually have to be fabricated to achieve all the instrument's science goals. This beam combiner will be building on the groundwork established by this thesis.

Contents

List of Figures

1

Introduction

> In space, there are countless constellations, suns and planets; we see only the suns because they give light; the planets remain invisible, for they are small and dark. There are also numberless earths (exoplanets) circling around their suns...
>
> Giordano Bruno [1548-1600]
>
> *Despre infinit univers si lumi* [1]

In recorded history, Giordano Bruno, well-known as the martyr of science, is probably the first person to think of exoplanets. Since then, exoplanets have become a quest in observational astronomy. However, it is only recently that instrumental development allowed human understanding of extrasolar planets and their planetary systems.

In particular, advances in the field of optics, such as integrated optics to adaptive optics, have enhanced the capability of exoplanet detection. According to the recent NASA Exoplanet Archive, by March 2024, the number of confirmed exoplanets is 5595 [2].

1.1 Exoplanet detection techniques

Exoplanet detection involves multiple techniques that are distinguishable based on the detection methods and characteristics of the planets. The first well-known technique is the *radial velocity method*. This pioneering technique relies on the periodic variation of the star relative to the centre of mass of the system, which appears as a Doppler shift in the spectral lines of a star induced by the gravitational influence of an orbiting exoplanet.

The radial velocity method confirmed the first official exoplanet discovery by Mayor & Queloz in 1995 that orbits a normal sun-like star [3]. Previously, the first exoplanet was discovered in 1992 and orbits around a pulser using the pulsar timing technique [4]. Even though the pulsar timing technique was not developed to detect planets, it is sensitive enough to detect exoplanets.

The second and most successful method is the *transit method*; this method involves monitoring the temporary dimming of the star's brightness as an exoplanet transits through its stellar disc. More than half of all detected planets have been discovered using this method [5; 6; 7].

Another technique is the *microlensing method*. It works based on the principle of gravitational lensing when a massive object, such as a planet, passes through and temporarily magnifies the light from a background star [8; 9]. Numerous additional techniques play pivotal roles in the detection of exoplanets. One such method is the *astrometry method*, devised initially to monitor minute shifts in a star's position, thereby detecting its motion. This technique has been extended to successfully identify planets orbiting a star by measuring subtle alterations in the star's position as it oscillates around the centre of mass of the planetary system [9].

However, these methods are based on indirect observations, even though they have successfully found planets, particularly the radial velocity and transiting methods. Unfortunately, most cannot provide spectral or direct radiation that can allow advanced analysis to understand the planet's properties or even biosignatures since there is an inherent bias from nearby planets or the host star [10]. Therefore, direct imaging of the reflected light or thermal radiation emitted by the planet is the best way to obtain a planetary spectrum. The *direct imaging method* involves capturing the faint light emitted or reflected by exoplanets. This is inherently challenging due to the overshining brightness of its host star[7]. Hence, only a tiny fraction of exoplanets, less than 50 out of 5595, have been confirmed using direct imaging to date [11].

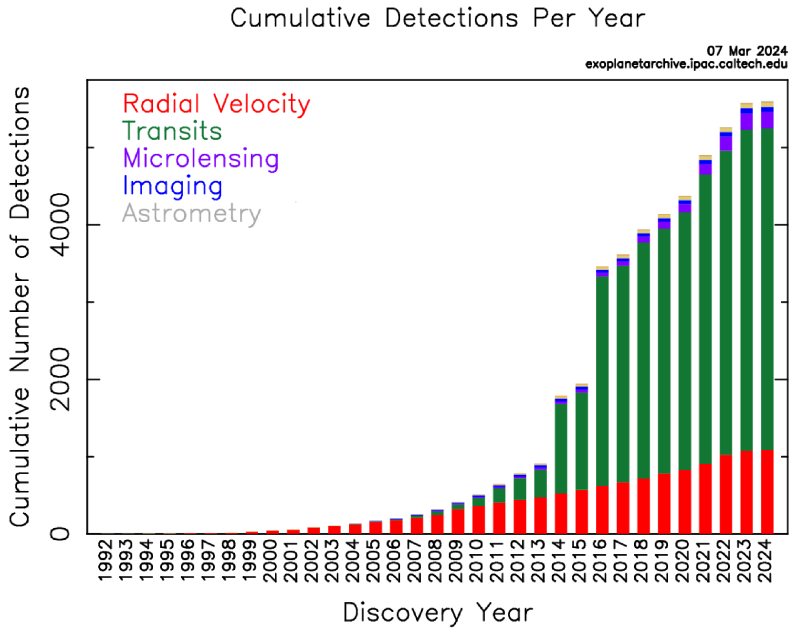

Figure 1.1: As per the latest data from the NASA Exoplanet Archive, as of March 2024, the number of confirmed exoplanets is 5595. The graph illustrates the cumulative number of detections using radial velocity, transit, microlensing, imaging, and astrometry methods. Image source: [2].

1.1.1 Direct imaging of exoplanets/VLTI

Direct imaging and high spectral resolution characterisation can reveal unique properties of exoplanets, including the composition of their atmosphere [12; 13; 14; 15], rotation [16; 17; 18], and cloud coverage [19].

Therefore, the advancement of imaging devices, characterised by a continuous enhancement in angular resolution, sensitivity, contrast, and ability to suppress the glare of the host star, holds the potential to guide scientific progress and discoveries of exoplanets. In this context, contrast refers to the reciprocal of the dynamic range, signifying the flux ratio of the least luminous object detectable by the instrument [20]. For that, two additional techniques are used – (i) coronagraphy, which involves masking the light from the star through the use of a focal plane mask, and (ii) nulling interferometry, which is a particular case of interferometry with the ability to block or null the host star light as is done with coronagraphy but without masking.

Contemporary coronagraphic imaging tools are extensively employed, combined with adaptive optics for direct imaging [10]; however, their effectiveness is constrained by contrast limitations within a few resolution elements from the central star. This limitation arises from a fixed inner working angle (IWA $\approx \lambda/D$). This is the angle of separation from the star, at which the flux from the planet is rapidly decreased and/or beyond which the flux from a resolved star rapidly increases. Typically, the contrast ranges from 10^{-4} to 10^{-5} at distances of several λ/D from the central star, depending on the wavelength. Here, λ represents the centre wavelength, and D denotes the diameter of the aperture integrated into the telescopic aperture [21; 10].

On the other hand, ground-based long baseline nulling interferometry shows significant advantages over coronagraphy; it allows probing of smaller spatial scales with modest contrast [20]. For instance, The Very Large Telescope Interferometer (VLTI), located in Paranal, Chile, is an astronomical facility specialising in high angular resolution astronomy under the support of the European Southern Observatory (ESO) in infrared. Figure 1.2 represents the VLTI observatory and the infrared transmittance window for the ground-based observatories, sub-divisioned by astronomical bands H, K, L, L', M and N. VLTI contains four 8.2-m Unit Telescopes (UTs) and four 1.8-m

Auxiliary Telescopes (ATs). The locations of UTs are fixed, while the ATs can be relocated to more than ten different positions [22]. This facility has played a crucial role in numerous astronomical discoveries and technological advancements, using a suite of famous and well-known instruments operating in the infrared.

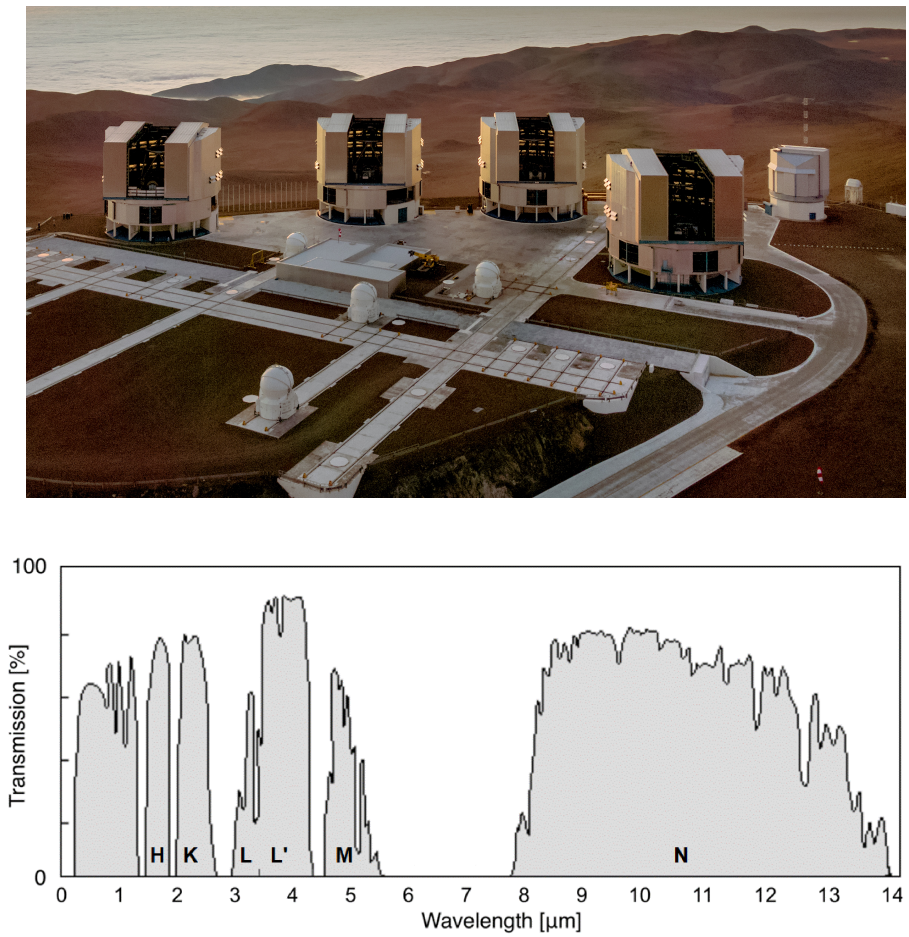

Figure 1.2: European Southern Observatory (ESO)'s VLTI at Paranal, Chile (upper) [22]. Illustration of the astronomical wavelength bands with respect to the infrared transmission of the Earth's atmosphere. The presence of extinctions is due to molecular absorption by water vapour, CO_2, etc [23] (lower).

As of 2024, MATISSE [24], GRAVITY [25], and PIONIER [26] are currently commissioned high contrast imaging instruments at VLTI. In the past, VLTI hosted, now decommissioned, high contrast imaging instruments AMBER, MIDI, PRIMA, and VINCI [27]. The VLTI achieved contrast in the near-infrared using PIONIER (H band)

and GRAVITY (K band) at the level of 10^{-3} within a few milliarcseconds (mas) angular resolution. However, nulling instruments located in the Northern hemisphere and non-redundant aperture masking observations, such as those conducted at CHARA, have demonstrated superior contrasts of approximately 10^{-4} on baselines longer than those currently accessible at the VLTI [28]. As depicted in Figure 1.3, it has been identified that compared to shorter wavelengths, the contrast ratio of young giant exoplanets to their host stars reaches 10^{-4} or 10 magnitudes, making direct imaging more feasible in the L' band. However, achieving this requires high angular resolution, which can only be accessed through the advantages offered by long baseline interferometry. Therefore, developing a high-contrast L' band nulling interferometry instrument for detecting extra-celestial bodies is highly prioritised for the future VLTI instrument [27].

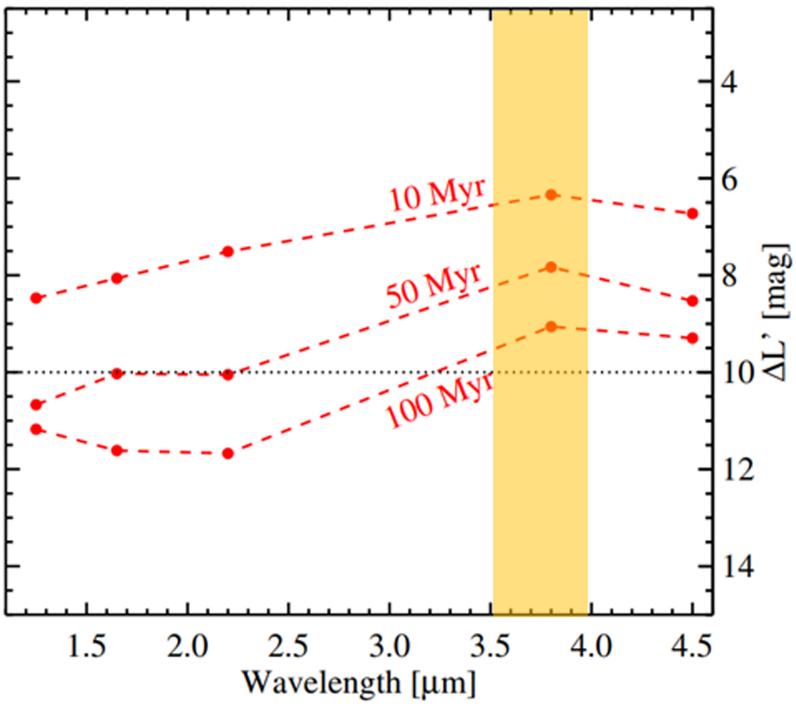

FIGURE 1.3: Simulated contrast between a 10 $M_{jupiter}$ planet and a 1 M star as a function of wavelengths depending on the planets age. The wavelength of the L' band provides improved contrasts over shorter wavelengths, particularly for young planets still hot from their formation. The dashed horizontal line represents the target contrast 10^{-4} or 10 Magnitudes for ASGARD/NOTT [20].

Recent innovations in technology, for example, adaptive optics [29], data reduction techniques like self-calibrating null depth estimation [30], beam combination architectures [31], and integrated optics[32], present promising pathways to elevate the VLTI to the next level of observational capability by providing enhanced contrast at smaller angular separations.

1.2 ASGARD: instrument overview

The VLTI: ASGARD initiative has been introduced as an innovative visitor instrument [33; 34], comprising four collaborative sub-instruments, namely HEIMDALLR (High-Efficiency Multiaxial Do-it-ALL Recombiner), BALDR (performing both fringe tracking and stellar interferometry with shared optics), BIFROST (Beam-combination Instrument for studying the Formation and fundamental paRameters of Stars and planeTary systems), and NOTT (Nulling Observations of dusT and planeTs), a nulling interferometer dedicated to imaging young nearby planetary systems in the L' band, formerly known as Hi-5 [35]. This NOTT instrument's heart is a 4-telescope integrated optics beam combiner. The focal point of this thesis is to construct such a device utilising the ultrafast laser inscription technique.

The operational range of ASGARD extends from Y to L band, covering wavelengths from 1 to 4 μm. Figure 1.4 shows the instrument overview and Figure 1.5 contains the optomechanical layout of the ASGARD instrument, while Table 1.1 lists the specifications of each ASGARD sub-modules.

Each of the sub-instruments of ASGARD contains multiple subsystems, as shown in Figure 1.4. However, they share two common modules - (i) ASGARD Calibration and Alignment Unit (ACAU), which includes the sources for the spectral calibration of the modules and a coherent 4-beam light source for internal alignment and co-phasing. It also provides flip mirror pickoffs to switch between ACAU and VLTI. (ii) ASGARD Common Optics (ACO) with a combination of four sub-modules - *shutters* with the ability to shut down all the instruments at once or one at a time, *beam compressors* is to reduce the size of beams with four pairs of optics, MEMS *deformable mirrors* to

perform fringe tracking and injection control as well as the correction of higher order aberration modes for maximising the injection efficiency in BIFROST and NOTT. *Dichroic* mirrors to transmit the L' band to NOTT and reflect shorter wavelengths to the other sub-instruments.

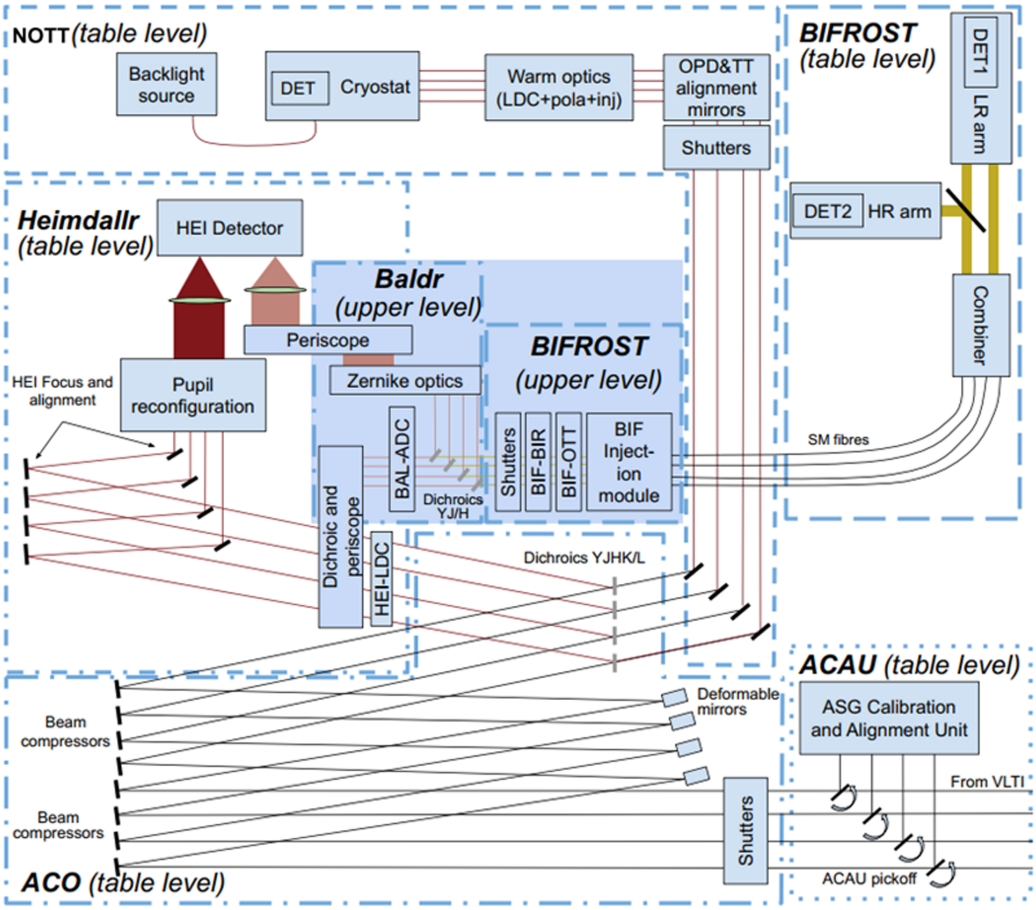

FIGURE 1.4: Schematic layout of the ASGARD instrument with its four sub-instruments and their modules. Image credit: [34].

The first sub-instrument, HEIMDALLR, incorporates several essential components. This includes the Longitudinal Dispersion Compensator (HEI-LDC), which features a piezoelectric linear stage mounted in each beam to introduce optical path delay. Additionally, the Focus and Alignment Mirrors (HEI-FA) consist of four mirror pairs steared by stepper motor actuators.

Furthermore, the Pupil Reconfiguration (HEI-COMB) component utilises knife-edge mirrors to reconfigure the K-band beams into a two-dimensional pattern for performing wavefront sensing using fringe patterns created by six non-redundant baselines on the detector. The Camera (HEI-DET) module contains the cooling systems, electronics, and detectors to collect and record fringe patterns and signals from the BALDR.

TABLE 1.1: Specifications of the VLTI /ASGARD modules [34; 33]

Feature	**HEIMDALLR**	**Baldr**	**BIFROST**	**NOTT**
Photometric band	K	H	Y, J, H	L
Central wavelength (μm)	2.18	1.6	1.35	3.75
Bandwidth (μm)	0.45	0.3	0.6	0.5
Spectral resolutions	R=5 (two channels)	None	LR arm (Y,J,H): R = 50, 100, 1500, 5000 HR arm (Y,J): R = 1000 (1.05-1.65 μm) HR: R=5000 (1.05-1.65 μm) VHR: R=25000 (around He I+Paβ and Paγ)	R = 20 R = 400 R = 2000*
Polarization split	NO	-	YES (optional)	YES*
Off-axis mode	-	-	YES*	-
Inner Working Angle @3.75 μm	-	-	-	2 mas (AT), 3 mas (UT)
Diameter of the field of view	250 mas (AT), 55 mas (UT)	183 mas (AT), 41 mas (UT)	155 mas (AT), 34 mas (UT)	430 mas (AT), 94 mas (UT)
Interferometric observable	V^2, closure phase	-	V^2, closure phase, differential phases	Null depth, differential null depth
Magnitude limit	K=11.5 (ATs) or 13.5 (UTs)	H=9.6 (ATs) or 12.9 (UTs)	Limited by Baldr	L'=11 (ATs) or 13 (UTs)

* Contingent on additional development.

BALDR, the second sub-instrument, has an Atmospheric Dispersion Compensation (BAL-ADC) unit that employs motorised rotary stages to rotate four pairs of prisms for mitigating chromatic dispersion effects between Y and H bands. This improves injection efficiencies and reduces differential phase errors between the wavelength bands.

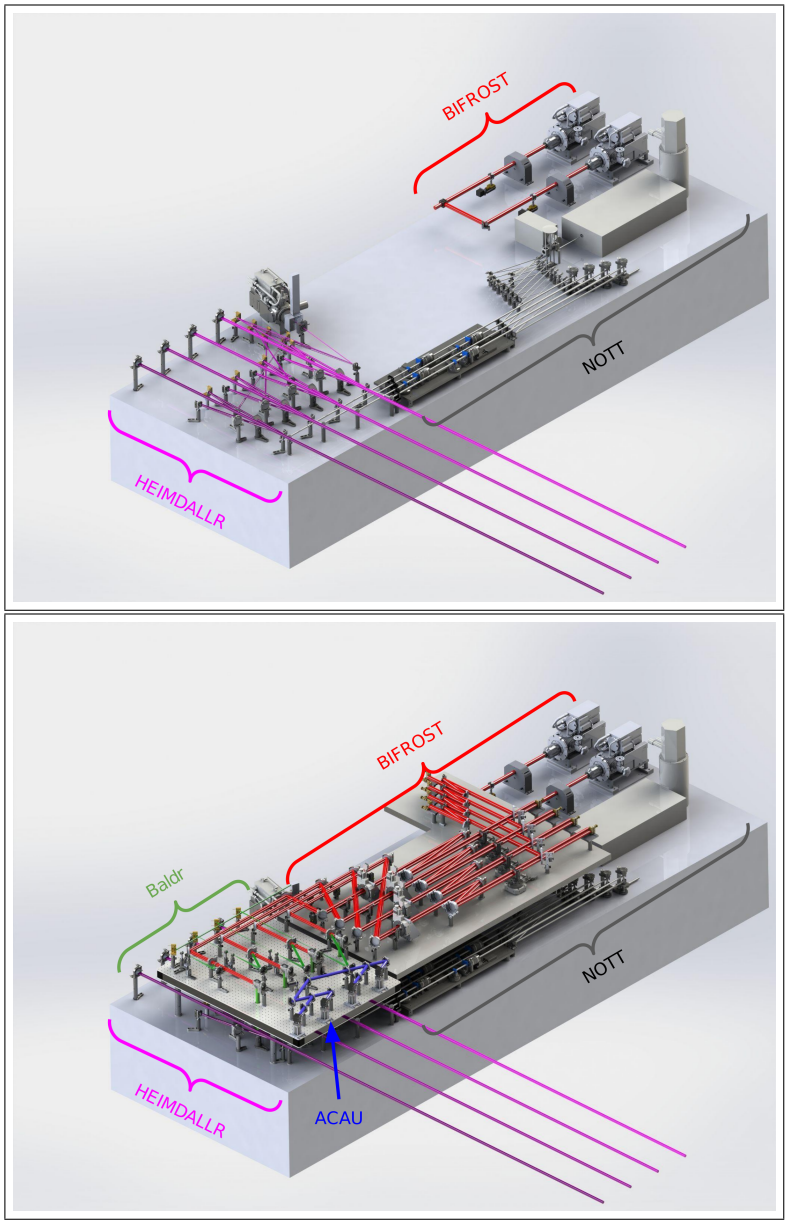

FIGURE 1.5: Optomechanical design of ASGARD: The optics are spread across two levels on the table. The upper image shows the lower level, and the lower image shows the complete design. The optical paths are coloured for each module: HEIMDALLR (purple), BIFROST (red), NOTT (grey), BALDR (green), and ACAU (blue), which stands for Asgard Calibration and Alignment Unit. Image credit: [34].

The Beam Splitter (BAL-DIC) reflects the H-band to BALDR and transmits the J and Y bands to BIFROST. The Zernike Optics (BAL-ZER) serves as the wavefront sensor, incorporating phase masks or photonic lanterns to decompose wavefronts on a Zernike aberration base. Last, the Periscope (BAL-PER) directs signals from BALDR to HEIMDALLR's camera.

The third sub-instrument, BIFROST, encompasses several key components. The Shutters (BIF-SHUT) consist of four shutters capable of individually blocking each beam or collectively performing calibration tasks and protecting detectors from strong light when BIFROST is inactive. Birefringence Correction (BIF-BIR) utilises $LiNbO_3$ plates mounted on motorised rotary stages to compensate for birefringence in the beam path, enabling for maximising the interferometric contrast within BIFROST. OPD & TT Alignment Mirrors (BIF-OTT) ensure the co-phasing of the input beams between BIFROST and HEIMDALLR and optimise light injection into BIFROST's Injection Module (BIF-INJ). This includes a differential delay line mirror for co-phasing BIFROST with ASGARD and a tip-tilt fast steering mirrors for active optimisation of optical fiber coupling. The Injection Module incorporates off-axis parabolic mirrors and single-mode optical fibers to transport light to BIFROST's core.

Additionally, the Combiner (BIF-COMB) facilitates coherently combination of the four beams, featuring a 90/10 beam splitter for simultaneous data recording with BIFROST's LR and HR arms. The Low-Resolution arm (BIF-LR) includes imaging optics, a prism for low-spectral dispersion, a camera, and a Wollaston prism for polarisation state measurement and visibility calibration. Its camera collects low-dispersed fringe patterns and photometry signals. Similarly, the High-Resolution arm (BIF-HR) comprises imaging optics, a filter wheel with prisms for high spectral dispersion, and a camera primarily used for measuring wavelength-differential quantities and closure phases.

The NOTT sub-instrument, NOTT, contains the beam conditioner (NOTT-SHUT), which includes shutters and diaphragms. It blocks beams individually and equalises the intensities for calibration and to optimise the null depth. Optical Path Difference OPD and Tip-Tilt alignment mirrors (NOTT-OTT) co-phase the beams between

HEIMDALLR and NOTT to optimise the light injection into the 4-telescope integrated optics beam combiner, in this thesis simply referred to as 4T-Nuller. The combined beams go through the NOTT-warm optics containing longitudinal dispersion compensator (LDC), polarisation control optics, the slicer, and the alignment camera. LDC uses a feedback loop to compensate for the chromatic phase across the L' band and compensate for water vapour effects. The Polariser balances the polarisation effects to improve the instrumental null depth. The arrangement involves positioning the slicer to align the four telescope pupils onto the cold stop located at the entrance of the NOTT cryostat (NOTT-CRYO). The cryostat contains a window, a cold stop, the NOTT integrated optics beam combiner, a spectrograph and imaging optics, the camera (NOTT-DET), the cryocooler, and the vacuum system. Different prisms are available for different spectral resolutions in the spectrograph. The camera collects the spectrally dispersed signal that emerges from the photonic beam combiner. NOTT can compensate for fringe drifts due to water vapour and CO_2 by relying on simultaneous analysis of its signal with wavefront analysis of HEIMDALLR and the telemetry of BIFROST. The advantage of such a layout is that HEIMDALLR and BALDER can operate simultaneously with either BIFROST or NOTT.

The instrumental overview and operational details presented above are sourced from the work of Martinod *et al.* [34]. Reference [34] details the current project plan for ASGARD.

1.3 ASGARD/NOTT: science quest

The science cases for ASGARD revolve around stellar physics and exoplanetary science [33; 36]. HEIMDALLR and BALDR primarily address atmospheric aberrations and atmospheric pistons, while BIFROST and NOTT are science-driven.

At the initial operation phase, ASGARD will start observation based on the available astronomical datasets regarding steller physics and extragalactic astrophysics, and then it will focus on new surveying. The Gaia mission provides approximately 813,000

non-single star systems (data release 3 [37]), where 357,000 systems are binary. However, the available angular resolution (0.1 arcsecond) of Gaia is insufficient to spatially resolve most of these systems, which leads to a degeneracy between the flux ratio of the stellar objects and their separation. BIFROST and HEIMDALLR aim to spatially resolve and characterise up to 6,000 binaries among these 357,000 systems via measuring interferometric visibilities, closure phases, and differential phases in the K band and Y/J band, respectively [36]. The extensive study can provide access to the ages of the stars, which is essential for galactic archaeology studies. Harnessing the high resolution (HR) spectroscopy mode of BIFROST with a resolving power of R = 25,000 will allow for measuring the stellar spin orientation of moderate/slow rotating stars. BIFROST will also be used to study the mass accretion and ejection process of young stellar objects (YSO), active galactic nuclei (AGN) [36; 38], accretion disks of T Tauri stars[37], gas dynamics around Herbie Ae/Be stars[39], wind-wind collision in luminous-blue variables stars[40], and relativistic jets of micro-quasars[41].

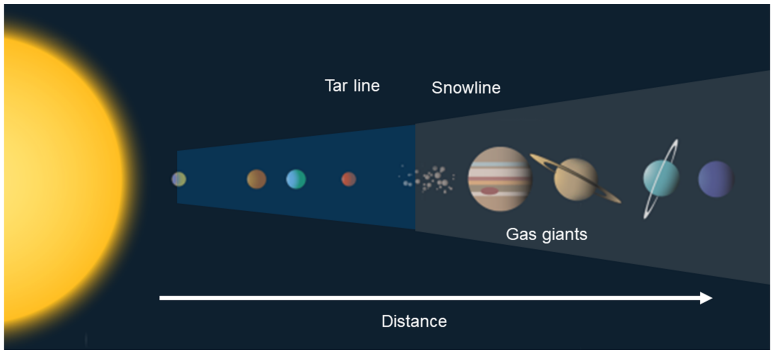

FIGURE 1.6: Schematic diagram based on our solar system, showing gas giants within the snowline, a region in the solar system located at a distance from the host star where water and other volatile molecules condense into their icy forms. Conversely, the region closer to the star, where water exists in its vapour state, is referred to as the Tar line [42].

ASGARD/NOTT aims to explore exoplanetary science, which will start by detecting exoplanets within the snowline of its planetary system to characterise chemical composition using 4-telescopes of VLTI by implementing the technique called self-calibrated nulling interferometry where the subtraction of the nulled outputs is used to measure a null that is less sensitive to phase excursions, which classically encountered

in long-baseline interferometry from the ground [20; 43; 44; 45]. Figure 1.6 depicts the snowline's location and definition.

In operation, NOTT will be employed to understand the formation and evolution of exoplanetary systems and atmospheres of giant exoplanets, ones that already have been discovered by non-direct imaging techniques or ones expected to be found soon. For instance, Gaia suggested that $\sim 25\%$ of planets are more massive than ~ 0.3 $M_{Jupiter}$ and located in uncharted territory, particularly close to the water/ice or snowline line. This region is inaccessible for current direct-imaging instruments and upcoming instruments proposed for the Extremely Large Telescopes (ELTs) [46; 47]. NOTT will provide more information by measuring effective temperature to constrain the models of their formation more accurately [48]. Nearly 1500 young stars (< 250 Myr) within 150 pc are currently in the target list of NOTT.

By using Monte-Carlo simulations and end-to-end simulations [49; 43; 50], NOTT is also expected to detect 5-10 giant exoplanets from a list of $\approx$ 20 stars best star candidates, depending on the planet-formations models such as core accretion or gravitational instability. In addition, the spectroscopic maturity of NOTT will lead to the detection of the thermal emissions and absorption opacities from molecular bands and clouds [33]. The off-axis mode of BIFROST can be used to probe the atmospheres of these giant exoplanets [36]. Critical optical information, for example, non-equilibrium atmospheric chemical composition and their dynamics, vertical temperature profiles, spinning rates, and formation process, can be determined from such observations.

Protoplanetary disks exhibit diverse structures, including rings, gaps, spirals, and large cavities, offering valuable insights into the formation process. The frequently observed large cavities, often exceeding 20 astronomical units (AU), are present in approximately 10% of all disks [51]. They display asymmetric features such as spirals or vortices, indicative of companions that result in cavity carving [52; 53].

NOTT observations are envisioned to contribute novel data for hydrodynamical models, enhancing the understanding of planet-disk interactions and providing constraints on planet formation and early-stage evolution.

Leveraging its high-contrast nulling mode in combination with the long VLTI baselines, NOTT will facilitate the observation of transition-disk cavities at shorter wavelengths, which is currently inaccessible by other single-telescope instruments operating in L-band or other exoplanet imagers under the projects initiated under the umbrella of Spectro-Polarimetric High-Contrast Exoplanet REsearch (SPHERE) [54].

Furthermore, NOTT-based image reconstruction capabilities will enable a detailed examination of dust origin through its distribution, complementing the study of structures indicative of the planet-disk interaction [33].

Exozodiacal dust, situated in the inner regions of main-sequence planetary systems near the habitable zone and closer, holds great scientific significance but poses a challenge for future observations such as imaging surveys for exo-Earths and the spectroscopic search for biosignatures in their atmospheres [55]. Scientifically, this dust serves as a tracer, offering insights into the architecture, dynamics, and evolution of the planetary and planetesimal system it inhabits [56; 57; 58; 59].

In Earth-like exoplanet imaging, dust in the habitable zone introduces photon noise and causes potential confusion from disk structures. Exozodiacal dust is particularly challenging to detect due to the low dust-to-star contrast compared to scattered light, and thus far, it is detectable only in thermal emission [60]. The emission from the dust is not even strong enough for photometric detection. So, it requires high sensitivity [61].

Nulling interferometry on VLTI using NOTT is anticipated to provide a ten-fold increase in sensitivity to extended circumstellar emission compared to other stellar interferometers like the Precision Integrated-Optics Near-infrared Imaging ExpeRiment (PIONIER) of VLTI and Fiber Linked Unit for Optical Recombination (FLUOR) of CHARA [26; 62; 63].

Additionally, the dust-to-star contrast is approximately five times more favourable in the L' band compared to the H band [64]. Similar to the procedure accomplished with PIONIER/VLTI [62], NOTT will rely on high-contrast circumstellar emission detection using a polarization corrector on the VLTI auxiliary telescopes (AT).

1.4 Thesis outline

At the heart of NOTT lies the integrated optics (IO) beam combiner. This thesis describes the development of this beam combiner, driven by the ASGARD's requirements. The primary aim is to create a *deliverable* 4-telescope beam combiner, named 4T-Nuller, to enable nulling interferometry for ASGARD/NOTT. This endeavour forms the central pillar of this Cotutelle PhD dissertation, which is dedicated to development, fabrication and characterisation of a photonic chip based on a mid-infrared transparent Gallium Lanthanum Sulphide (GLS) glass substrate by holding the deliverable objectives as follows in Table 1.2

TABLE 1.2: Key photonic requirements for the ASGARD/NOTT [35; 33; 65; 34].

On-chip waveguides	Operational range	3.5-4.0 μm (GLS glass)
	Mode-field profile	Single-mode
Y-junctions	Splitting for photometric tap	20/80*
	Chromaticity	Achromatic
Directional couplers	Splitting for beam combination	50/50*
	Chromaticity	Achromatic
	Phase shift between two outputs	180 degree
4T-Nuller	Optical throughput	$\approx$ 50%**
	Contrast level (raw and self-cal.)	$10^{-2} - 10^{-5}$

* The splitting values should closely match those discussed in this table. However, slight deviations from the ideal specifications are anticipated experimentally. To address these deviations, parallel simulation packages, called SCIFYsim, are being developed at KU Leuven to establish their influence on the instrument's science capability and appropriate post-processing algorithms will be developed to mitigate their effects [43].

** Without Fresnel loss

The first half of Chapter 2 delves into the theoretical underpinnings of astronomical interferometry and then narrows down to nulling interferometry. The second half provides a background on the evolving field of astrophotonics and Ultrafast Laser Inscription (ULI) employed to fabricate waveguides for the NOTT beam combiner.

Chapter 3 covers two aspects. First, it discusses the fabrication setup and procedure, including pre- and post-processing of the photonic chips. Second, it demonstrates two characterisation setups that were employed to characterise the photonic waveguides for beam combiners.

Following that, Chapter 4 introduces the on-chip building block elements used to construct 4-telescope beam combiners for nulling interferometry. This chapter also highlights the photonic requirements for ASGARD/NOTT. Then, the relative optical throughputs of the waveguides are discussed. GLS glass materials contain some defects, and these defects are reported at the end of this chapter.

Chapter 5 explains the achromatic Y-junctions as a splitter for ULI. The results of incorporating Y-junctions with nulling beam combiners are discussed next. Then, the optimisation process to develop new Y-junctions for future nulling beam combiners is demonstrated, which will meet the project's requirements.

In Chapter 6, directional couplers are discussed for integrated optics and then the development phases of fabrication are discussed, which include optimisation with iteration to achieve required achromatic splitting ratios, a key requirement for nulling beam combination.

Nulling interferometry with a 2-telescope beam combiner and 4-telescope beam combiner (NOTT) has been performed in a lab environment and reported in Chapter 7 and Chapter 8, respectively. However, this chapter also contains the necessary theoretical discussion, including the procedure required/developed to obtain nulling measurements at the beginning.

Finally, Chapter 9 concludes with a comparison summary between the results obtained from the work of this thesis and the photonic requirements of ASGARD/NOTT. In the end, a guideline for future upgrades is also included.

2

Background

This chapter aims to provide a comprehensive discussion on the link between astronomical interferometry to nulling interferometry and the growing field known as astrophotonics, with a specific emphasis on Ultrafast Laser Inscription (ULI) of waveguides and mid-infrared optical material for manufacturing ASGARD/NOTT beam combiners.

2.1 Astronomical Interferometry

Long-baseline interferometry is an astronomical observation technique that allows a coherent combination of signals from multiple telescopes. Such a technique exceeds the angular resolution of a single telescope. The van Cittert-Zernike (VCZ) theorem, developed between 1934 and 1939 by Pieter Hendrik van Cittert and Frits Zernike, is the fundamental concept employed in astronomical interferometry, which provides a

mathematical framework for understanding how the mutual coherence of light, or more general electromagnetic waves, from a distant source can be related to the observed interference. The whole mechanism has been used dominantly by radio astronomers since the 1950s. However, a simplified version can be introduced to explain the basic idea with the help of various interpretations and implementations from researchers [66; 67; 68; 69; 70; 71; 72]

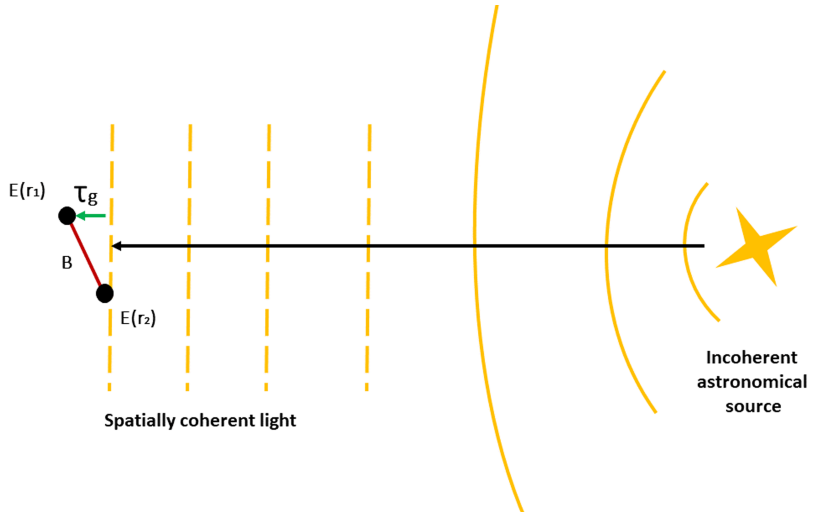

Figure 2.1: Representation of the basic principle of astronomical interferometry with the help of the VCZ theorem. An astronomical source, portrayed as a star that emits an incoherent electrical field $E(r)$, is observed by two telescopes situated at distinct locations r_1 and r_2 along a long baseline B. The detected signals, denoted as $E(r_1)$ and $E(r_2)$, are treated as plane waves due to the substantial separation from the source. The geometric delay τ_g represents the temporal gap between the reception of the signals.

The emission of an astronomical source is considered spatially incoherent if the radiation field is not heavily affected by the atmosphere of the Earth or scintillation in the atmospheric medium of the Earth. Now, by following Figure 2.1, a source can be considered. $E(r)$ is its emitted electrical field that is received by the two telescope apertures, which are separated by the baseline B between the points at a distance from the source of r_1 and r_2, respectively. The electric field is assumed to be a plane wave due to the fact that the source is in the far-field. The term 'mutual spatial coherence function' is usually used to describe it in more detail, which is equivalent to complex visibility $V(r_1, r_2)$.

However, for the electric fields, $E(r_1)$ and $E(r_2)$, received by the two telescopes, it can be expected that due to the positional displacement or the angle of the baseline with respect to the object, there will be a geometric delay stated as $\tau_g \approx B/c$, where c is the speed of light [73]. Hereafter, the measured electric fields from the two points will contain a phase difference between the measured signals, which results in constructive or destructive interference depending on the relative position of the two measurement points and the frequency f or wavelength λ at which the emitted radiation is observed. This phase difference is constant for any relative spatial difference and is expressed as $\phi = 2\pi f \tau_g = 2\pi/\lambda$.

In addition, the positional coordinates of the two apertures can be extended into a three-dimensional format as $B = \vec{r_1} - \vec{r_2} \approx (x_1 - x_2, y_1 - y_2, z_1 - z_2) \approx (u, v, w)$, where u, v, w can be considered as positional coordinates of B. Similarly, the sky intensity distribution in 3D can be considered as $I_v(l, m, n) = \langle E(r) \rangle^2$, when (l, m, n) is the normalised coordinate of the source that satisfies the relation $l^2 + m^2 + n^2 = 1$.

In such circumstances, the complex visibility of the transmission map, $V(\vec{r_1}, \vec{r_2}) = \langle E(r_1) E(r_2)^* \rangle$, where $\langle E(r_1) E(r_2)^* \rangle$ is the time-average correlation between the received signals, and this relation can extend for the 3D system according to the VCZ theorem using Equation (2.1).

$$V(u, v, w) = \int_{-\infty}^{\infty} \int_{-\infty}^{\infty} I_v(l, m, n) \frac{e^{-i2\pi(ul+vm+wn)}}{\sqrt{1 - l^2 - m^2}} \, dl \, dm \; = \mathcal{F}\{I_v(l, m, n)\} \tag{2.1}$$

During astronomical observation, Equation (2.1) is used in the form of Equation (2.2) by approximating for 2D transmission map using $w = 0$ and $l, m << 1$ because in 2D observation the observed area on the sky is pretty small, thus $n \approx 1$ holds.

$$V(u, v) = \int_{-\infty}^{\infty} \int_{-\infty}^{\infty} I_v(l, m) e^{-i2\pi(ul+vm)} \, dl \, dm \; = \mathcal{F}\{I_v(l, m)\} \tag{2.2}$$

In practice, when processing interferometric data, the complex visibility function is first identified, and then mathematically an inverse Fourier transform is performed, as both equations 2.1 and 2.2 contain Fourier properties. This leads to identifying the

information on the spatial coherence of the observed source. However, the resolving power or the angular resolution is limited by diffraction to $\approx \lambda/B$. How the light is combined from the two apertures to measure the complex visibility is discussed in Chapter 7.

2.1.1 Nulling interferometry

The concept of astronomical interferometry is further expanded by applying nulling interferometry, a technique initially proposed by Bracewell in 1978 for detecting exoplanets using a two-telescope rotating system [74]. The concept has undergone significant refinement since its inception. Nulling interferometry introduces a crucial modification to conventional interferometric procedures by incorporating an additional π-phase shift, as illustrated in Figure 2.2.

In traditional interferometry, spatially incoherent light of a source is detected and combined to create interference using telescopes, where the on-axis object, such as a star, experiences constructive interference at the image plane. However, in the case of nulling interferometry, an intentional π-phase shift is introduced before beam combination, which ensures that on-axis light experiences destructive interference, leading to the starlight cancellation at the centre of the interferometric image plane.

Conversely, light originating from an off-axis source carries a phase shift due to the non-coaxial angle of incidence. This facilitates the isolation of light emanating from nearby companions, such as planets or other faint sources like exozodial disks, effectively separating it from the strong stellar signal. However, the on-sky transmission map depends on the telescopes' arrangement. Figure 2.3 shows the telescope or aperture configurations and angular receive characteristics for a three- and four-telescope formation. A central null, N, can be written as $N \propto (\pi B \phi/\lambda)^2$ for all aperture configurations when ϕ is the off-axis angle and λ is a single wavelength [75]. Unlike coronagraphs, nulling interferometry does not impose a strict limit on the effective inner working angle. Instead, it allows the continued resolution of spatial structures much closer to the star, even with a reduction in the achievable contrast [76].

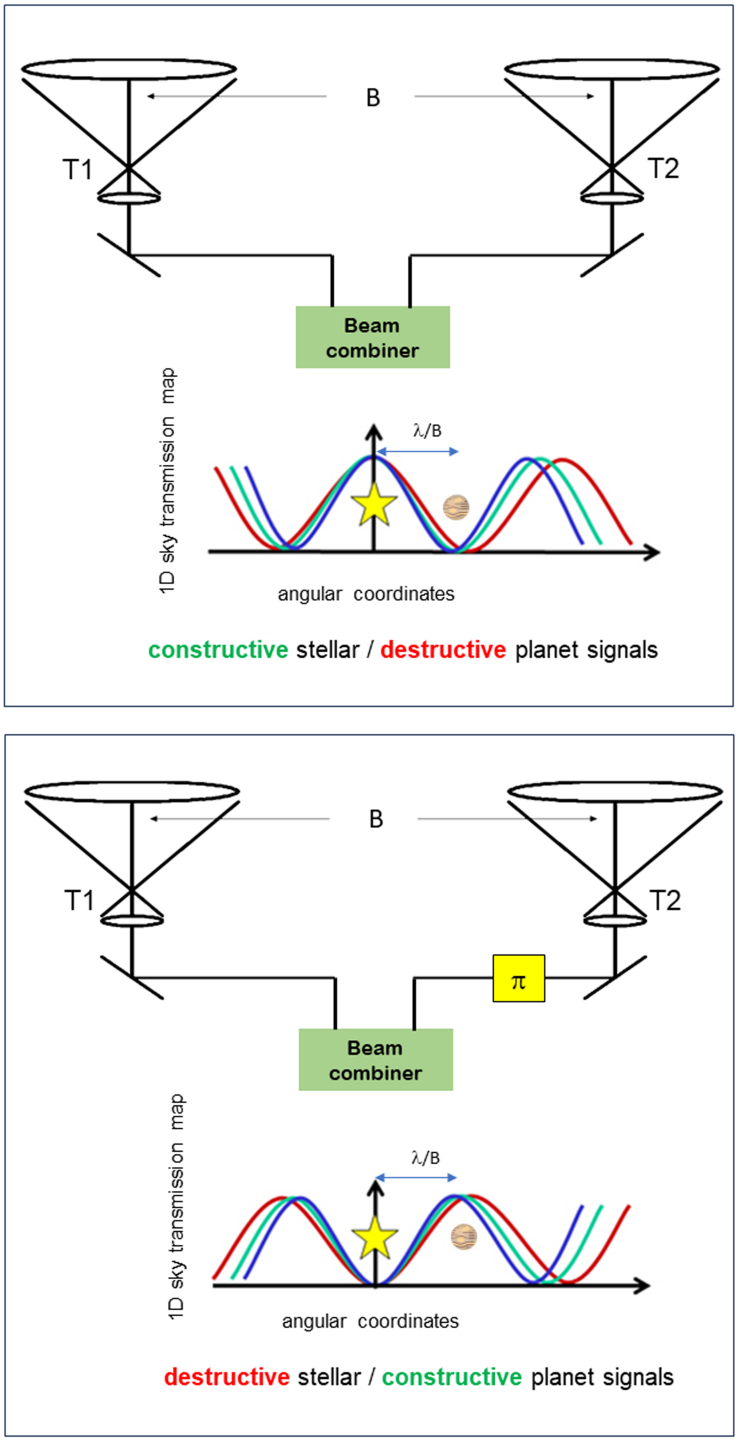

FIGURE 2.2: A comparison of conventional stellar interferometry (upper) and nulling interferometry (lower). In the conventional setup, signals from telescopes $T1$ and $T2$, separated by the baseline B, are combined using a beam combiner, which can be a simple 50/50 beam splitter, generating a 1D sky transmission map with polychromatic constructive fringes isolating most signals from the stellar object. In this case, a planet's signal falls into a destructive fringe if separated by an angular distance of λ/B. In contrast, nulling interferometry introduces an additional phase shift of ϕ in one arm before the beam combiner, thus shifting the destructive interference to the star and positioning a constructive fringe on the planet.

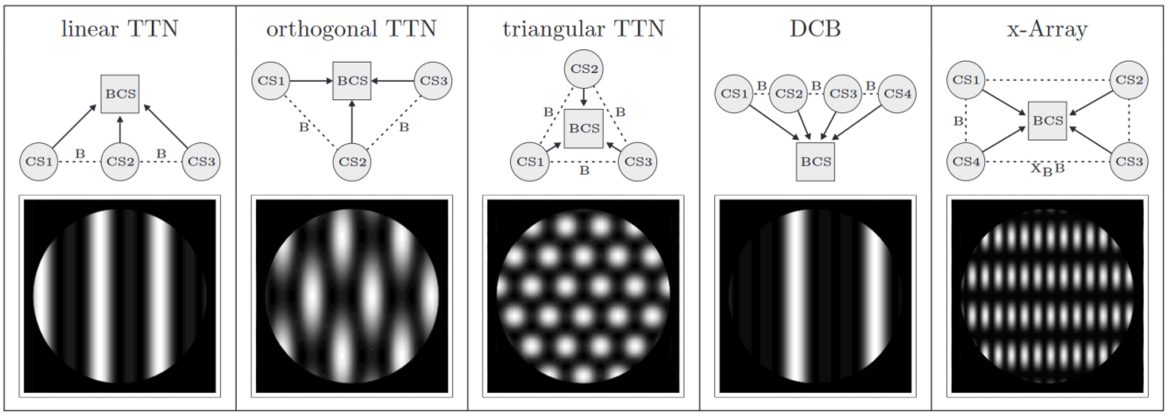

Figure 2.3: Examples of on-sky transmission maps of nulling interferometers based on satellites with different geometric arrangements of the spacecrafts. When the Collector Spacecraft (CS) are separated by the Baseline (B), and the received signals are combined using a Beam Combiner Spacecraft (BCS), then different arrangements such as Three Telescope Nuller (TTN), Dual Chopped Bracewell (DCB) or X-array with $X_B B$ can produce the following transmission maps depicted in the bottom row. Image credit: [75; 77]

The key observable in nulling interferometry is the source null depth, representing the ratio of destructive to constructive interference intensities. This metric quantifies the extent of light suppression attributable to the source's spatial brightness distribution. While the source null depth is retrieved through the processing of the measured data, it is subject to bias from instrumental responses and seeing-induced effects. The precision of its measurement is influenced by fluctuations from various sources, including atmospheric conditions, vibrations, and detector noise.

Precision enhancement can be achieved by applying statistical data analysis and fitting methodologies, which are discussed in Chapter 7, where the interferometric performances of the 2-telescope beam combiner are presented.

2.1.2 Nulling instruments

Over the past decades, several notable conceptual ideas have been proposed for high angular resolution imaging in space using nulling interferometry [78; 79], together with

in-depth theoretical studies focusing on instrumental effects, such as spectral dispersion and polarisation, over the nulled signal [80]. In the past two and half decades, various nulling interferometry-based instruments have been deployed on-sky at terrestrial telescopes. These instruments have either used masks to sub-divide a single telescope's pupil into multiple sub-apertures or used multiple individual telescopes for long-baseline interferometry. Pioneering instruments in this domain include the Bracewell Infrared Nulling Cryostat (BLINC) [81], the Keck Interferometer Nuller (KIN) [82], the Palomar Fiber Nuller (PFN) [30], the Large Binocular Telescope Interferometer (LBTI) [83], and the DRAGONFLY/GLINT instrument on Subaru/SCExAO [84]. With the exception of PFN and GLINT, these instruments operate predominantly at mid-infrared wavelengths between 8 to 14 μm, where dust in habitable zones of stars is prominent and atmosphere-induced phase instability is more manageable compared to shorter wavelengths [20].

These instruments have yielded significant scientific findings. For instance, KIN, which utilised both 10 m Keck Telescopes, conducted a comprehensive survey of exozodiacal dust around 47 stars in the astronomical N band [85]. More recently, the LBTI, as part of the HOSTS survey, explored the presence of dust closer to the habitable zone of nearby stars, also in the N band. This investigation is crucial for future activities in Earth-like exoplanet imaging [86].

Both, KIN and LBTI rely on conventional bulk optics. In contrast, PFN utilised the spatial filtering properties of single-mode optical fibers to enhance the instrumental null depth. It combined light from two sub-apertures of the 5.1 m Palomar Telescope in the K band and introduced the numerical self-calibration method (NSC) [87].

NSC involves the analysis of statistical fluctuations in the measured null depth to deduce the underlying source null depth, providing the precision necessary to detect faint companions in binary systems [88] and components of disks around stars, for example, AB Aur [89].

GLINT (Guided-Light Interferometric Nulling Technology) performs all beam combination operations within a compact photonic chip [90]. An earlier prototype of this was tested at the Anglo-Australian Telescope in Australia, focusing on studying the

performance of the photonic technology itself under seeing-limited conditions [91].

The final GLINT device has been integrated into the Subaru Coronagraphic Extreme Adaptive Optics system (SCExAO) at the Subaru Telescope. GLINT takes advantage of wavefront correction provided by the adaptive optics (AO) system [92]. It is the first photonic instrument capable of nulling multiple baselines simultaneously, with the additional capability of simultaneous photometric monitoring for each beam.

GLINT serves as a model for the design of highly capable, scalable instruments suitable for future large telescopes like the Extremely Large Telescope (ELT) or Thirty-Metre Telescope (TMT), as well as for long baseline interferometers such as ASGARD/NOTT.

Photonic chips facilitate the realisation of advanced architectures, including the multi-tier combiner [79] or kernel-nulling [45; 93], aiming for robust performance against the time-varying instrumental phase. Several novel interferometer architectures have emerged to enhance the performance of nulling interferometers in active nulling instruments.

Among the architectural concepts, one allows closure-phase measurements from nulled outputs [31], and another, called *kernel nulling* [45]. These concepts involve combining the outputs of a first nulling stage in a second mixing stage, with the aim of creating an output signal more resilient to imperfect co-phasing of incoming stellar light.

Some other innovative techniques appeared to be quite beneficial, involving a diffraction grating to adjust the light phase and achieve achromatic destructive interference at the tip of a single-mode fiber such as the Vortex Fiber Nuller [94], or using a symmetric beam combination scheme that is insensitive to polarization states, i.e., the Cross Cube Nuller [95].

Some applications of those techniques are explored, for example, simultaneous photometry detection and correction. However, this progress directly fuels the inspiration for developing cascaded or multi-stage on-chip nulling beam combiners, like the one for ASGARD/NOTT.

2.2 Astrophotonics

Astrophotonics, broadly defined, involves the application of photonic technologies to astronomical instrumentation, utilising the advantages of optical fibres and waveguides to manipulate and control light for astronomical observations. Within this domain, Integrated Optics (IO) emerges as a specialised discipline that focuses on miniaturising and integrating optical components onto a single photonic chip, offering the potential for increased stability and efficiency within a compact dimension.

Photonic devices like beam combiners, enabled by astrophotonics' advancement, play a crucial role in creating the intricate interference patterns essential for interferometry and nulling. Integrated Optics (IO) takes this integration a step further by consolidating multiple optical components onto a single chip. This miniaturisation enhances stability and precision in comparison to the typical bulk optics architecture.

Traditionally, integrated optics are fabricated using lithography, in which a geometric pattern is created by exposing the light-sensitive substrate through a previously manufactured photomask, followed by etching to create waveguides on a substrate.

Lithography, leveraging mature technology from the electronics industry, offers advantages for mass fabrication. Multiple fabrication techniques are used in lithography [96]. However, lithography's compatibility is limited to a narrower range of materials, and the requirements for many sequential processing steps do not lend lithography for rapid prototyping. Furthermore, waveguides fabricated using lithography are planar, which necessitates waveguide crossings. These crossings result in crosstalk, which is disadvantageous when the fabricated IO devices require the highest possible contrast. Herein lies the significance of Ultrafast Laser Inscription (ULI), which offers a broader selection of materials and facilitates rapid iteration through various device designs. Additionally, ULI enables three-dimensional fabrication, eliminating the need for waveguide crossings [97]. All of this makes it a suitable technique for fabricating photonic devices for the ASGARD/NOTT.

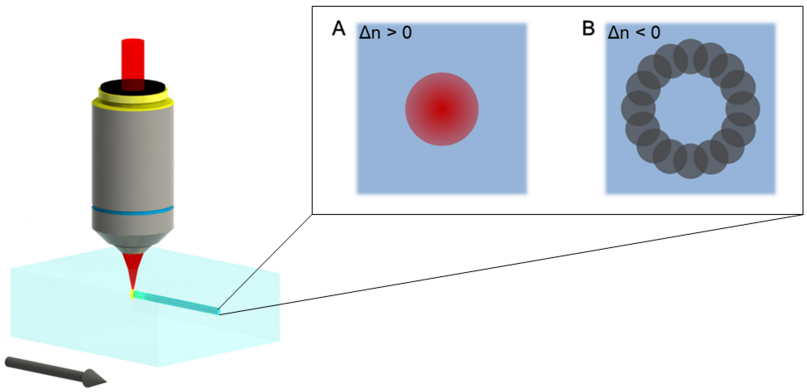

Figure 2.4: Ultrafast Laser Inscription of a waveguide inside a glass sample. The arrow denotes the translation direction of the sample with respect to the stationary laser focus. The zoomed-in cross-section of the inscribed waveguide reveals specific details: (A) illustrates a regular waveguide with a laser-inscribed core characterized by a positive refractive index change, while (B) depicts a depressed cladding waveguide that features a laser-inscribed cladding of negative refractive change. Image source: [97]

2.2.1 Ultrafast laser inscription

The Ultrafast Laser Inscription (ULI) manufacturing process features a femtosecond pulsed laser that is be tightly focused below the surface of the substrate, usually to a depth of a few hundred μm. This process introduces a permanent localised structural change in the material, which manifests itself as either a positive or negative change in the refractive index by an amount of Δn within the focal volume of the beam. Moving the substrate during irradiation makes it possible to inscribe arbitrary lines of refractive index change in three dimensions. When the laser causes a positive refractive index change, it creates the core of a waveguide similar to the core of an optical fibre. Conversely, if the laser induces a negative change in refractive index, one can resort to inscribing the cladding of a waveguide, effectively surrounding a cylindrical core with laser modified volume of lower refractive index. In this scenario, the core itself remains largely unaffected by the laser. Figure 2.4 shows an illustration of the process.

The structural transformation of the material under the influence of high laser intensities involves three sequential steps: the initiation of free electron plasma, the subsequent relaxation of energy, and the consequential modification of the material.

The initial phase, generating a free electron plasma, is comprehensively understood and comprises three key nonlinear processes: multiphoton ionisation, tunnelling photoionisation, and avalanche photoionisation, as depicted in Figure 2.5.

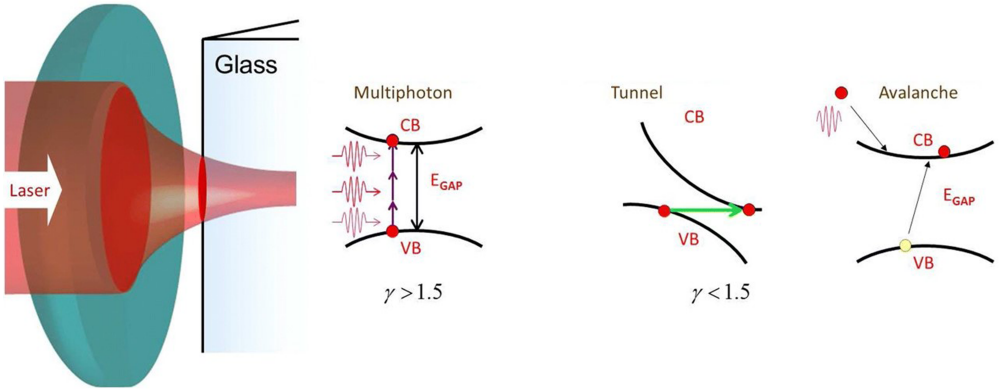

FIGURE 2.5: The three nonlinear photoionisation processes that can take place during ULI waveguide formation are multiphoton (left), tunnelling (centre), and avalanche ionisation (centre). E_{GAP} is the energy band gap of the substrate material. VB and VC are the valence band and conduction band, respectively. Image source: [98]

Multiphoton ionisation dominates at lower laser intensities and higher frequencies of the laser's electric field. In this scenario, the substrate material is transparent at the wavelength of the inscription laser (typically in near-infrared), preventing a single photon with frequency f from possessing adequate energy to elevate a valence electron from the valence band (VB) to the conduction band (CB). The simultaneous absorption of n number of photons becomes possible at high peak intensities, supplying sufficient energy for an electron to be promoted from the valence to the conduction band when $nhf > E_{bandgap}$, where $E_{bandgap}$ denotes the bandgap energy of the material.

The electrical field of the laser can distort the potential barrier at elevated laser intensities and lower frequencies. This distortion facilitates direct band-to-band transitions through quantum tunnelling, referred to as tunnelling photoionisation. The Keldysh parameter γ indicates the transition between multiphoton and tunnelling ionisation, as $\gamma = \frac{f}{e} \cdot \sqrt{\frac{m_e c n \varepsilon_0 E_{bandgap}}{I}}$ [99]. Where m_e stands for the electron-mass, n is the refractive index of the material, ε_0 represents the free-space permittivity, and I is

the laser intensity at the focus spot. In the case of $\gamma >> 1.5$, multiphoton ionisation dominates, and for $\gamma << 1.5$, tunnelling ionisation dominates.

Following the transfer of electrons to the conduction band through the mechanisms mentioned above, these electrons can absorb additional light through free carrier absorption. Suppose an electron absorbs a significant number of photons, then its energy may surpass the conduction band minimum plus the bandgap and can ionise another electron from the valence band upon impact. This leads to the presence of two electrons in the conduction band. This cyclic process, where the ionisation of one electron triggers the ionisation of another, can perpetuate and amplify. It is referred to as avalanche ionisation.

If the density of electrons in the conduction band reaches a critical value, usually $10^{21}/\text{cm}^3$ at 1 μm laser wavelength, the plasma formed by the electrons becomes highly absorptive, leading to optical breakdown. Glass materials typically require intensities of $I \approx 10^{13}$ W/cm^2. The electrons then pass their energy via electron-phonon interaction to the lattice, which happens on picosecond timescales, much longer than the duration of the femtosecond laser pulse itself. Consequently, a highly localised structural modification is formed due to energy deposition.

The structure alteration and refractive index change resulting from lattice heating strongly depend on the material. It can be empirically categorised into three distinct regimes: a gradual alteration of the refractive index, a modification characterised by birefringence due to the formation of self-aligned nanostructures, and the formation of empty voids within the material as a result of micro-explosions. Typically, these three phases manifest sequentially with increasing laser power [100]. However, it is important to note that the specific type of modification is generally determined by a combination of factors, including the laser and inscription parameters, as well as the inherent properties of the substrate material.

The gradual refractive index alteration can occur through rarefaction/densification induced by melting, changes in the bond structure and/or the generation of colour centres, as experimentally outlined in [101; 102; 103]. A colour centre is a defect that absorbs visible light due to an anionic vacancy that is filled by one or more electrons.

These laser-induced material modifications result in a change in refractive index, which may exhibit either a positive or a negative sign. Such a regime is observed when the laser power slightly exceeds the threshold for optical breakdown, approximately at 10^{13} W/cm^2. This particular parameter range is favoured for the inscription of low-loss optical waveguides.

A non-isotropic birefringent refractive index emerges at higher intensities, characterised by the self-alignment of nano-gratings perpendicular to the electrical field of the laser [104]. This phenomenon may be attributed to the interference between the laser field and the electron plasma wave [105]. However, the presence of nano-gratings as a potential source for uncontrolled birefringence and scattering losses renders this regime of limited suitability for the inscription of low-loss waveguides as required for astronomical beam combiners. Further intensification beyond 10^{14} W/cm^2 creates a shockwave emanating from the focal point, generating nano- and micro-voids. Although this regime has found applications for data storage, it is deemed inappropriate for inscribing optical waveguides [106].

A crucial distinction for the ULI waveguide formation lies in the thermal characteristics of the inscription process. Generally, one can distinguish between two regimes, *thermal* and *athermal*. The femtosecond pulse duration is well below the time required for heat diffusion, which for glass typically is on the order of micro-seconds. Yet, the repetition rate of the laser determines whether subsequent pulses fall within the thermal relaxation time [107]. In the athermal regime, characterized by low repetition rates around a few kilohertz and high-energy pulses of approximately 1 μJ, the pulse-by-pulse modification results in a modified region reflecting the intensity distribution of the laser beam. However, in order to maintain a seamless overlap between consecutive pulses reduces the writing speed to micrometres per second.

In contrast, the thermal regime, featuring repetition rates ranging from hundreds of kHz up to a few MHz, induces melting due to insufficient time for heat diffusion. This leads to circular cross-sections larger than the dimensions of the laser focal spot [100]. The isotropic nature of heat diffusion in this regime results in circular cross-sections. Despite the faster writing facilitated by the higher repetition rate, the athermal regime

is often preferred due to its ability to produce circular symmetric low-loss waveguides [108]. However, the choice of regime depends on the material.

In-depth reviews of the ULI writing processes are discussed by L. Li *et al.* [109], and S. Gross & M. J. Withford [97]. The physics behind ULI can be found in the book by R. Osellame, G. Cerullo, and R. Ramponi [110].

2.2.2 Mid-infrared optical material for ULI

ULI has been extensively explored for fabricating on-chip optical waveguides in various glasses materials with different wavelength-dependent transmission properties [111; 28]. The selection of suitable glass materials becomes limited when considering the mid-infrared regime, spanning from 3 to 20 μm. For instance, Figure 2.6 illustrates the transmittance of a range of common optical glass materials for mid-infrared wavelength. These selected materials become more restricted for the L' astronomical band, ranging from 3.5 to 4.0 μm, as required for ASGARD/NOTT - where low loss, high transparency, and availability in sufficiently large-sized substrates are key requirements [20].

Low loss is particularly critical in astronomy due to the intrinsic low brightness of distant astronomical sources. Propagation losses for ULI fabricated mid-infrared single-mode waveguides typically range from 0.1 dB/cm to 3 dB/cm, which is equivalent to 98% to 50% throughput per cm within the wavelength sub-band of 3–5 μm, representing an order of magnitude increase compared to near-infrared silica-based waveguides of $\sim$ 0.01 to 0.05 dB/cm, or up to 99% throughput per cm [112; 113].

Mid-infrared transparent materials other than GLS glass, such as Lead-germanates [115], Gallo-germanates [116], Tellurites [117] and Chalcogenides [118], have been employed as substrates for laser-inscribed mid-infrared waveguides. Among these, Gallium Lanthanum Sulphide (GLS) glass from the Chalcogenide glasses family has emerged as one of the most promising candidates for demonstrating low-loss waveguiding at extended wavelengths (> 3 μm) [119]. Furthermore, it is available in a sufficiently large size of 10 cm^2. Chalcogenide glasses possess high refractive indices, approximately $\sim$

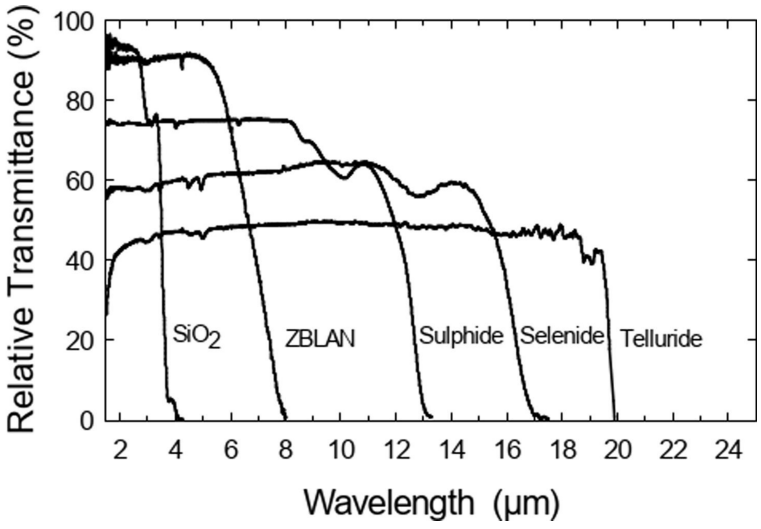

FIGURE 2.6: Transmission spectra of typical optical materials/glasses across the mid-infrared region. Silica (SiO_2), Fluorides (ZBLAN), Sulphide, Selenide, and Telluride bulk glasses are compared regarding relative transmittance and bandwidth. Image source: [114]

2.5, resulting in approximately 15% Fresnel reflection losses per facet. Mitigating these losses necessitates the application of broadband anti-reflection coatings on the small-sized input/output facets. Alternatively, materials with refractive indices ~ 1.5, and thus lower Fresnel losses of only 4%, have also been explored, such as ZBLAN (ZrF_4-BaF_2-LaF_3-AlF_3-NaF) glass from fluoride glass family, although its transparency is limited to $\sim 4\mu$m [120].

For the ASGARD/NOTT beam combiner, GLS glass was chosen due to its low loss, high transparency within the range 3.5 to 4.0 μm, and availability in sufficiently large-size. Moreover, GLS was discovered by Loireau-Lozach *et al.*, [121] in 1976. GLS glass exhibits a light orange colouration attributed to its band-gap of 2.6 eV ($\lambda =$ 475nm). This non-toxic glass contains high thermal resistance due to its glass transition temperature exceeding 500°C, which is much higher compared to other Chalcogenide glasses containing toxic Arsenic components.

3

Methods

This chapter describes the experimental methods and equipment employed. This includes the fabrication of photonic devices within GLS glass, both pre- and post-processing procedures, ultrafast laser inscription facilities, and optical microscope inspection of the fabricated GLS sample. To characterise the fabricated photonic components, two different test benches were utilised. The first investigation involved the examination of the mode-field diameters (MFDs) using a 3.39 μm HeNe laser conducted at Macquarie University. At the University of Cologne, using the second test bench, transmission measurements and the chromatic behaviour of the components in the range of 3.5 – 4.0 μm (astronomical L' band) were conducted using the fast Fourier transform technique. This test bench supports two configurations. The first configuration is based on a single Michelson interferometer capable of producing two beams with identical intensities. In comparison, the second configuration utilised a test bench

of two cascaded Michelson interferometers to generate four beams with near identical intensities. Both configurations were employed to conduct broadband interferometry experiments, specifically investigating null depth and contrast of the fabricated beam combiners.

3.1 Fabrication

3.1.1 Sample preparation

GLS glass samples with physical dimensions of either 50 × 10 × 1 mm or 50 × 15 × 2 mm, and their top and bottom surfaces polished were kindly provided by Prof Dan Hewak from the University of Southampton. The glass synthesis was supported by the Engineering and Physical Sciences Research Council (UK) through the project Manufacturing and Application of Next Generation Chalcogenides (EP/M015130/1). Depending on the specific requirements, the entire sample was either utilised for waveguide inscription or cut into smaller pieces of desired lengths using an SYJ-400 CNC dicing machine from the MTI Corporation. The dicing machine uses a water-cooled diamond blade. To prevent chipping or cracking of the delicate GLS glass, a slow feeding rate was selected during the cutting process and additional sacrificial soda-lime glass pieces were temporarily bonded to the top and bottom surface of the GLS glass. Following the cutting process, the prepared samples were placed in a falcon tube containing acetone and subjected to ultrasonic cleaning to release the protective glass pieces from the GLS samples.

After the ULI waveguide fabrication, the sample has to be taken through a grinding and polishing process. Before commencing these processes, two microscope slides are affixed to the top and bottom surfaces of the sample using UV adhesive (NBA107, Norland Products). Once the sample is bonded, it is attached to a fixture that fits the PP5 polishing jigs (Logitech, Scotland). Angular alignment provided by the PP5 jig ensured that the end face of the GLS sample is perpendicular to the waveguides. The angular alignment employs a 3.6 m long beam path for utilising the back reflection of a

visible HeNe laser (633 nm). This setup provides an approximate angular resolution of 1 arcmin. The subsequent steps involve coarse grinding with 25 μm grit Al_2O_3 abrasive for rapid material removal and fine grinding with 5 μm grit abrasive to achieve surface smoothness. Each abrasive is mixed with reverse osmosis filtered water to form a dispensable solution, which is constantly supplied onto a rotating cast iron plate with a diameter of 30 *cm*.

The PP5 jig is equipped with a digital micrometer gauge that facilitates the measurement of material removal. This gauge precisely measures how much material has been removed. After completion of the grinding stage, the cast iron plate is removed and replaced by a stainless steel plate with a polyurethane foam pad for the polishing phase. The abrasive is replaced with a colloidal silica slurry (Ultra-Sol 500S) with an average particle size of 70 nm, diluted with a solution of NaOH. The end-facets then go through 60 minutes of polishing on each side to obtain surfaces of optical quality.

3.1.2 The ultrafast laser inscription facility

The setup for ultrafast laser inscription involves a commercial mode-locked titanium-doped sapphire (Ti:sapphire) femtosecond oscillator (Femtosource XL500, Femtolasers GmbH) capable of emitting pulses at a central wavelength of 800 nm with a pulse duration of < 50 fs and a repetition rate of 5.1 MHz. This oscillator is installed on an optical table with air suspension and is located in a temperature-controlled basement laboratory at Macquarie University. The setup is designed to allow the laser pulses to travel through a series of alignment optics and characterisation devices before being focused by a microscope objective into the glass sample positioned on a three-axis translation stage, including an HD colour CMOS camera for live monitoring of the fabrication process as depicted in Figure 3.1. A comprehensive description of the function of each component can be found in [122] and [123].

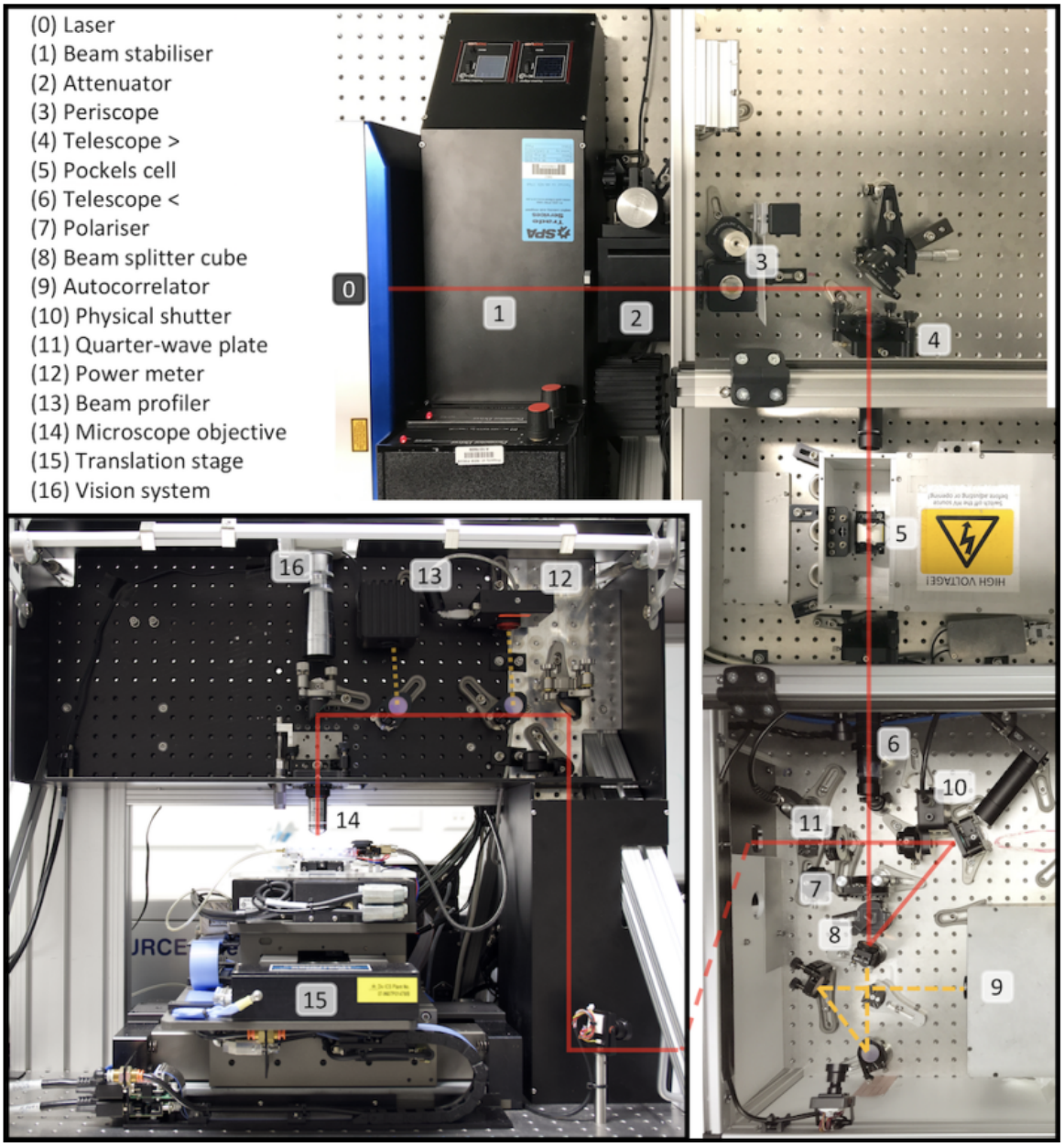

FIGURE 3.1: Photos of the ultrafast laser inscription setup for direct writing of optical waveguides. The red line indicates that the beam path passes through a series of optical alignment and characterisation elements, listed as 1-13, before being focused by the microscope objective, as 14, into the GLS glass sample placed on the translation stage, 15. A vision system, 16, used the inscription microscope objective for live monitoring of the fabrication process. Image credit [123].

The microscope objective used for waveguide inscription in GLS is an achromatic Olympus Plan N 100 ×/1.25 Oil PLN100XO. Designed for oil immersion, it possesses a short working distance of 150 μm and a numerical aperture (NA) of 1.25. The higher NA value ensures a more circular symmetric waveguide cross-section compared to objectives with relatively lower NA values. The inscription depth can extend up to 241 μm before the objective touches the GLS top surface according to $f_{depth} = z.n_{gls}/n_{oil}$, where f_{depth} represents the focal depth inside the material, z denotes the working distance between the objective and the sample, and n_{gls} and n_{oil} correspond to the refractive indices of the GLS glass and immersion oil, respectively. At the laser wavelength of 800 nm, the refractive index of GLS glass is $n_{gls} = 2.3931$, while the immersion oil possesses a refractive index $n_{oil} = 1.50$.

To write waveguides within the GLS substrate, a set of linear stages (Aerotech) provide sample translation in the XYZ-directions to facilitate the fabrication of three-dimensional optical devices by moving the sample through the stationary laser focus. The stage velocities are limited to 3000 mm/min for the X and Y directions and 240 mm/min for the Z-axis, with encoder resolutions of 62.5 pm and 32.6 pm, respectively. A tip/tilt mount is installed on top of the Z-stage, featuring a vacuum chuck to secure the sample in place and level it with respect to the stage XY-plane. The motion of the stages is controlled by a computer using a numerical control programming language (G-code).

3.1.3 Visual inspection

Following the waveguide fabrication, the initial step involves a visual examination of the waveguides to ensure the presence of a continuous and smooth modified region along the laser writing direction. The optical characterisation is conducted using an Olympus IX81 transmission microscope equipped with an Olympus DP74 camera. This microscope operates on the differential interference contrast (DIC) principle, initially developed by Georges Nomarski in 1955 [124]. The DIC technique enhances the contrast of transparent specimens by converting optical path differences into intensity differences. Through this visual inspection, any irregular modifications caused by laser

instabilities, surface defects, inconsistencies in the oil layer, as well as the potential presence of defects within the bulk of the substrate along the path of the written waveguides can be identified as described in Chapter 4. This process is crucial for isolating and identifying faulty waveguides before starting advanced characterisation.

3.2 Characterisation

The characterisation of the fabricated waveguide devices adheres to the prescribed criteria set by the ASGARD/NOTT. This comprehensive assessment encompasses several key parameters, including the mode-field profile in the mid-infrared range, optical throughput, spectral splitting properties, and broadband interferometric contrast and null-depth. Two distinct experimental setups, described as Setups I and II, have been employed to measure these properties. The setups facilitate the thorough examination and evaluation against the requirement for ASGARD/NOTT.

3.2.1 Setup I: mode-field profile

The mode-field profile of a single-mode waveguide depends on its physical size and shape, the refractive index contrast and the spatial distribution of the refractive index contrast. The characteristics are directly affected by the inscription parameters and the quality of the inscription process. The investigation of the mode-field profiles was conducted using a test bed at Macquarie University. This test bed incorporates a 3.39 μm Helium-Neon laser (REO-4018) as the mid-infrared source, possessing a narrow bandwidth and milliwatt level output power that renders it ideal for interrogating mid-infrared waveguides.

The HeNe laser is launched into an Indium Fluoride single-mode fiber (Thorlabs - InF3, 3.2-5.5 μm, 9 μm core, 0.26 NA). The opposite end of the fibre is collimated using a 50 mm off-axis parabola (OAP) mounted in a Thorlabs 30 mm cage setup as depicted in Figure 3.2. The alignment of the OAP against the fiber is adjusted using a Shearing interferometer and regular red HeNe laser source (633 nm). The OAP offers the advantage of achromatic collimation of any broadband or narrow band

point source such as the tip of an optical fiber. The absence of any chromaticty by the OAP combined with the flexibility of connector-terminated optical fibers, enables convenient swapping between mid-infrared, near-infrared radiation, and visible laser sources to facilitate ease of alignment.

After collimation the beam is directed towards a 50 mm Si-Ge achromat lens (Thorlabs) for launching light into the fabricated waveguides inside the GLS chip. The waveguidse samples are positioned atop a 5-axis stage equipped with a vacuum chuck to optimise injection.

The output signals are detected using two Zinc Selenide (ZnSe) objective lenses with focal lengths of f = 6 mm and f = 18 mm, respectively. The lens forms an image on a mid-infrared sensitive indium-antimonide (InSb) camera (FLIR SC7000, 1 - 5 μm). This detector records magnified mode profiles as images. The magnifications for the lenses with focal lengths of 6 mm and 18 mm are calibrated to $\sim$ 38 and $\sim$ 12.5, respectively. This calibration is achieved using a 1 $\times$ 2 Y-junctions, where the distance between the two output facets of the Y-junction is known (Chapter 5), along with the pixel size of 15 μm for the corresponding camera.

The recorded frames enable the calculation of the mode-field diameter in the vertical and horizontal directions based on either a Gaussian fit or the 4-σ method.

Gaussian fitting involves fitting a Gaussian function to the measured intensity distribution's vertical and horizontal line intensity profile. This method provides a distribution of the beam profile and allows for calculating the beam waist, corresponding to the MFD. Gaussian fitting is performed separately for the horizontal (X) and vertical (Y) directions using the mathematical relation $I(r) = I_{max}e^{-\frac{(r-r_0)^2}{2\omega_0^2}}$. In this relation, $I(r)$ is the intensity of point r from the position r_0 where I_{max} is the maximum intensity in the image, and ω_0 is the standard deviation within the distance $(r - r_0)$. Now, if at a distance D_r, $(r - r_0)^2/2\omega_0^2 = 1$, then the beam will be $I(r) = I_{max}e^{-2}$ and for this condition, the mode-field diameter will be in the direction r, $MDF_r = 2(r - r_0)$.

The 4-σ method is an ISO standard method where the mode-field diameter is 4 times the standard deviation of the image's intensity distribution along the axis X or Y. It is calculated from the second intensity moment of the beam profile. The measured MFD

for Gaussian fitting and 4-σ method are identical for a perfect Gaussian beam profile with no noise in the measurement system. With the presence of noise, aberrations or background, the 4-σ diameter is larger than the Gaussian fit [125]. A Matlab script, which S. Gross wrote, was used during the measurement.

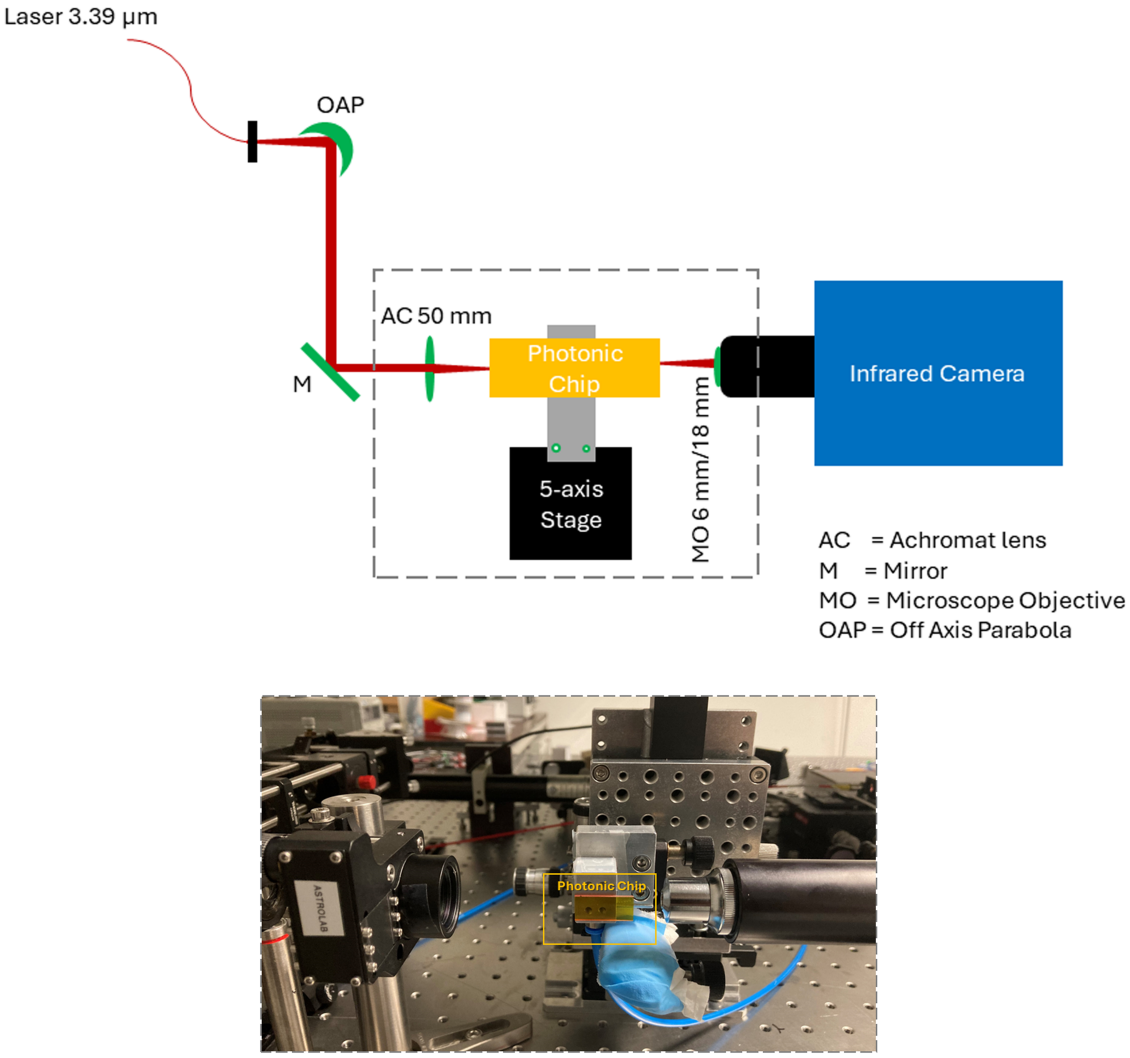

FIGURE 3.2: Schematic layout of the mode-field profile measurement test bed. Monochromatic light (3.39 μm wavelength) is coupled into the GLS waveguides. The output is imaged onto a mid-infrared camera for determining the mode-field diameters.

3.2.2 Setup II: interferometric characterisation

A dedicated interferometric test bench is essential for assessing the performance of beam combiners. Consequently, an interferometric test bench setup has been developed at the Infrared Integrated Optics for Interferometry Laboratory at the University of Cologne, as depicted in Figure 3.3 [35; 126].

The setup utilises either a commercial Leukos supercontinuum laser source (SCS) (200-5000 nm, P<2W) or a Thorlabs thermal blackbody source (BBS) (SL202L/M) as input. The source is coupled into the setup via a single-mode fibre (Thorlabs, InF3, 2-5.5 μm, 9 μm core, 0.26 NA). The beam is then collimated using a 50 mm achromat lens. An L' band bandpass filter (3.5-4.0 μm) is employed to filter the collimated beam. The corresponding experimentally-measured filtered spectra are presented in Figure 3.4. It is observed that both sources generate signals centred at the central wavelength of 3.75 μm of L' bandpass, but exhibit reduced flux towards the shorter wavelength limit of the L' band due to the filter characteristic. It is noted that the supercontinuum source (SCS) generates more flux and exhibits a centralised peak at 3.75 μm, spanning a spectral range from 3.65 to 3.85 μm. Consequently, this source is predominantly used throughout the experiments.

The L' signal is directed to a double-Michelson interferometer through a beam splitter, BS1. The first Michelson interferometer (MI 1) comprises mirrors M1 and M2 with BS2, while the second Michelson interferometer (MI 2) consists of mirrors M3 and M4 and another beam splitter, BS3. Among the mirrors of the double-Michelson section, M1 is fixed on the bench, while M2, M3, and M4 are placed on three motorised stages with Thorlabs Z812B actuator. These stages allow to introduce relative optical path differences between the four independent beams to facilitate interferometry. For simplicity, the four beams corresponding to mirrors M1, M2, M3, and M4 will be denoted as T1, T2, T3, and T4, respectively. T1 serves as the static reference beam, while the remaining beams can be tuned using adjustment knobs of the mirrors. Using beam splitter BS4, all four beams from the double-Michelson setup are launched via a $f_1 = 50$ mm achromatic lens into the waveguides or devices within the photonic chip. The waveguide sample is positioned on top of a 5-axis stage with an adapter capable

of precise angular tuning.

Diameters of the 4-beams are calculated as Point Spread Function (PSF) without installing the photonic chip. For that, an achromat $f_2 = 50$ is placed so that each beam passes through f_1+x+f_2 combination, where x = 5.5 mm. It allows forming an image with distance, di = f_2 + x. Hereafter, the object distance is calculated using $d_o = (f_2(d_i+x))/(d_i-f_2)$. Then, magnification is calculated as M $\sim$ 9.99 using the relation M = d_o/d_i.

Afterwards, the Full Width at Half Maximum (FWHM) is determined individually for each beam. Using a Python script to fit the data to a Gaussian distribution, the PSF of the individual beams is calculated as follows: $T1_{PSF} \sim 10.99$ μm, $T2_{PSF} \sim 10.91$ μm, $T3_{PSF} \sim 9.85$ μm, and $T4_{PSF} \sim 10.03$ μm.

For interferometric testing, the $f_2 = 50$ mm achromat is employed to collimate the output signals from the photonic components. In combination with an f = 50 mm camera lens, an image of the output is formed on an IR-sensitive camera across the 2-5 μm range (InfraTec-IRBIS). The imaging system creates a 1:1 relay on the camera such that each waveguide comfortably fits within a single pixel (30×30 μm) of the camera's image sensor. The detector is operated at a frame rate between 25 Hz and 250 Hz. It is observed that the intensities of all beams are not exactly identical and vary while adjusting the Michelson mirrors for tuning. It is due to the fact that beam splitters are 55/45, not precisely 50/50. Moreover, BS2 is less transmissive, and the two Michelson arms produced from this beam splitter appear to flatten from Gaussian shape (on the top, right two beams of Figure 3.4), possibly because of ageing. Multiple neutral density filters are used to equalise the beam intensities to ensure equal flux is launched into the photonic components.

The beam splitters BS1-BS4 utilised in this setup are Thorlabs pellicle beam splitters with a transparency range between 3-5 μm, while BS0 is a calcium fluoride broadband plate beam splitter operating in the range of 2-8 μm. Besides the 11 mm aspheric lens, all lenses in the setup are achromats designed for operation within the 3-5 μm range, consistent with the pellicle beam splitters.

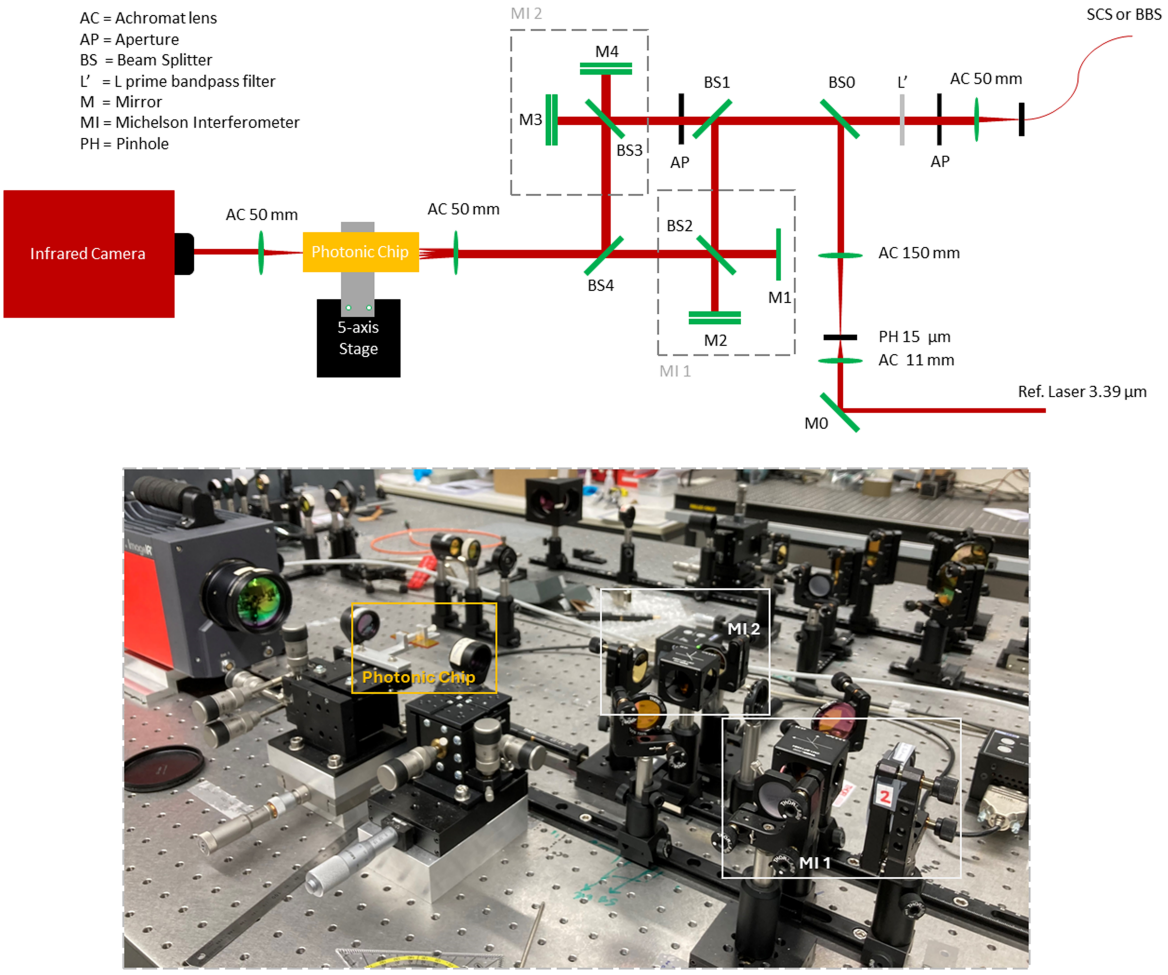

Figure 3.3: Schematic diagram of the experimental test bench and the corresponding lab setup shows that the mid-infrared source (SCS or BBS) feeds to the test bench using a mid-infrared fibre and passes through various optical elements to create two Michelson interferometers. The first Michelson (MI 1) is used to characterize one or two input photonic components. Four input photonic components are characterised using both Michelson interferometers (MI 1 & MI 2). A monochromatic metrology laser (Ref. Laser) is used alongside the broadband mid-infrared signal to calibrate the delay lines.

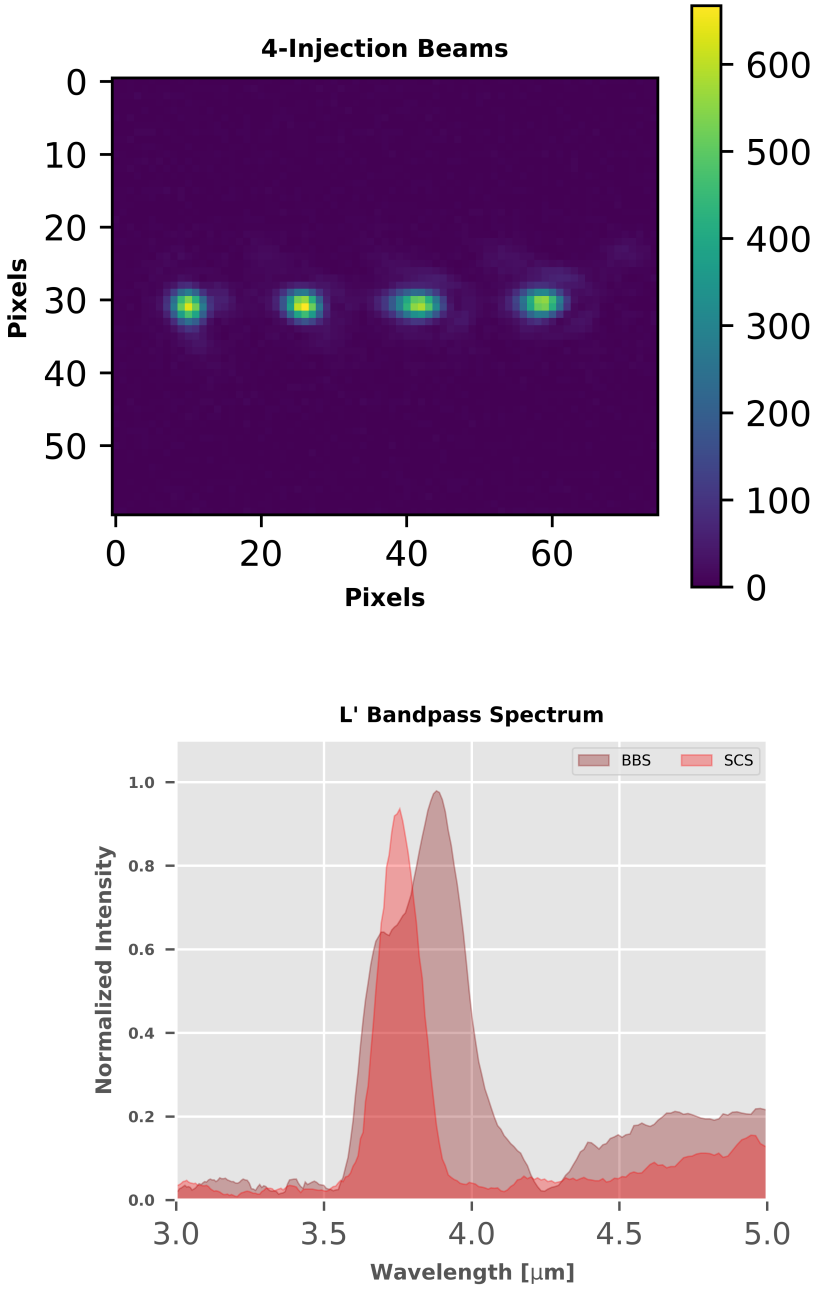

FIGURE 3.4: Top: Magnified image showing the four injection spots. Each pixel corresponds to 30 by 30 μm. From the right, two beams (T1 and T2) are produced using MI 1, and the next two beams (T3 and T4) originate from MI 2 of the interferometric test bench 3.2. Bottom: Normalised spectra transmitted through the L' band filter, either using the Black-Body Source (BBS) or the Super-Continuum Source (SCS) within the range 3.0 to 5.0 μm. It indicates that the effective transmitted region for L' is between 3.65-3.85 μm.

During the testing of four input nulling devices, all four beams (T1, T2, T3, and T4) are employed. However, for photonic devices containing only two inputs, only MI 1 is utilized by blocking the beam path of MI 2 using an aperture positioned before the entrance of MI 2 from BS1.

In addition to its 4-beam/2-beam broadband interferometry capabilities, the uniqueness of this setup lies in its ability to perform spectroscopic measurements using the Fast Fourier Transform Spectroscopy (FFTS) technique. FFTS offers an advantage over commercially available spectrometers, enabling the resolution and isolation of signals emanating from waveguides within the photonic component. The spectral resolution of FFTS can be adjusted by changing the scan-distance of the delay lines.

A Python script is utilised to characterise the spectral transmission or splitting ratios to extract spectral information from the time-domain interferogram and convert it into the frequency domain using a Fourier transform. The script is based on an algorithm first developed by J.W. Cooley and J.W. Tukey[127].

Initially, the script loads the interferometric signal and determines its length (using the number of data points, denoted as N). Using NumPy, a Discrete Fourier transform (DFT) is applied according to equation 3.1 [128]:

$$X[k] = \sum_{n=0}^{N-1} x[n] \cdot e^{-j \cdot 2\pi \cdot k \cdot n/N} \tag{3.1}$$

X represents the DFT outputs in the frequency domain, k is the index of the frequency component (range, [0, N-1]), n is the index of the time/sample in the range [0, N-1], when x represents the input interferogram sequence of length N.

Next, the frequency-axis for the Fourier transformed signal is calculated using another built-in NumPy function. The mathematical operation can be expressed as $f_k = \frac{k}{N \cdot \Delta t}$ where $(\Delta t) = \frac{1}{\text{sampling\_rate}}$ or the optical path delay between consecutive data points. This expression calculates the frequency values for each index k in the FFT output based on the number of data points N and the sampling rate. The frequencies are normalised with respect to the time interval between consecutive data points.

$X[k]$ contains complex numbers due to the Fourier transformation. From these

complex numbers, it is possible to calculate the modulus of the array of $X[k]$ and plot against their corresponding frequency-axis values. This plot is the spectrum of the interferogram in the frequency domain. However, in optics, wavelengths are more commonly used for measurements. Therefore, the frequency-axis is translated to the wavelength-axis using the relation $\lambda = c/f$ where c = speed of light and spectrum represents as a function of wavelength. By plotting the argument of the complex values $X[k]$ as a function of wavelength, one obtains the spectral *phase* of the interferogram. The phase contains information related to the phase shift induced by a photonic component, which provides information about how the component interacts with the electric field of the light [129].

The spectral resolution or resolving power of FFTS, denoted as R, can be calculated according to $R = \lambda/\Delta\lambda$, where $\Delta\lambda$ represents the coherence length of the interferogram or spectral bandwidth and λ is a particular wavelength of interest within the coherent length for measuring the resolving power. As a result, a highly coherent source needs more delay to resolve its spectrum accurately compared to a low coherence source.

For a Michelson interferometer, as shown in Figure 3.3, the resolving power depends on the optical path difference L between the interferometer's two arms. It can be written as $L = \lambda^2/(2\Delta\lambda_{\max})$ or $\Delta\lambda_{\max} = \lambda^2/(2L)$, when $2L$ is the total optical path of a Michelson interferometer (MI 1 or MI2) and $\Delta\lambda_{\max}$ is the maximum difference between the spectral bandwidth. Hence the resolving power can be defined as $R = \lambda/\Delta\lambda_{\max}$ or $R = 2L/\lambda$. Thus, it is possible to achieve higher spectral resolution by increasing the delay's travel range, L. Similarly, for a given travel range L, the spectral resolution increases with shorter wavelengths.

For FFTS, an instrumental challenge is the precision of the delay-line or motorised stages, which can drastically decrease the resolution by adding mechanical noise, which translates in spectral noise. To overcome this limitation of insufficient precision, a high coherence metrology or reference laser, a 3.39 μm HeNe laser, is simultaneously introduced into the system using the beam splitter BS0. The interferogram of the reference laser during the delay-line scan is simultaneously recorded with the SCS/BBS interferograms from the device under test. By utilising the knowledge of the fringe

frequency of the monochromatic 3.39 μm laser, the exact delay-line position can be determined with sufficient precision. The accurate knowledge of the delay's position is then applied to the polychromatic interferogram of the broadband SCS/BBS signal (L' band) during the computation of the FFTS[1].

[1]Most of the equipment of the test benches, optics and fabrication facilities were already available in the laboratories of Macquarie University and the University of Cologne, except for a few additional purchases for minor upgrades, such as filters, pellicle beam splitters, and collimation lenses. This enabled this project to focus from the start on the development of the beam combiner rather than experimental characterisation setups. Moreover, Macquarie University facilities were developed over the past 10+ years and used by multiple PhD candidates, and the successful PhD project by Jan Tepper was conducted previously under the facilities of the University of Cologne [130; 123].

4

Photonic building blocks

The integrated optics-based NOTT 4-telescope beam combiner or 4T-Nuller consists of multiple basic building block photonic elements. The design and optimisation of the nulling beam combiner start from studying the individual building blocks. Basic integrated optic components or photonic elements can be characterised by either being an active or passive element. Active elements rely on activators or additional power to activate their functionalities. Light sources, detectors, various types of optoelectronic modulators, and switches are typical examples of active photonic elements. On the contrary, passive elements operate without the need for an activator or additional input power. These elements manipulate light solely through their inherent optical properties, examples of which include straight waveguides, S-bends, Y-junctions, various types of couplers, multimode interferometers (MMI), tapers, and many more [131]. The NOTT beam combiner is a passive component, although thermal phase shifter

activators might be incorporated in a future revision for precise path length tuning.

Straight waveguides, curved waveguides or S-bends, Y-junctions, and directional couplers are the elements required for the design of the NOTT beam combiner. Using these building block elements, integrated photonic circuits for nulling interferometry will be presented for 2-telescope and 4-telescope configurations. The 2-telescope and 4-telescope beam combiners can be classified as a *single-Bracewell architecture* and *double-Bracewell architecture*, respectively. These architectures stem from the seminal 1978 publication by R. N. Bracewell [74].

This chapter presents the design and characterisation of the individual photonic elements that were fabricated using Ultrafast Laser Inscription (ULI). Valuable information related to the writing order, geometry, mode-field profile, bending radius, defects, and optical transmittance of each photonic element was investigated, which is crucial for compiling, optimising, and fabricating good-quality waveguides to develop the nulling beam combiner.

4.1 ULI optical waveguides in GLS glass

4.1.1 Waveguide formation

Ultrashort pulsed laser beams modify the refractive index of glass or crystal within the localised focus region during the ULI waveguides manufacturing process. Extensive research has explored different materials and their modifications for the ULI using femtosecond laser pulses, ranging from crystalline $Bi_4Ge_3O_12$ [132] and lithium niobate [133] to amorphous materials like fluoride [120] and chalcogenide glasses [134]. The waveguide geometries is determined from the modification of the glass or crystal as a response to the focused femtosecond laser pulses, often categorised into Type I and Type II [135]. These types were initially established for fiber Bragg gratings by J.L. Archambault *et al.,* [136]. While researchers have predominantly defined Type I and Type II in terms of positive and negative refractive index changes [137]. An article by S. Gross *et al.,* [138] discusses this classification in more detail.

In terms of waveguide geometry, it is important first to identify whether the refractive index change induced is positive or negative, where the shape is often correlated with the glass's refractive index and usually high refractive index glasses tend to form asymmetric shapes due to spherical aberrations [139]. However, mid-infrared optical waveguides must exhibit high refractive index contrast to minimise bending losses, have round mode fields for efficient coupling, and maintain low intrinsic losses to be compatible with the on-sky operation. Moreover, in terms of writing, waveguides with positive refractive index modifications usually exhibit shorter fabrication times using femtosecond laser pulses compared to negative refractive index-based waveguides because less material must be exposed to the femtosecond laser, as seen in Figure 2.4.

Arriola *et al.,* [119] have further expanded the classification of waveguide structures, particularly in glasses suitable for mid-infrared waveguide inscriptions for astrophotonics, and identified that GLS glass modification has positive and one of the highest refractive index profiles (n = 2.361) compare to other mid-infrared materials at 4 μm. In addition to the transmittance window (see Figure 2.6) and availability in larger sizes, a positive refractive index with high refractive index modification is another argument for considering GLS glass as the NOTT beam combiner material.

4.1.2 Waveguide inscription regime and techniques

In recent decades, the fabrication of optical waveguides in GLS glass using ULI has undergone extensive experimental investigation [140; 141; 118], particularly in the context of ULI fabrication with respect to the repetition rate of the laser [139]. These studies provide insight into the inscription of low-loss single-mode waveguides in GLS glass by contrasting different waveguide inscription regimes: (i) the thermal regime (high repetition rate) and (ii) the athermal regime (low repetition rate), which refer to whether the modification during inscription significantly exceeds the focal volume of the inscription laser. Suppose, at low repetition rates, each pulse induces a permanent material change within the focal volume, whereas, at high repetition rates, heat accumulation leads to material modification beyond the laser's focal volume [122].

Three techniques are commonly employed for waveguide inscription:

1. *Cumulative heating*, where waveguides are fabricated with a single scan at high repetition rates (thermal regime) utilising thermal diffusion to create sufficiently larger modifications [142].

2. *Slit beam shaping*, where a slit is placed in front of the focusing objective which shapes the laser beam to achieve the desired cross-section waveguide [143].

3. *Multiscan method*, where multiple scans are placed adjacent to each other until the desired cross-section is achieved [144; 145].

Over time, various researchers used different techniques with different combinations in GLS glass to produce low loss waveguides in mid-infrared, for instance, J.E. McCarthy *et al.,* [146], D. Lee [147], and R. Diener *et al.,* [148; 149] explored multiscan techniques in the athermal regime.

However, previous research conducted using Macquarie University's facilities by T. Gretzinger *et al.,* [150; 139] demonstrated that employing multiscan in an athermal regime could yield propagation losses as low as 1.5 ± 0.3 dB/cm at 3.39 μm. This was achieved with a laser repetition rate of 425 kHz, pulse energy of 100 nJ, and a 100 mm/min translation stage velocity. These results also exhibited a horizontal Polarisation Dependent Loss (PDL) of 0.24 ± 0.02 dB/cm. Mode-Field Diameter (MFD) was 23.5 × 25.1 μm.

Moreover, cumulative heating (single scan) in a thermal regime, propagation losses 0.47 ± 0.01 dB/cm measured at 3.39 μm, with a mode-field diameter of 22.9 × 24.7 μm, utilising a higher repetition rate of 5.1 MHz, pulse energy of ∼ 13 nJ, and a translation velocity of 100 mm/min. The width of the single-track waveguide was 7.5 μm.

The work extended to inscribing double and triple tracks with varied centre-to-centre spacings, resulting in decreased propagation losses of 0.33 ± 0.02 dB/cm with the double track of width 12.3 μm, and MFD ≈ 19.7 × 22.1 μm at 3.39 μm.

Additionally, a nearly linear decline in propagation loss was observed with increasing the wavelength for both single and triple structures, ultimately achieving propagation losses as low as 0.29 ± 0.06 dB/cm with the single track and with the triple track (physical size ≈ 19.4 × 19.8 μm) 0.22 ± 0.02 dB/cm at 4 μm, where MFD's are

23.7 × 27.2 μm and 22.3 × 22.6 μm, respectively. Also, various writing orders were experimented with- for triplets, including right-to-left, left-to-right-centre, and centre-to-right-to-left. Interestingly, each trial demonstrated identical propagation loss values and MFD.

These results highlighted the efficacy of a hybrid approach that combines cumulative heating (thermal regime) and the multiscan technique for fabricating good quality low-loss waveguides in the mid-infrared, particularly at the L' band. This hybrid methodology was found to be the optimal strategy for fabricating single-mode straight waveguides because this mechanism can produce less lossy waveguides in GLS glass samples.

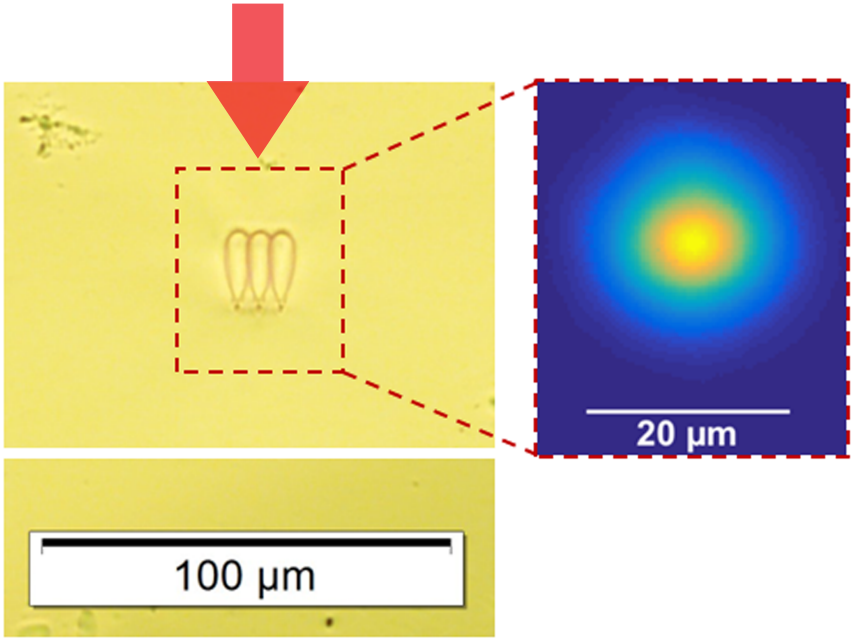

FIGURE 4.1: The enlarged picture showcases the cross-sectional view of an inverted teardrop-shaped triplet, along with its amplified illumination as MFD, under the influence of a 3.39 μm HeNe laser source. The red arrow indicates the direction of the inscription laser.

Figure 4.1 shows the tear-drop-shaped cross-section of a triplet and its MFD at 3.39 μm produced by the hybrid approach. Cumulative heating is responsible for the visually distinguishable inner region from its outer halo as a tear-drop shape, initially

demonstrated by various researchers [140; 141].

T. Gretzinger *et al.,* [151] demonstrated through the use of Raman spectroscopy and electron probe microanalysis (EPMA) in GLS glass that this phenomenon arises due to a positive refractive index change in the waveguide, with an overall value of $\Delta n_{waveguide} = 0.0049$, compared to its bulk refractive index $n = 2.38462$ (at 833 nm), during the femtosecond laser direct writing process in the GLS glass.

In the waveguide's shell region, an average index contrast of $\Delta n_{shell} = 0.0095$, with a peak index contrast of $\Delta n_{peak} = 0.023$, is found. Additionally, the waveguide core regions exhibit a refractive index gradient, with positive index values near the shell and a negative refractive index change towards the centre, with a maximum value of Δn_{core} = -0.0093. The average change in the index within the core regions is Δn_{peak} = -0.0003.

These overall localised modifications are created by nonlinear absorption and multiphoton processes such as electronic excitation, ionisation and localised changes of the material's composition, resulting in a change in its refractive index as discussed earlier in Chapter 2.

‘

4.2 On-chip optical waveguides

As a part of the ASGARD/NOTT project, four prototype photonic chips are manufactured, and they are chronologically identified as Sample I, Sample II, Sample III, Sample IV. These chips belong to two GLS glass batches, Sample I and Sample IV are from batch *LD 1765*, Sample II and Sample III are from batch *LD 1999*.

Figure 4.2 shows the four prototype photonic chips with a schematic diagram showing the arrangement of the photonic elements, such as waveguides, Y-junctions, directional couplers and the beam combiners themselves. Individual elements serve as test structures to verify the ULI process as well as for exploring different geometrical and inscription parameters for subsequent sample iterations. The overall requirements for the final NOTT beam combiner are listed in Table 4.1.

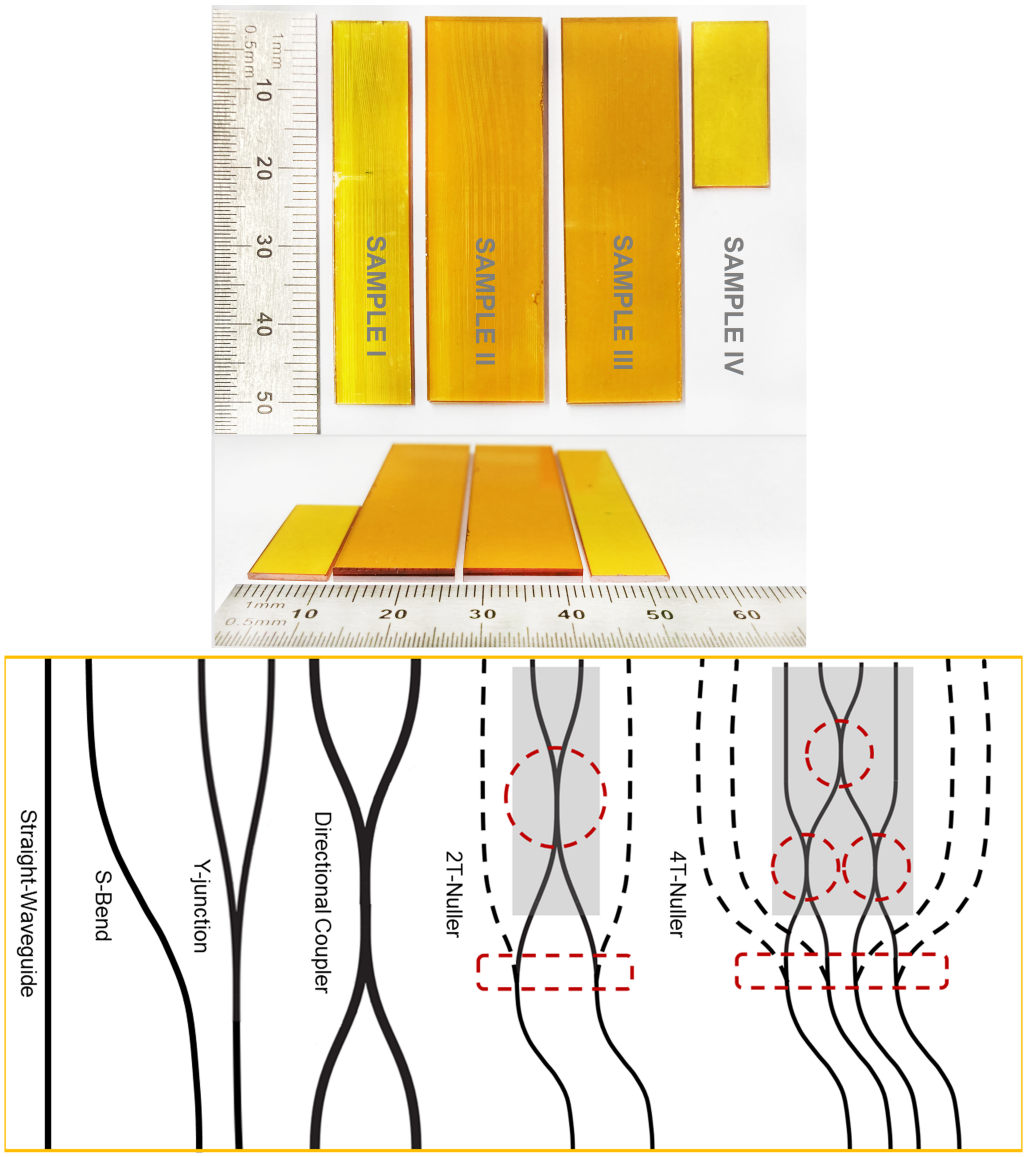

FIGURE 4.2: The top two images show the physical dimensions of four ultrafast laser inscribed photonic chips in GLS glass, SAMPLE I, SAMPLE II, SAMPLE III, SAMPLE IV. The schematic in the bottom image illustrates the spatial arrangement of fundamental building-blocks within the chips, such as straight waveguide, S-bend, and Y-junction. The basic elements are typically followed by a series of 2T-Nuller and 4T-Nuller. Red dash lines are displaying the locations of directional couplers and Y-junctions inside the Nullers.

4.2.1 Straight waveguides and their mode-field profile

As part of the current investigation related to the ASGARD/NOTT project, 15 triple-track straight waveguides, or triplets, were inscribed using the hybrid approach involving the multiscan technique in the thermal regime in the GLS glass of Sample IV. These waveguides were fabricated to explore their mode-field profiles and verify that this project's waveguides work with the optimal inscription parameters.

The fabrication process utilised a femtosecond laser repetition rate of 5.1 MHz, with a pulse energy of $\sim$ 13 nJ. The modification sizes or widths for single scans were 4.5, 5.5, and 6.5 μm, while for triplets, three scans were performed with offsets between two modifications of 0.00425, 0.00525, and 0.00625 μm, respectively. Five translation velocities (feedrate) were employed for these three types of modifications, including 100, 250, 500, 1000, and 2000 mm/min.

The writing order chosen for all these triplets was *left to right*, where the left track was written first, then the central and right tracks followed. This writing order is optimised based on the manufacture of 50/50 achromat directional couplers and will be discussed in Chapter 6.

Subsequently, using the *characterisation setup I* test bed of Figure 3.2 at Macquarie University, the mode-field diameters of these waveguides were measured using *Gaussian fitting* and the 4-σ method techniques for 3.39 μm, with a magnification of $\sim$ 12.5 using an 18 mm microscope objective lens detailed in Chapter 3. Both methods demonstrated similar trends. However, Figure 4.3 is included to illustrate the measurement results obtained from the Gaussian fitting method.

The results reveal that the average MFDs, obtained from the horizontal and vertical cross-section diameters of the triplets, fall within the range of 26 to 28 μm, indicating that variations in translation velocity or feedrate have minimal impact on average MFD sizes. This suggests that even with faster writing speeds, waveguides can be fabricated while maintaining consistent levels of MFDs.

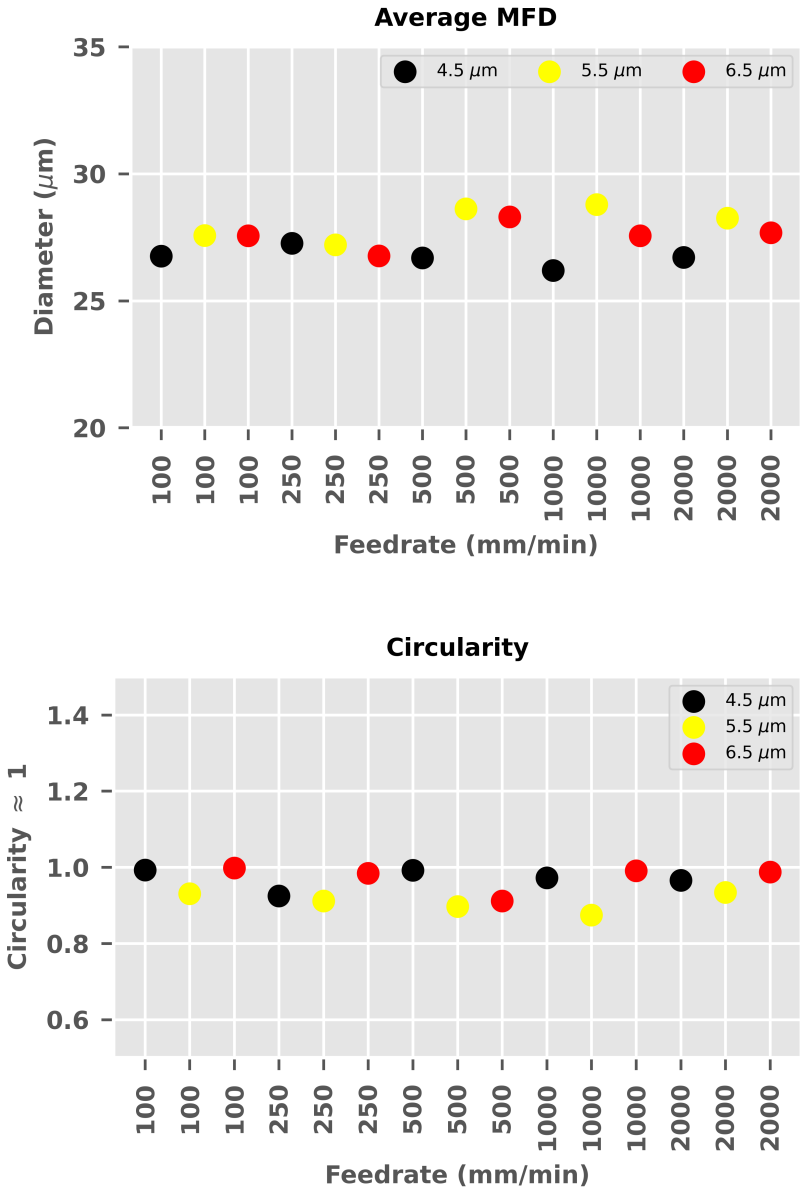

FIGURE 4.3: In the top plot, the average diameter, derived from horizontal and vertical cross-section diameters of the triplets, is plotted against the federate. The bottom plot illustrates the circularity of the mode-field profile, determined by the ratio between the minimum and maximum values of horizontal and vertical cross-section diameters for individual triplets. The trends observed in this ratio are closely comparable. For both plots, Black, yellow, and red colours represent the single-modification size.

Furthermore, achieving a perfect circular cross-section necessitates equality between horizontal and vertical MFDs. To assess circularity, each of the triplet's MFDs was compared where the minimum and maximum values between horizontal and vertical dimensions were obtained and calculated as the ratio ∼ *min(horizontal, vertical)/max(horizontal, vertical)*. A ratio of 1 indicates a perfectly circular mode-field profile. The results indicate a circularity trend consistent across different translation velocities and modification sizes with the circularity of the mode-field profiles ≈ 0.95 ± 0.03.

The insight from this measurement is that a similar level of circularity and mode-filed profile is achievable with explored writing speeds and modification sizes, which can significantly reduce manufacturing time with high translation velocity without affecting the size of mode-field diameter in mid-infrared.

4.2.2 S-bends

For NOTT photonic devices, S-bends are integral components of directional couplers and Y-junctions, playing a crucial role in the beam combiner by effectively redirecting stray light to minimise contamination of the sensitive interferometric outputs.

Photonic integrated circuits can use various different kinds of S-bends or S-curves, such as (a) the radial arc, characterized by the utilisation of inverted arcs featuring uniform curvature, as described in Equation (4.1), and (b) sinusoidal S-bends, encompassing either cosine or raised-sine S-bends. These sinusoidal S-bends follow Equations (4.2) and (4.3), respectively [152]. Where L is the longitudinal dimension or the length of the S-bend, W is the lateral offset or the width of the S-bend, as shown in Figure 4.4. For identical lengths and longitudinal offsets, the radii of curvature, $R(s)$, along the S-bends vary for the different types. The radius of curvature can be expressed as equation (4.4) [153].

$$y(x) = \begin{cases} \sqrt{M^2 - x^2} - (M - W) & \text{, when } 0 \leqslant x \leqslant \frac{L}{2} \\ -\sqrt{M^2 - (x - L)^2} + M & \text{, when } \frac{L}{2} \leqslant x \leqslant L \end{cases} \tag{4.1}$$

where $M = \frac{L^2}{4W} \cdot \left(1 + \frac{W^2}{L^2}\right)$.

$$y(x) = \frac{W}{2} \cdot \left(1 - \cos\left(\frac{\pi}{L} \cdot x\right)\right), \text{ when } 0 \leqslant x \leqslant L \tag{4.2}$$

$$y(x) = \frac{W}{L} \cdot x - \frac{W}{2\pi} \cdot \sin\left(\frac{2\pi}{L} \cdot x\right), \text{ when } 0 \leqslant x \leqslant L \tag{4.3}$$

$$R(s) = \frac{(1 + y'(x)^2)^{3/2}}{|y''(x)|} \tag{4.4}$$

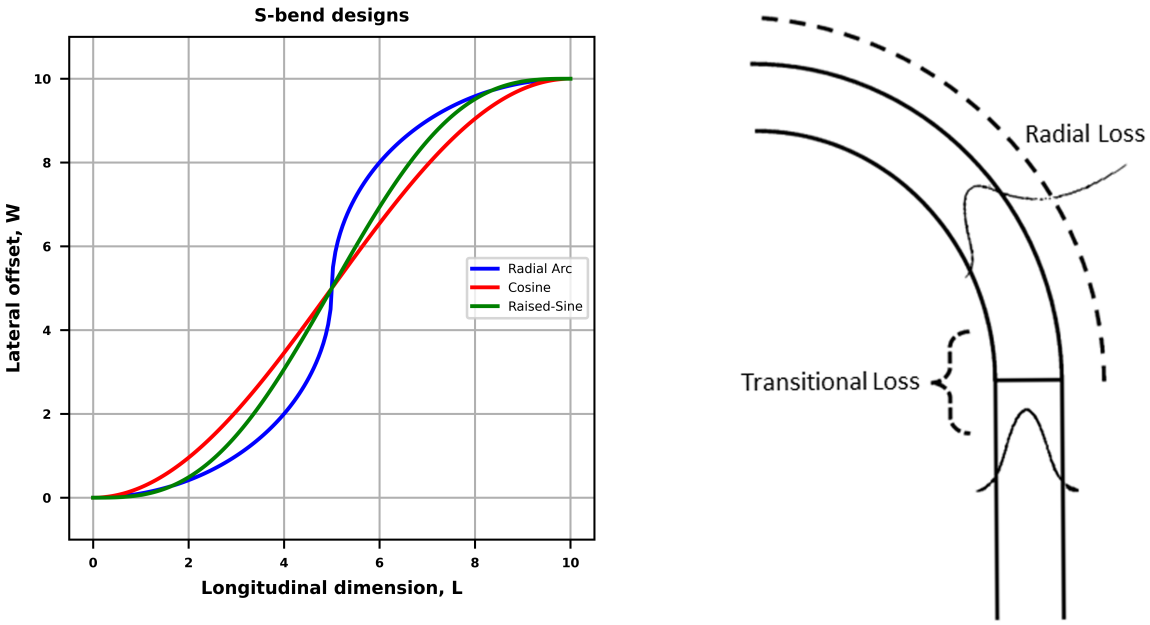

FIGURE 4.4: The left plot illustrates three different S-bends types—radial arc, cosine, and raised-sine bend, plotted with identical length or longitudinal dimension L and width or lateral offset W. The sketch to the right depicts the transitional and radial loss that occurs in S-bends.

In design, the radius of curvature influences the characteristics of the S-bend, particularly structural losses. Theoretical descriptions of such loss can be summarised from the article of K.L. Kruse, & C.T. Middlebrook [152], where the structural loss L_s can be identified from the summation of transitional loss Γ_T and radial loss Γ_R in dB, as described in Equation (4.5) and illustrated in Figure 4.4.

$$L_s(\text{dB}) = \sum \Gamma_R + \sum \Gamma_T \tag{4.5}$$

Continuous power radiation along the curve path causes radial loss. For the radial attenuation coefficient $\alpha(R, s)$, the radial loss can be represented as Equation (4.6).

$$\Gamma_R(\text{dB}) = e^{-\int_S^0 \alpha(R(s),s)\, ds} \tag{4.6}$$

Transitional loss arises when there is a mode-mismatch, i.e. a mismatch in the near-field electric-field profiles. Such a mismatch occurs at the transition between a straight and a bent waveguide or waveguide segments of opposite curvature, as occurs in the middle of an arc-based S-bend. This loss can be calculated using the mode overlap integral Equation (4.7), where E_{in} and E_{out} are the electric fields at the end of the first segment and the start of the second segment, respectively.

$$\Gamma_T(\text{dB}) = 1 - \frac{\left|\int E_{\text{in}}(x,y) E^*_{\text{out}}(x,y)\, dy\, dx\right|^2}{\int |E_{\text{in}}(x,y)|^2\, dx\, dy \cdot \int |E_{\text{out}}(x,y)|^2\, dy\, dx} \tag{4.7}$$

The primary factor often limiting the performance of well-designed S-bends is the transition loss, while the radial loss can be mitigated by adjusting the minimum bend radius through an increase in the S-bend length. However, this elongation may contribute to the *total losses of the S-bend* due to the intrinsic linear propagation losses of the waveguides. Additionally, the radii of curvature can vary among different S-bend configurations, even when they share the same total length.

Theoretical investigations have shown that cosine S-bends exhibit the least losses for a given length and longitudinal offset [154; 155]. Moreover, cosine S-bends start and end with maximum curvature, this limits coupling in the S-bends when using them for directional couplers. Therefore, the cosine S-bends have been used in all beam combiner designs.

Previous work has shown that straight waveguides and cosine S-bends are comparable in terms of loss at 4 μm wavelength for the *bend radii* > 40 mm, where the excess loss of cosine S-bends was measured using the Fabry-Perot method [150], as shown in Figure 4.5. It means structural losses become dominant when the bend radii are smaller than < 40 mm. Therefore, a minimum *bend radii* > 40 mm has been used for all photonic components. Other sources of loss that impact the throughput of the

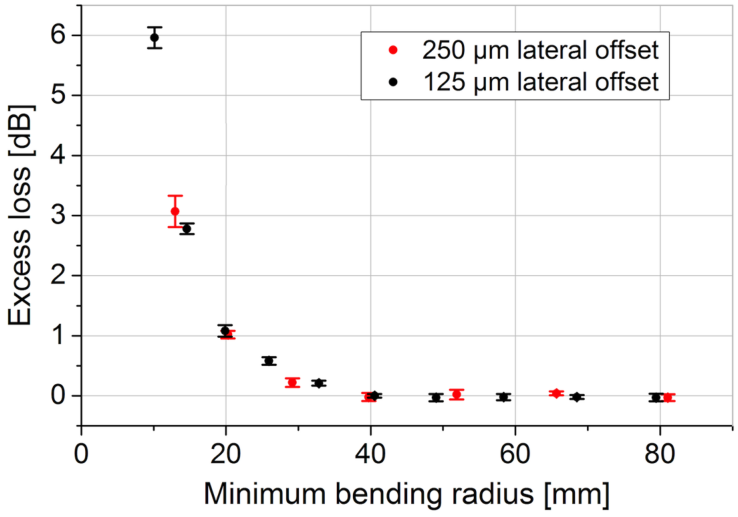

FIGURE 4.5: At the wavelength of 4 μm, cosine S-bends based on the triplet waveguides in GLS exhibit negligible losses for bending radii exceeding $>$ 40 mm. Image credit: [123].

fabricated devices are discussed in the last section of this chapter.

4.2.3 Y-junctions

Y-junctions serve the purpose of combining or splitting optical signals [131]. They are comprised of straight waveguides and S-bends to form a Y-shaped junction from a common stem to two branches.

Within the ASGARD/NOTT project, Y-junctions are used as achromatic 1×2 power-splitting elements. For the 4T-Nuller, the light from each input has to be split to direct approximately 80% of the telescope's signal to the interferometry section, while the second path is configured to allocate the remaining 20% of the signal for photometry, as outlined in Table 4.1.

Further elaboration on Y-junctions and the optimisation is undertaken to identify the appropriate designs for ULI in GLS glass and their characterisation is provided in Chapter 5.

4.2.4 Directional couplers

Directional couplers or 2 × 2 couplers are the key integrated optics elements for performing beam combinations. By design, they consist of two closely spaced straight waveguides with lead-in and lead-out S-bends. The close spacing facilitates the transfer of power between the two waveguides. The power transfer or splitting ratio depends on the distance between the two waveguides and the interaction length along with the wavelength of the propagating light.

In this project, the most crucial requirement of the directional couplers is to provide 50/50 achromatic splitting for performing interferometry in broadband by equally splitting and combining signals from the telescopes, as noted in Table 4.1. For this purpose, asymmetrical directional couplers are used to produce 50/50 achromatic splitting and beam combination across the L' band. Chapter 6 contains a detailed theoretical and experimental discussion on the laser-written directional couplers in GLS glass for the NOTT.

4.2.5 2T-Nullers

Building on the concept of the basic *single-Bracewell* Nuller [74] with the aided ability to simultaneously track photometry during its operation [156]. Side-step S-bends lead the telescope signal to the Y-junctions from the input region. These s-bends suppress uncoupled stray light at the input coupling region. The Y-junctions split each incoming signal into two branches from the S-bend sections, with one portion passing through the interferometry section based on an achromatic 50/50 directional coupler. This directional coupler performs interferometry by combining the two beams coming from two telescopes. The other branch, designated as the photometry channel/taps, enables the instrument to track the intensity of the incoming telescope signals and lets one perform photometric correction of the observed destructive interference.

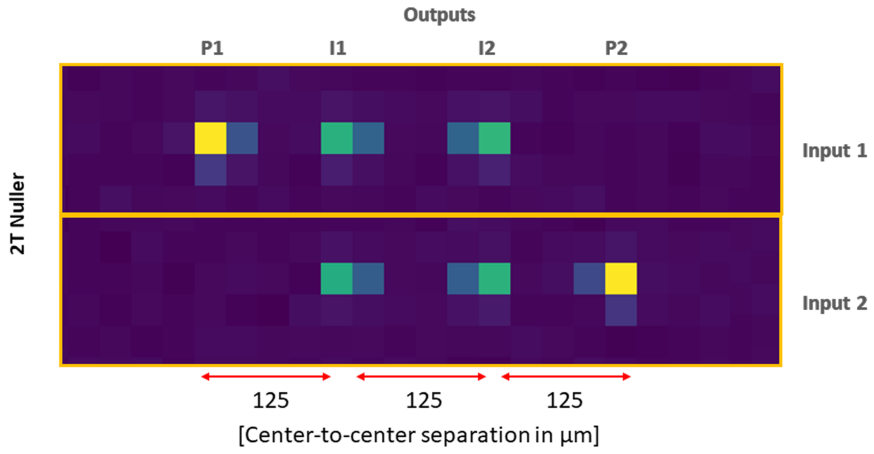

FIGURE 4.6: Output of a 2T-Nuller recorded with the mid-infrared camera of 30 × 30 μm/pixel for injection of two individual beams from the supercontinuum source. P1 and P2 are two photometric taps/outputs, and I1 and I2 are two interferometric outputs. All the outputs are in equidistant separation of 125 μm

Figure 4.6 shows example outputs of a 2T-Nuller of Figure 4.2, with two photometric taps (P1 and P2) and two interferometric outputs (I1 and I2). The light was launched sequentially into the two independent inputs. More details on the design, nulling performance and simultaneous photometric correction methods are presented in Chapter 7.

4.2.6 4T-Nullers

The *double-Bracewell* Nuller for NOTT harnesses the basic concept of the 2T-Nuller. The 4T-Nuller combines signals from four telescopes for nulling [35]. Similar to the 2T-Nuller, it includes photometry for the incoming starlight using Y-junctions after the stray-light suppressing S-bends. The key advantage lies in its implementation of a cascade of 50/50 achromatic directional couplers. The first two directional couplers create two nulled signals feeding the third directional coupler, as shown in Figure 4.2. This results in two nulled outputs. By subtracting these two outputs of the central combiner, a self-calibrated null can be acquired [157].

On-chip, input spacing between four input facets are equal (125 μm). However,

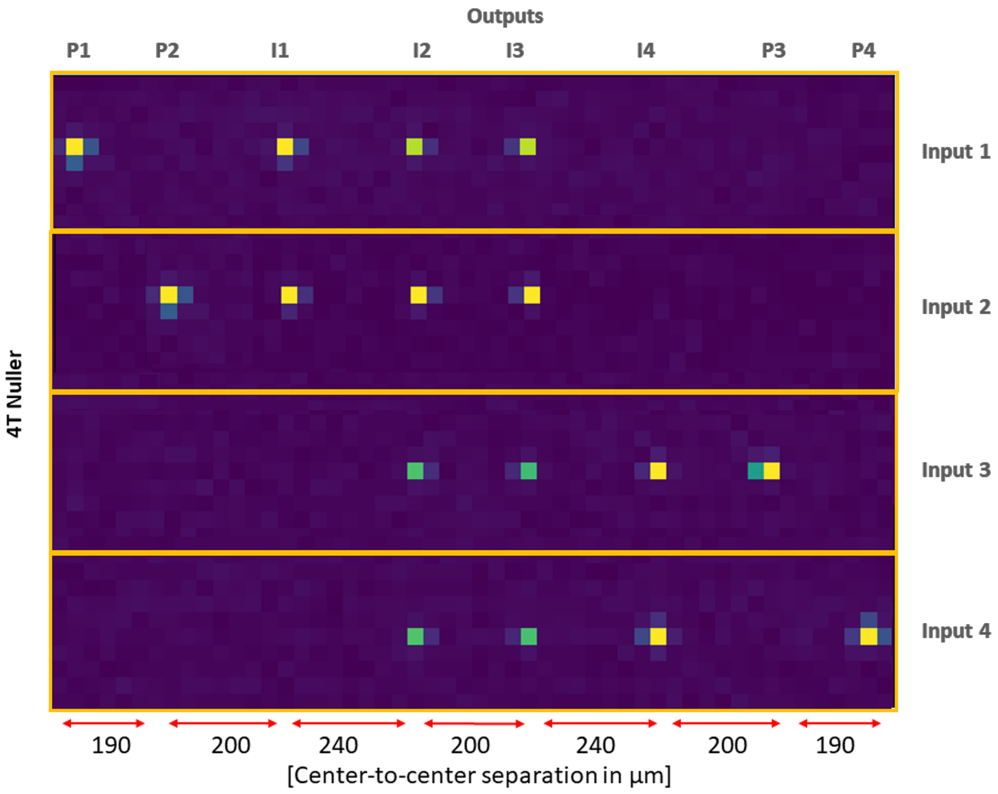

Figure 4.7: All outputs of a 4T-Nullers, 4 × photometry (P1, P2, P3, P4) and 4 × interferometry (I1, I2, I3, I4) after sequential injection into each of the four inputs. The spacing between the outputs are designed as 190 – 200 – 240 – 200 – 240 – 200 – 190 μm optimised for the NOTT's back-end optics [34; 65]

output spacing, as presented in Figure 4.7, is non-equidistant and followed the ZEMAX design developed for the NOTT's back-end optics [34; 65]. This optimised arrangement, with non-equidistant spacing, will allow to prevent overlap between the output signals. Additionally, the signals from nulled outputs will be sufficiently isolated to avoid any influence or cross-talk from anti-null or photometry signals on the ASGARD detector.

Chapter 8 presents the design and experimental characterisation showing the interferometric performance of the 4T-Nuller. A functional 4T-Nuller for the NOTT instrument is the main goal of this thesis.

4.3 ASGARD/NOTT photonic requirements

To achieve the ASGARD/NOTT science case (discussed in Chapter 1), specific requirements are placed on the GLS glass 4T-Nuller. These criteria are summarised in Table 4.1. Several iterations of photonic chips with complete beam combiners were fabricated with incremental improvements to accomplish these criteria. SAMPLE I, SAMPLE II, SAMPLE III, SAMPLE IV are the four iterations of photonic chips that have been fabricated, characterised and analysed as part of this thesis. Each chip accomplishes one or multiple requirements.

TABLE 4.1: Key photonic requirements for the ASGARD/NOTT [35; 33; 65; 34].

On-chip waveguides	Operational range	3.5-4.0 μm (GLS glass)
	Mode-field profile	Single-mode
Y-junctions	Splitting for photometric tap	20/80
	Chromaticity	Achromatic
Directional couplers	Splitting for beam combination	50/50
	Chromaticity	Achromatic
	Phase shift between two outputs	180 degree
4T-Nuller	Optical throughput	$\approx$ 50%*
	Contrast level (raw and self-cal.)	$10^{-2} - 10^{-5}$

* without Fresnel loss

The inscription parameters and device geometries for the first prototype photonic chip, SAMPLE I, were taken from the work of T. Greetzinger *et al.*,[150], comprised 10 $\times$ 4T-Nullers. During the characterisation process, weak functionality in 4T-Nullers was observed where one of the interferometric outputs suffered from suboptimal writing order. As a result, a second prototype photonic chip, SAMPLE II, was fabricated soon. This second iteration contained 7 $\times$ 4T-Nullers, two sets of reference directional couplers with different writing orders, and a series of building block waveguides.

Upon characterisation of SAMPLE II photonic chip, it was observed that the directional couplers of the nulling devices exhibited $\sim$ 70/30 imbalances, deviating from the NOTT's requirement of 50/50 splitting ratio [35]. Thereafter, a set of reference directional couplers with writing order *left to right* and extended parameter scan of interaction length led to identifying appropriate interaction lengths and writing order

to fabricate a 50/50 achromat directional coupler [35]. More details of the splitting ratios of the directional couplers are discussed in Chapter 6.

Building on the insights gained from characterising Sample II, Sample III was manufactured to consolidate the learning from Sample II and incorporate them into a new batch of nulling beam combiners, which eventually led to achieving the desired 50/50 achromat directional couplers. This chip also contains 2T- and 4T-Nullers 50/50 achromatic directional couplers. Therefore, nulling interferometry tests were carried out with this chip in the lab. Chapter 7 and 8 are devoted to nulling interferometry measurements with 2T-Nuller and 4T-Nuller, respectively.

Moreover, the Y-junctions used for photometry in 4T-Nullers of Sample III did not yet exhibit the desired 20/80 splitting ratio across the L' band to fulfil the NOTT instrumental requirements, as described in Table 4.1. To address this requirement, Sample IV was fabricated, where a series of Y-junctions with different geometries were explored. The optimisation of the geometry was informed by beam propagation simulations using the commercially available RSoft BeamPROP module. Characterisation showed good agreement with the simulation and resulted in Y-junctions with 20/80 splitting. These Y-junctions will be introduced into the next batch of 4T-Nullers, which is beyond the scope of this thesis. The Y-junction design, optimisation and characterisation are discussed in Chapter 5.

4.4 Optical throughput

High throughput or low-loss photonic components are a major requirement in astronomy, because of the intrinsic weakness of the observed distant astronomical sources.

Mathematically, throughput (T) can be obtained in percentage from the Equation (4.8), where P_{in} is the total power incident on a specific waveguide or a photonic device and P_{out} is total output power emerging from the output facets.

$$T = \frac{P_{out}}{P_{in}} \times 100\% \tag{4.8}$$

Moreover, the total output power can be estimated in dB using the relation, $P_{out} =$

(P_{in}–I_L), where I_L is the *insertion loss*, and it is the amount of power that a signal loses after the transmission through the waveguide. The insertion loss is the sum of three loss components: (i) coupling loss C_L, (ii) Fresnel loss F_L, and (iii) internal losses, such as linear propagation loss, bend losses and transition losses.

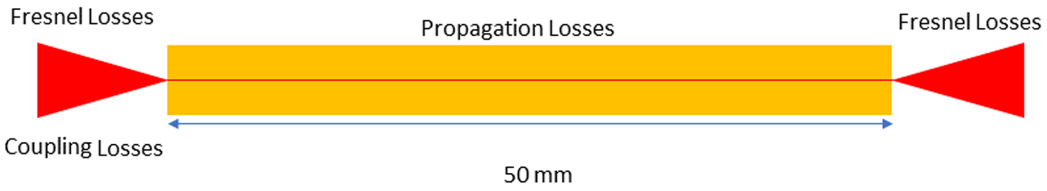

FIGURE 4.8: Sketch of a straight waveguide with the various sources of loss, such as coupling, Fresnel loss, and propagation losses indicated depending on their location of occurrence.

For a waveguide, coupling losses C_L occur at the input interface between the free-space and the waveguide facet, as shown in Figure 4.8. They result from the mismatch in electric-field profile between the waveguide mode and focal spot of the injection beam. The coupling losses increase if there is angular and/or spatial misalignment in addition to a field mismatch. Theoretically, the best coupling efficiency between the Airy pattern at the focus of a homogeneously illuminated lens and the Gaussian mode of a single-mode waveguide is 81% [158].

Fresnel losses F_L occur at the interface between two optical media with different refractive indices. These losses are attributed to partial reflection and partial transmission of light (also identified as Fresnel reflection) caused by an impedance mismatch at the interface. This loss can be calculated using the relation $F_L = \frac{(n_{gls}-n_0)^2}{(n_{gls}+n_0)^2}$. The Fresnel loss between air and GLS glass is $\approx$ 15.6% or - 0.74 dB per facet, where $n_0 = 1$ and $n_{gls} = 2.3159 \pm 0.002$ at a wavelength of 3.4 μm [159]. The GLS refractive index at mid-infrared wavelengths was interpolated from refractive index measurements conducted by VITRON GmbH commissioned by J. Tepper *et al.,* [159]. This loss can be mitigated with antireflection thin-film coatings, which would increase the overall throughput by $\approx$ 30%.

The *internal losses* of a device are the sum of propagation loss P_L, bending loss B_L, and transition losses T_L. The propagation loss encompasses the attenuation of light as it propagates along the waveguide. This loss is primarily attributed to material absorption, scattering, and other intrinsic factors. Propagation losses are usually measured in dB/cm according to $P_L = \frac{1}{L}10 \cdot log\frac{P_0}{P_{Left}}$ dB/cm [160], where P_0 is the initial power, L is the total length of the waveguide, and P_{Left} is the power left after propagation. However, propagation losses of mid-infrared compatible integrated optics platforms based on lithography across the wavelength band of 3–5 μm, such as SiN/Si, SOI, Ti:$LiNbO_3$, Si/Al_2O_3, and Ge/Si range between 98% to 50% throughput over 1 cm, equivalent to 0.1 to 3 dB/cm. This is an order of magnitude larger than at near-infrared wavelengths, such as silica-based waveguides, which feature up to 99% throughput per cm (0.01 to 0.05 dB/cm) [112; 113].

In the context of curved waveguides, such as S-bends, bending losses B_L can arise from the curvature of the waveguide path, causing light to leak out as radiation from the waveguide core due to mode distortion. The bending radius is maintained as $\geqslant$ 40 mm for the NOTT's S-bends to have negligible bend losses. This threshold has been optimised from prior research outlined in Figure 4.5.

Furthermore, transition loss T_L represents another significant factor contributing to internal losses beyond propagation and bending losses. Transition loss occurs when light incompletely escapes from the waveguide's cladding. A typical scenario where transition loss manifests is in Y-junctions, where light may not be fully divided between the two output waveguides [161; 162].

The optical throughput in the L' band of the basic photonic components and beam combiners were measured using the supercontinuum source (SCS) and the *characterisation setup II* (see, Figure 3.3) for Sample III. The throughput was determined by first measuring the injection beam intensity, carefully aligning the sample and then measuring the intensities emerging from the individual outputs of the device under test. To reduce noise, each measurement contained a camera recording of 8 seconds duration at a recording frame rate set at 125 Hz (1000 frames in total).

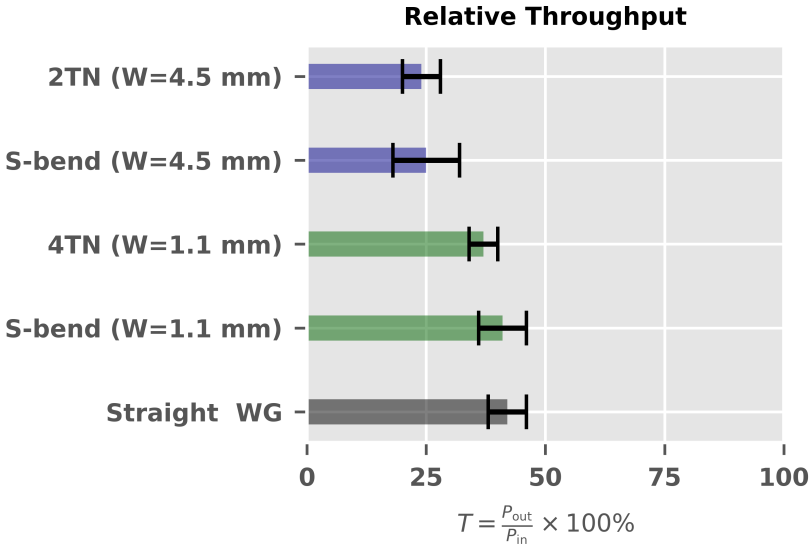

FIGURE 4.9: The bars present the relative throughputs of the devices found in SAMPLE III. The term WG denotes waveguides. The green bars represent S-bends with an amplitude (W) of 1.1 mm, where the S-bend refers to individual building block S-bends, and the 4T-Nuller includes S-bends designed for stray light suppression with the same amplitude. Similarly, the blue bars correspond to S-bends with an amplitude (W) of 4.5 mm for building block S-bends and Straylight suppressing S-bends inside the 2T-Nullers.

Figure 4.9 represents relative throughput values. To achieve these findings, 6 × triplet straight waveguides, 5 × side-step S-bends with an amplitude of 1.1 mm, 5 × side-step S-bends with an amplitude of 4.5 mm, along with 5 × 2T-Nullers and 1 × 4T-Nuller were utilised. The error bar associated with the 4T-Nuller was determined from the individual set of total outputs corresponding to each of the four inputs. Furthermore, this specific 4T-Nuller was selected for conducting nulling measurements for its central 50/50 achromat directional coupler, as elaborated in Chapter 6 and 8.

These values include the Fresnel losses, the coupling losses and all internal losses of the devices. The results reveal that straight waveguides exhibit throughput within the range of 42% ± 4%, and building block S-bends with an amplitude of 1.1 mm and a minimum radius of curvature of 45 mm demonstrate a throughput of 41% ± 5%. 4T-Nullers, which also incorporate identical S-bends of the same radius of curvature and amplitude to suppress stray light, demonstrated a transmittance of 37% ± 3%. These

results indicate that S-bends and 4T-Nullar have low bending losses, where Y-junctions and cascaded directional couplers add a fraction of loss.

In contrast, the large amplitude S-bends and 2T-Nullers exhibit a throughput of $25\% \pm 7\%$ and $24.5\% \pm 4\%$, respectively. These building block S-bends and the S-bends employed to suppress stray light are identical, with amplitudes of the S-bends being 4.5 mm, though the radius of curvature is 45 mm, which is similar to the previous set of building block and 4T-Nuller S-bends. Moreover, S-bends of 4.5 mm contain a length of $\sim$ 31.6 mm, which is nearly twice ($\sim$ 15.6 mm) the length of the S-bends of 1.1 mm. These S-bends are much longer than those S-bends previously fabricated and examined by T. Gretzinger [123].

Furthermore, these results facilitated the calculation of propagation losses for straight waveguides and basic building block S-bends with amplitudes of 1.1 mm and 4.5 mm. The calculation using the relation, $P_L = (1/L) \cdot (I_L - 2 \cdot F_L - C_L)$, where L represents the optical path length. This formula omitted consideration of bending and transmission losses due to previous studies demonstrating negligible bending loss for bend radii $>$ 40 mm and cosine S-bends exhibiting low transition loss [123]. Subsequently, a C_L value of approximately -0.897 dB was derived from the lunched beam spot size $\sim$ 10 μm (FWHM, in Chapter 3) $\approx$ 17 μm for $1/e^2$ beam width and the average mode-field diameter of the straight waveguide, demonstrated in Figure 4.3. A Fresnel loss per facet of -0.74 dB is also derived from 15.6% per facet. The calculated results indicate propagation losses for straight waveguides within the range of -0.21 to -0.29 dB/cm, S-bends with 1.1 mm amplitudes ranging from -0.21 to -0.29 dB/cm, and S-bends with 4.5 mm amplitudes approximately ranging from -0.35 to -0.47 dB. As depicted in Figure 4.9. The propagation loss ranges were determined using error bars.

These findings align closely with previously obtained results, where propagation losses of $\sim$ 0.47 dB/cm were recorded for single tracks, $\sim$ 0.33 dB/cm for double tracks at 3.39 μm, and at 4 μm, results showed losses of $\sim$ 0.29 dB/cm for single tracks and $\sim$ 0.22 dB/cm for triple tracks [150].

Thus, for the final beam combiner chip, the most feasible approach involves anti-reflection coating to mitigate the effects of Fresnel loss. It will increase the throughput

of the existing 4T-Nuller up to ∼ 53 %, around the level of throughput (≈ 50%) required for the NOTT, as mentioned in Table 4.1.

4.5 Optical microscope inspection

After the inscription, all samples were in detail inspected under an optical microscope. It was observed, depending on the glass batch, that nucleation sites were randomly distributed within the volume of the GLS glass samples. Some of the waveguides were partly or entirely traversing such pre-existing nucleation sites. The structure of written waveguides is strongly affected due to the presence of these nucleation sites, as illustrated in Figure 4.10.

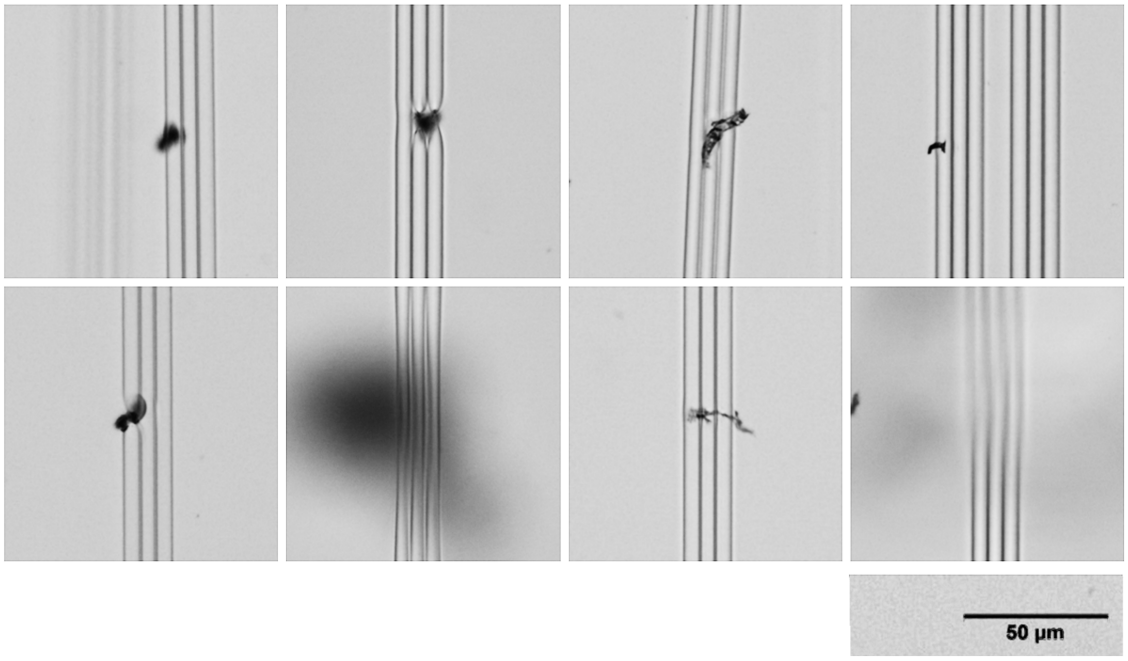

FIGURE 4.10: Sample optical microscope images of fabricated waveguides in GLS glass samples, revealing the existence of nucleation sites that negatively influence the waveguide inscription, resulting in neck-downs and gaps within the waveguides.

Nucleation sites can be common in crystal or glass materials. They are known to appear during crystallisation, which is associated with several phase transition processes [163]. By definition, a nucleus is the minimum amount of a new phase capable

of independent existence in a crystal [164]. However, the nature of nuclei, whether they are nebulous particles or tiny crystals, is still unknown [163]. Kashchiev and van Rosmalen [165] described nucleation as the process of random appearance of nanoscopically small clusters of a new crystalline phase, which can grow spontaneously to macroscopic sizes. The growth stage, which immediately follows nucleation, is governed by the diffusion of particles, called growth units, to the surface of the existing nuclei and their incorporation into the structure of the crystalline lattice [166].

L. Ruihua and A. B. Seddon [167] have reported the presence of nucleation sites in GLS glass. Their work discusses glass formation and the spontaneous appearance of nucleation sites during crystallisation processes. Further purification of the raw materials might improve the glass's quality. As described earlier, during this development process, two batches of the GLS glass materials were used for the ULI fabrication. Sample I and Sample IV were from the same batch of GLS glass, LD1765, while Sample II and Sample III were from batch LD1999. Batch LD1999 was specifically selected by D. Hewak from their stock at University of Southampton, because it features better quality and fewer nucleation sites than LD1765.

The impact of the presence of such nucleation sites is unpredictable, particularly in terms of throughput, i.e. the amount of loss a waveguide defect introduces. For instance, the error bars obtained from testing multiple straight waveguides and nulling devices have shown a relatively small variation, as depicted in Figure 4.9, regardless of the presence of nucleation sites. Unfortunately, due to the larger number of nucleation sites and their 3D distribution within the glass volume, it is nearly impossible to map their exact location and adjust the inscription location of the devices to minimise the number of waveguides colliding with the nucleation sites. Thus for the final beam combiner chip or future upgrade, the best approach is to inscribe a series of identical beam combiner devices, characterise them and select the one with the highest throughput.

5

Y-Junctions

Y-junctions are vital passive photonic components in modern integrated optical systems. These components provide a compact and efficient means of controlling and manipulating light for splitting or combining optical signals. Y-junction based power splitters play a crucial role in integrated optical devices related to the NOTT's instrumental requirements. These power splitters allow the achromatic division of optical signals into two branches. One branch is used for photometry, while the other is used for interferometry, as illustrated in the designs of 2T-Nuller and 4T-Nuller depicted in Figure 4.2. Y-junctions are favoured in these designs because of their relatively shorter length compared to directional couplers (see Chapter 6) to keep the photonic chip as small as possible and thus the losses as low as possible. Moreover, if appropriately designed, Y-junctions are inherently achromatic.

This chapter introduces the principles of Y-junctions, their role in power splitting

within integrated optics in the mid-infrared, and the ongoing efforts to attain achromatic power splitting of 20/80 in the contest of NOTT 4T-Nuller [20; 33]—in the mid-infrared L' band.

5.1 Y-Junctions as a splitter

As a splitter, a Y-junction relies exclusively on geometric design for its functionality. A typical Y-junction of 1×2 architecture consists of a stem and two diverging arms. Its light-splitting properties can be generalised based on tapers or the modification of mode-field propagation and the angle between the two arms. Y-junctions can be subdivided into two categories with variations in geometrical size and refractive indices of the arms, known as symmetric and asymmetric.

Y-junctions' approximate adiabatic propagation from the stem to the splitting arms in the axial direction is categorised into three groups: single-mode, few-mode, and multi-mode. The few-mode Y-junction has a broader stem that supports higher-order modes. After the waveguide branch, there are always two modes for a single-mode 1 × 2 Y-junction: (i) even mode, as shown in Figure 5.1 (top), and (ii) odd mode, where the field is shifted by π in one branch versus the other.

The detailed definitions and properties of the Y-junctions can be found in the article of J.D. Love and D. Riesen [168], where authors discussed each type with simulation-based demonstrations for silicon material and 1.55 μm wavelength.

However, in the context of the 4T-Nuller's Y-junction, an asymmetrical single-mode configuration is required. This configuration can split the fundamental mode into two same-phase phases (even mode) by tweaking a slight change of effective index between the stem and the arms.

Many studies have explored Y-junction fabrication using lithography and ultrafast laser inscription or ULI. Lithography offers scalability, cost-efficiency, and compact circuit design advantages, whereas ULI provides rapid-prototyping flexibility and quick device optimisation capabilities, which are often challenging to achieve with lithography [97; 169]. Historically, ultrafast laser inscription has been employed to produce

Y-junctions in various materials, such as Fused Silica [170], Lithium Niobate [171], and Bismuth Germanate crystals [132]. These Y-junctions operate across various wavelengths, covering from visible to mid-infrared, and serve purposes in optical communication and scientific applications [97].

The application of Guided Light Interferometric Nulling Technology (GLINT) in nulling interferometry with the Anglo-Australian Telescope showcased the utilisation of Ultrafast ULI in the fabrication of Y-junctions, which operates over a 50 nm bandwidth (centred at 1550 nm). These Y junctions were subsequently used in a 2-telescope integrated optical nuller, demonstrating the capability of ULI to inscribe efficient and achromatic power splitting for both interferometric and photometric purposes [90].

The findings from these studies collectively underscore the potential of ULI as a promising technique for Y-junction fabrication, particularly in the context of the design for NOTT Nullers (see Figure 4.2).

5.1.1 ULI Y-Junctions

ULI fabricated Y-junction splitters are designed based on a waveguide that is split into two arms via a *tapered transition region*. The tapered coupling region signifies a gradual transition in the cross-sectional dimensions of an optical waveguide. This transition aims to facilitate efficient optical power transfer from the stem of the Y-junction to the branch. Tapered coupling regions mitigate mode mismatches and minimise optical losses that may occur during the coupling process [131; 168].

One challenge of fabricating Y-junctions using ULI is achieving *symmetry*. Symmetry is crucial in ensuring that the fundamental mode in the stem equally excites the fundamental modes in both arms to achieve 50/50 splitting. An unbalanced power-splitting ratio can result from a lower refractive index change in the second inscribed arm, leading to an asymmetric power distribution [168]. Hence, *asymmetry* can be exploited to achieve achromatic 20/80 power-splitting ratios for the NOTT beam combiner.

Many researchers have explored various methods and techniques to achieve achromatic Y-junctions using ULI. Multiscan techniques have been utilised to produce achromaticity with rectangular geometry in fused silica, offering promising results in near-infrared at 1064 nm [172]. The *bending radii* introduce mismatching propagation constants between two splitting arms, resulting in mismatching propagation constants, which make the Y-junction asymmetric [173; 174]. The bending radii of the arms also form an *angle* between them concerning the rear edge where the junction occurs. This angle serves as a parameter to express the splitting ratios of the two arms [174].

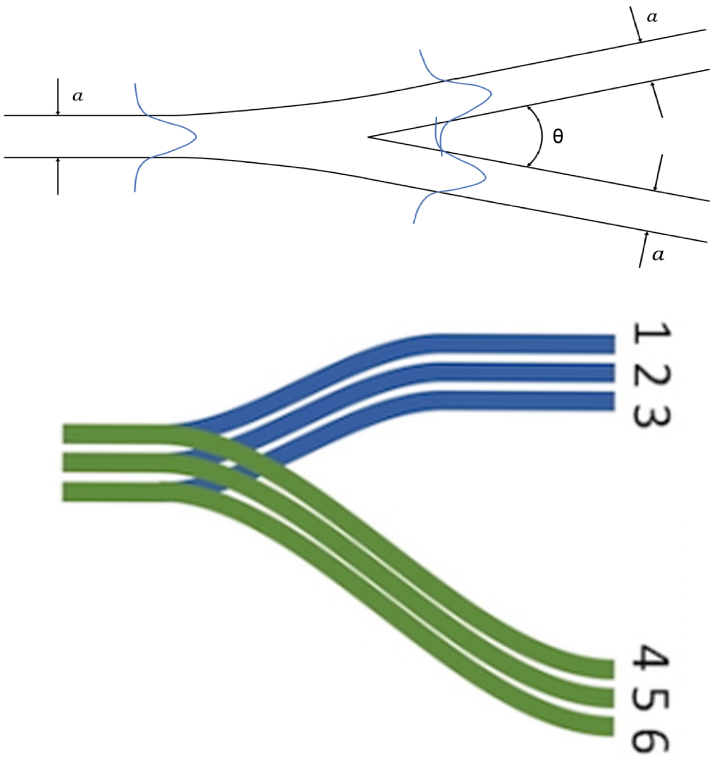

Figure 5.1: Top: Typical Y-junction based 1 × 2 splitter, where a is the diameter of the arms and θ is the angle between the splitting arms. Bottom: Y-junction specific to the triplet waveguides in GLS glass with the track inscription order (1 - 6) depicted. The green lines overpass the blue tracks during the inscription of the second branch, which influences the splitting ratio.

Cosine S-bends, as described in Equation (4.2), are utilised in the ULI to introduce

bending in the arms of the Y-junctions, to provide flexibility in geometry by ensuring that the split signals diverge further from the inputs within a shorter longitudinal dimension. Cosine S-bends are a good choice for Y-junctions due to their low loss property, as discussed in Chapter 4. Consequently, an increase in the radius of curvature implies a reduction in the intersection angle, θ. This relationship implies that for smaller angles, the size of the junction expands, potentially leading to an increased V-number. This increase in V-number may, in turn, introduce multimode features into the Y-junctions, governed by the formula $V = \frac{2\pi(a/2)}{\lambda}$ (NA), where a is the width of the waveguide junction core, λ is the wavelength, and NA represents the numerical aperture, expressed as $NA = \sin\theta_i$, where θ_i is the half angle of maximum cone of light that enters. The number of modes can be calculated using the relation, $M \propto V^2$ [160].

Gretzinger *et al.,* [150] developed mid-infrared Y-junctions in GLS glass using the triplet waveguides. Splitting ratios of 50/50, 60/40, and 65/35 were achieved by Y-junction splitters, which is away from the desired configuration of this project being 20/80. Additionally, it was also seen that the writing order of the waveguide tracks influences the refractive index difference in waveguides. Figure 5.1 (bottom) indicates the inscription order of the Y-junction that was found to be the most optimal and the least lossy Y-junctions in GLS glass, where the sequential fabrication of the tracks leads to overpassing the first three tracks (blue) a second time (green) up to the branching point. This same configuration has been used to write Y-junctions for the NOTT.

The splitting ratio can be tuned by changing the reflective index of an arm by lowering the *writing velocity*. Experimentally, this was demonstrated using UV laser writing to tune the splitting ratio between 70/30 and 30/70 [175]. It indicates that adjusting the writing velocity can offer possible achromatic splitting using the direct laser writing technique.

5.2 Y-Junctions in the 2T/4T-Nullers

SAMPLE I to III contain 4T-Nullers, whereas SAMPLE II and III contain functional 4T-Nullers. Therefore, the Y-junctions of these two samples were extensively characterised.

Besides, Sample III also contains 2T-Nuller. A 4T-Nuller is incorporated with 4× Y-junctions, and 2× Y-junctions are incorporated in 2T-Nullers for photometry and interferometry signal separation. Left to right triplet waveguides were used to write these Y-junctions, and these Y-junctions are not identical by design. Y-junctions of 2T-Nullers are planer or 2D, and Y-junctions of 4T-Nuller have 3D structure.

The arm of the Y-junction is used for photometry. In the case of the 4T-Nullers, this arm descends from the plane of the interferometry section downward, employing a cosine S-bend with a 45 mm bend radius. This 3D arrangement takes advantage of ULI's capabilities to avoid waveguide crossing, that introduces cross-talk. Cross-talk is detrimental to high contrast nulling. This descending arm extends upward again after the Y-junctions to form a linear array with all other waveguides at the output. The direction of the photometry channels of the Y-junction can either be to the left or to the right, according to the respective input (see Figure 5.2).

However, in the case of the 2T-Nuller, this photometry arm does not go downward, it goes either left or right from the interferometric within the same plane using a cosine S-bend of a 100 mm bend radius. In contrast to the 4T-Nullers, the 2T-Nullers are purely planar, as the 2T-Nuller does not require 3D waveguides to avoid crossing.

The arm of the Y-junctions splits the signal and directs one part to the interferometry section, i.e. the directional couplers. The design of the directional couplers dictates another cosine S-bend with a minimum radius of curvature of 50 mm. For the 4T-Nuller of Sample III, a 3 mm straight section is added right before these S-bends with an aim to provide more light for the interferometry, as seen in Figure 5.2.

These Y-junctions incorporate a 1 mm length of tapered straight section over which the first waveguide is tapered to avoid creating any damage and then overwritten by the second waveguide. Architectural details of these Y-junctions are summarised in Table 5.1.

TABLE 5.1: The parameter of Y-junctions in tn the 2T/4T-Nullers. S-bend radii [I] and S-bend radii [P] represent the minimum radius of curvature of the S-bends of photometry and interferometry arms, respectively

Photonic Chip	S-bend radii [I]	S-bend radii [P]	Straight Section	Type
Sam.II (4T-Nuller)	50 mm	45 mm	No	3D
Sam.III (4T-Nuller)	50 mm	45 mm	3 mm	3D
Sam.III (4T-Nuller)	50 mm	100 mm	No	Planner

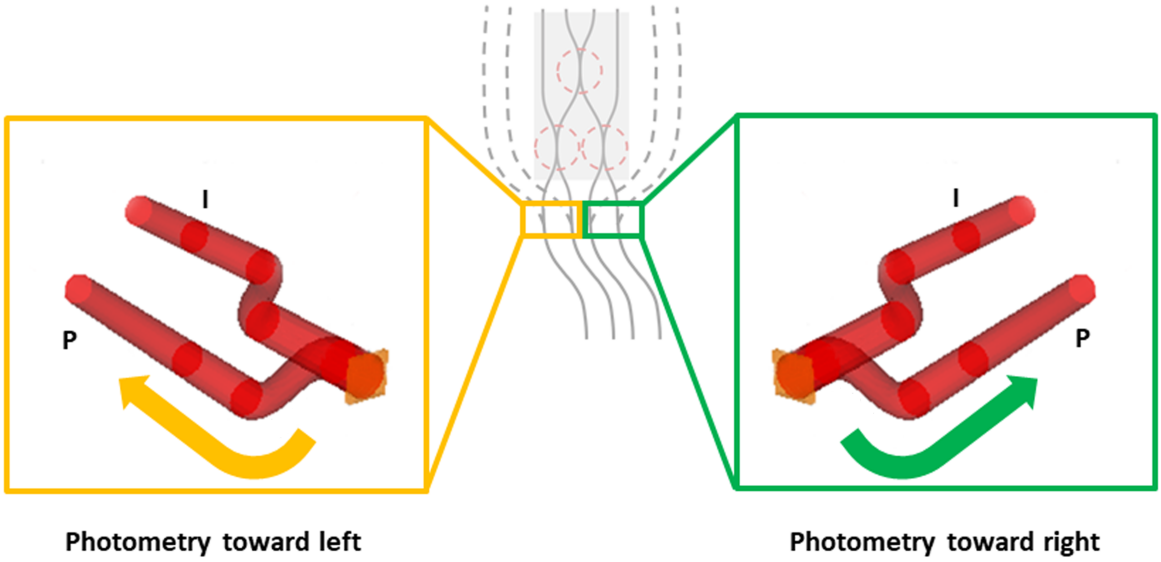

FIGURE 5.2: Sketch of the Y-junctions within the 4T-Nuller (generated using RSoft). The 3D diagram shows that the photometry arms extend downward from the interferometry plane and turn to the left or right, depending on the input. The dashed lines in the schematic diagrams delineate the photometry channels. These channels gradually extend upward after the Y-junction so that their outputs from a horizontal line with the interferometric outputs, as illustrated in Figure 4.7.

5.2.1 Characterisation results

The chromatic splitting ratios of the Y-junctions of the 2T/4T-Nullers were measured using Fast Fourier Transform (FFT) spectroscopy for the L' astronomical band (test bench in Figure 3.3) using the mechanism explained in Chapter 3. Across the bandwidth, the calculation of the splitting ratios between photometry and interferometry was obtained using the relations P/(P + Σ I) and I/(P + Σ I), respectively. P refers to the spectrum from the photometric output, and ΣI is the summation of all the interferometric output within the same spectral bandwidth.

Characterisation of the Y-junctions of Sample II suggests that the average splitting between all the photometry and interferometry signals of the 4T-Nullers at 3.75 μm is 37/56 with an error bar of 11/7 [35]. The splitting ratio at 3.75 μm, the central wavelength of the L' band, has been considered for demonstration. Regardless of the geometrical and designing differences, as described in Table 5.1, Y-junctions of 2T/4T-Nullers demonstrate a similar range of splitting ratios between photometry and interferometry arms as plotted in Figure 5.3 for Sample III. These results are also comparable to the Y-junctions of Sample II.

The photometry arms of the Y-junction extend to the left direction for the T1 input of the 2T-Nuller or for both the T1 and T2 inputs of the 4T-Nuller, while they extend to the right for the T2 input of the 2T-Nuller or the T3 and T4 inputs of the 4T-Nuller (see Figures 7.2 and 8.2). Interestingly, the splitting behaviours, as depicted in Figure 5.3, reveal a directional dependency for the 2T/4T-Nullers. The most likely explanation for this dependency is the writing order, which warrants further investigation.

Despite the directional dependency of $\sim$ 10%, all Y-junctions exhibit achromaticity across the L' astronomical band. The chromatic splitting ratio of the Y-junction of 2T-Nuller has been exemplified in Figure 5.4. This example is provided because these photometry channels of this specific 2T-Nuller were utilised to perform nulling interferometry in Chapter 7.

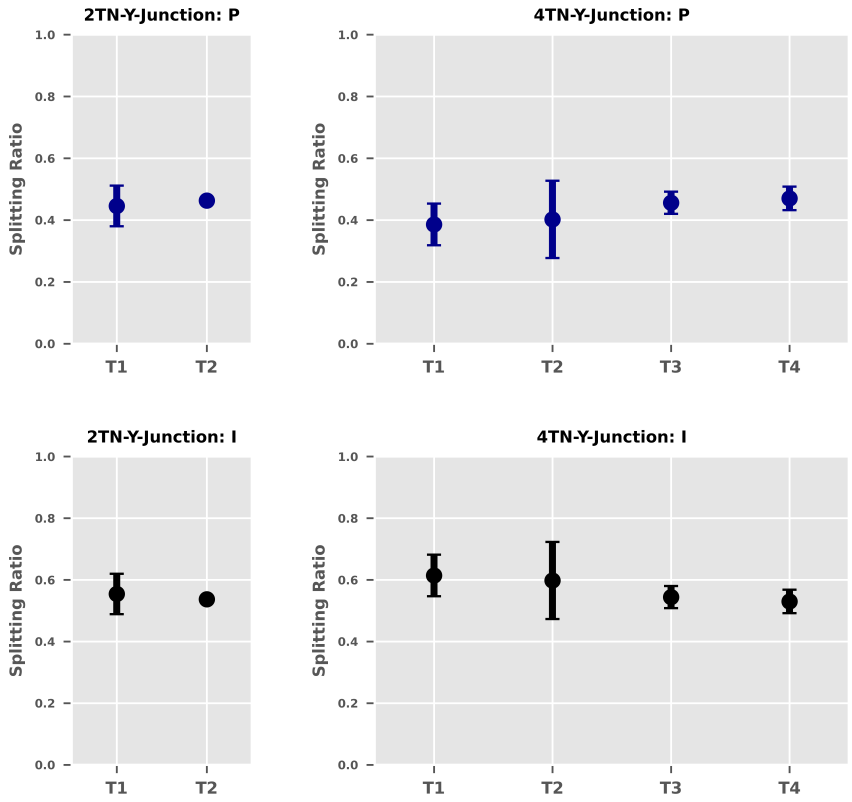

Figure 5.3: The left column illustrates the average splitting between photometry (P) and interferometry (I) measured and averaged across five Y-junctions of the 2T-Nullers contained in Sample III. T1 and T2 are the left and right inputs, respectively. All data is for a wavelength of 3.75 μm. The right column shows the same data for the 4T-Nullers, also for Sample III. T1 and T2 are left-handed Y-junctions, while T3 and T4 are right-handed Y-junctions. The error bars depict the error of the mean for the average values.

Despite the differences between 4T-Nuller and 2T-Nuller, such as 3D and 2D, all Y-junctions are achromatic splitters of $\sim 40/60$, and neither of them is close to 20/80 in terms of photometry and interferometry separation, a key requirement of the 4T-Nuller of NOTT. Therefore, further optimisation was implicated, particularly by modifying the design of the Y-junctions.

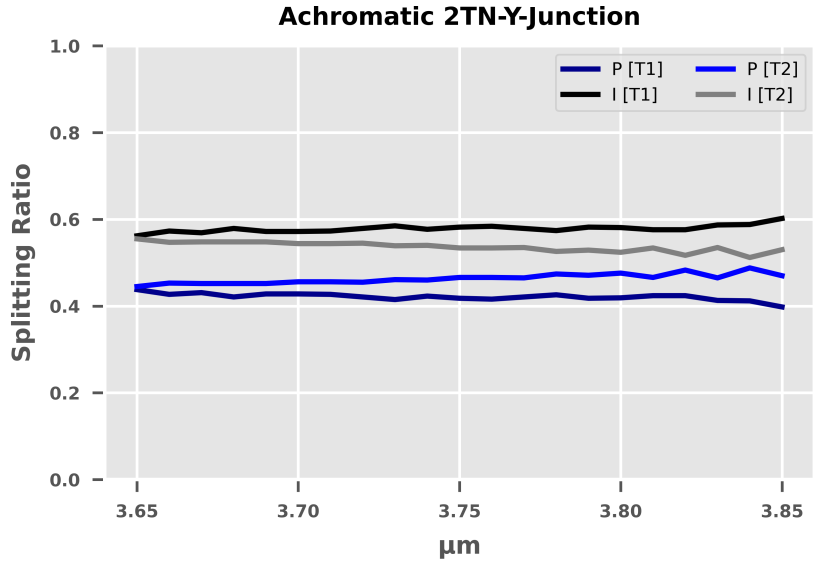

Figure 5.4: The graph depicts the splitting characteristics of the Y-junction of one 2T-Nuller from Sample III.

5.3 Optimising Y-Junctions for NOTT

5.3.1 Simulation

Further modification of the Y-junction geometry is necessary to address the challenge of achieving achromatic 20/80 Y-junctions for the 4T-Nullers. Before fabricating more devices, simulations utilised RSoft BeamPROP were conducted. In order to tailor the splitting ratios, the Y-junctions found in Sample II and III were modified. The Y-junctions in Sample II always followed the conventional design, where two S-bends originate from the common stem, as outlined in Table 5.1. The Y-junctions in Sample III can be seen as a variation of Sample II, where the waveguide leading towards the directional couplers for interferometry is a straight section, i.e. an S-bend with infinite radii of curvature, to facilitate more light coupling towards the interferometry. Despite these changes, the required 20/80 splitting was still not achieved. Therefore, the waveguide for the photometry was further decoupled by introducing a vertical shift. The 3D geometry of the modified Y-junctions is shown in Figure 5.5 where Model I is based on Sample II, and Model II is based on Sample III.

MODEL I holds to the conventional design of Y-junctions, where the S-bends of the two arms closely connect photometry and interferometry channels. On the other hand, MODEL II introduces an advancement design in which the cosine S-bend of the photometry channel descends before the position of the cosine S-bend of the interferometry channel. The existing Y-junctions of 4T-Nullers contain such designs.

To provide a gradual transition between the two waveguides, the photometry arm was tapered up over a distance, and the radius of curvature of the S-bend for the photometry arm and for the interferometry was 50 mm.

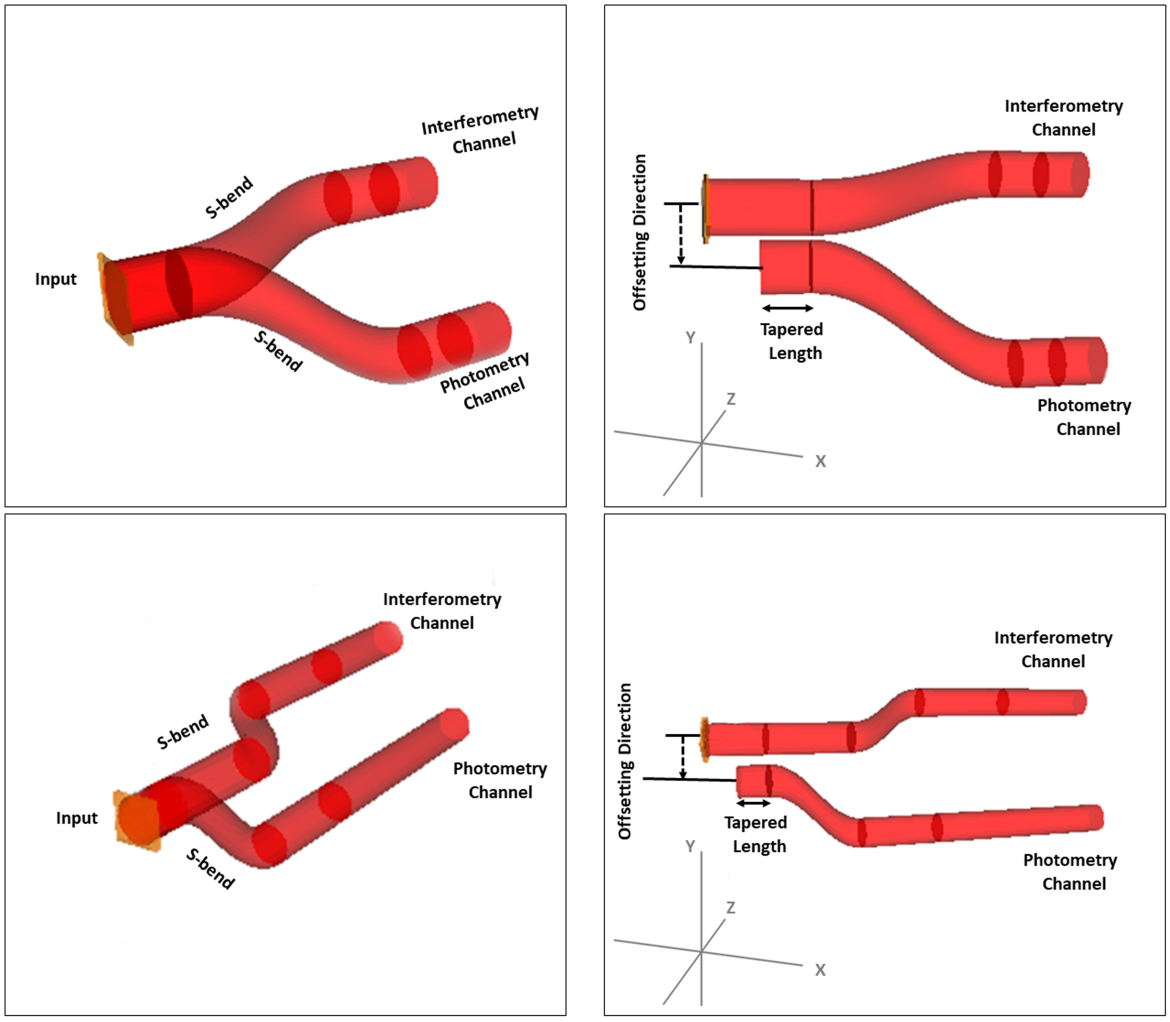

FIGURE 5.5: RSoft designed Y-junction of MODEL I is on the top row, and MODEL II is on the bottom row. The left column corresponds to the basic diagram of the two models. The Right column demonstrates the parameters tweaked in 3D to identify 20/80 achromatic splitting ratios.

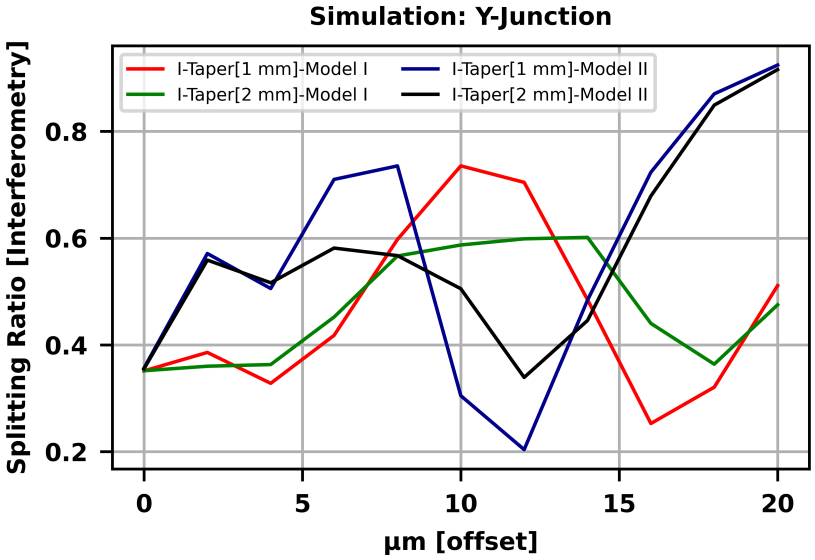

Figure 5.6: Simulation results illustrating the variation in splitting ratios of the interferometry channel based on the taper length and the vertical offset between the two waveguides at the branching point. The simulation wavelength is 3.75 μm. The graph shows an oscillatory behaviour in splitting ratio versus vertical offset. Offset $>$ 15 μm is required to achieve the desired 20/80 splitting. As one would expect, with increasing offset, less and less light couples into the photometry branch.

The primary objective of the simulations was to identify any trends that could lead to achromatic 20/80 splitting ratios. However, it was acknowledged that the manufacturing results might not precisely mirror the simulations due to inherent differences. RSoft models are designed using the triplet refractive index profile that was formerly obtained for 3.8 μm, whereas the physical mode-field profile of Ultrafast Laser Inscription (ULI) in the GLS glass sample exhibits triplet structures [151], as shown in Figure 4.1.

The simulations showed that varying the minimum radius of curvature from 45 mm to 145 mm of the S-bend for the photometry arm does not provide sufficient change in the splitting ratios for Model I but interferometry arm reaches nearly 75% for $>$ 105 mm. However, Promising trends were identified when introducing a vertical offset that places the start of the photometry branch deeper within the sample, as depicted in Figure 5.6. Testing different taper lengths between 1 mm and 2 mm

showed only a marginal influence. The simulations indicate that achieving an 80% signal in the interferometry channel is very sensitive to changes in the vertical offset of the photometry branch. An offset between 5 and 10 μm demonstrated a significant rise in the signal in the interferometry arm for both MODEL I and MODEL II with a throughput range between 80-94% and 91-95%, respectively. Besides the improved splitting ratios in accordance with the instrument requirements, the change in geometry maintained the achromatic behaviour of the Y-junctions.

5.3.2 Experimental results

To test the simulated Y-junction geometries, an additional sample was fabricated SAMPLE IV. Based on the simulations, the following parameters were chosen for fabrication:

- MODEL I: photometry branch's radius of curvatures = 45 mm, taper length and vertical offset are varied.
- MODEL II: photometry branch's radius of curvatures = 45 mm, 75 mm, 100 mm, 125 mm, and 150 mm, with taper length = 1 mm and no vertical offset.
- MODEL II: photometry branch's radius of curvatures = 45 mm, taper length and vertical offset are varied.

In accordance with the design of the 4T-Nuller, for every design, two Y-junctions were fabricated, one left-handed and one right-handed. Furthermore, as a reference also, Y-junctions based on the design used for the 4T-Nullers in SAMPLE III were included in SAMPLE IV.

During the characterisation, broadband splitting ratios are first identified by launching one beam of L' band into the input of the Y-junctions and measuring the photometry (P) and interferometry (I) splitting ratios as P/(P+I) and I/(P+I).

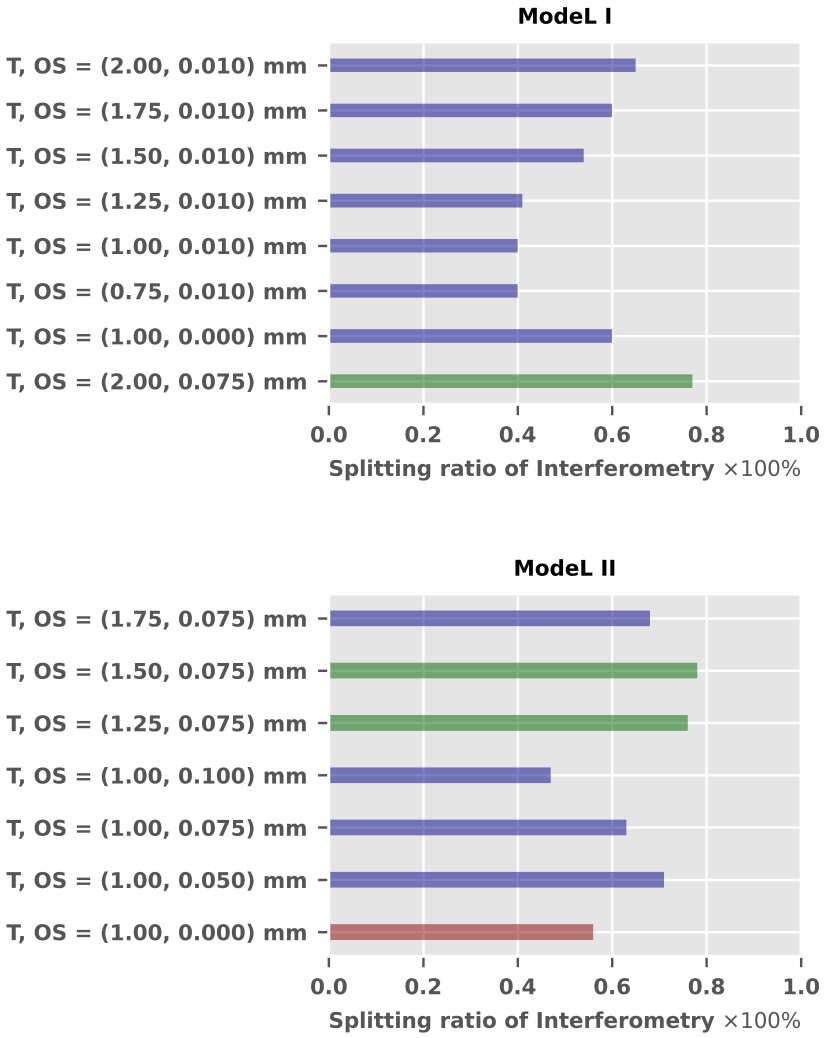

Figure 5.7: Broadband splitting ratios of ModeL I and ModeL II Y-junctions with varying taper length (T) and vertical offset (OS) for their interferometry branch. Exhibiting green-coloured splitting ratios are being considered promising candidates for the 4T-Nuller. Y-junction's ratio with the red colour contains parameters similar to those of existing Y-junctions in the 4T-Nuller. All of these Y-junctions' radius of curvature of photometry is 45 mm.

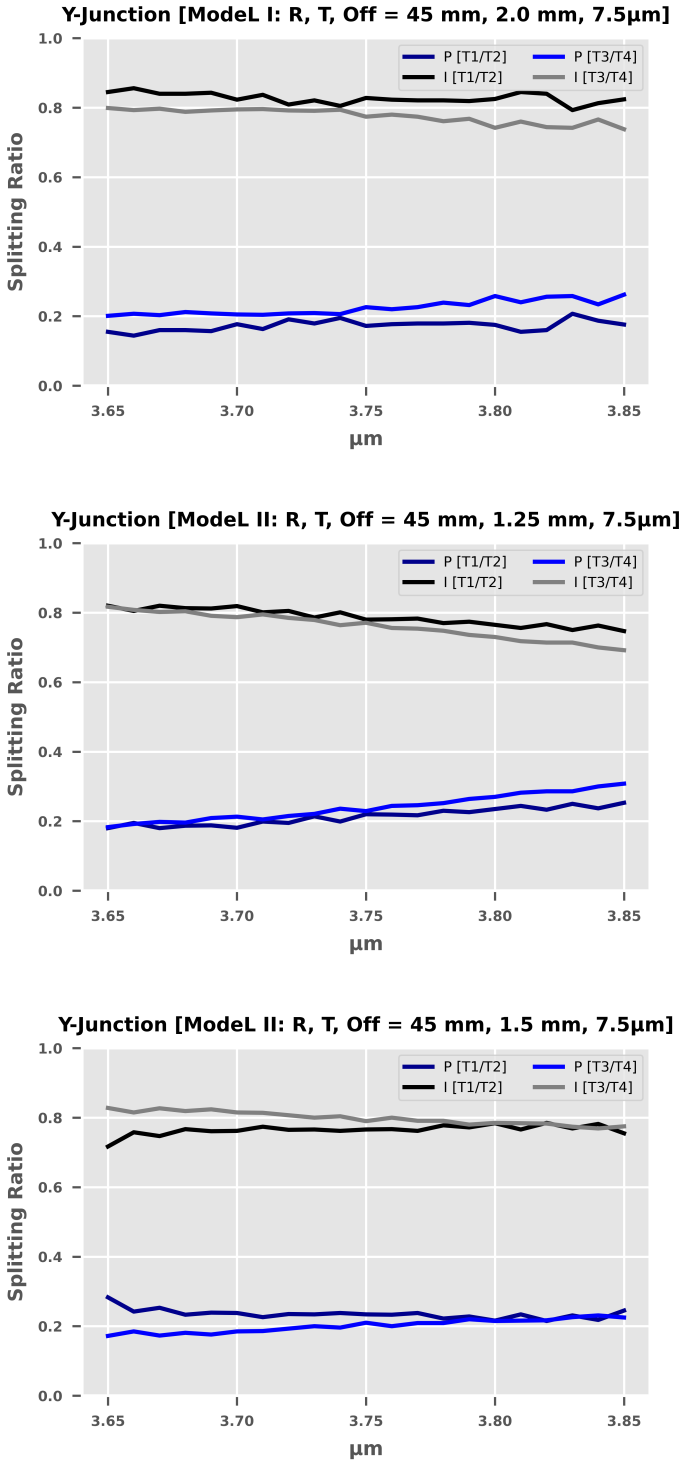

Figure 5.8: Wavelength resolved splitting ratios across the L' band for the 3 Y-junctions in Sample IV. See the text or graph titles for the differences in geometry. These Y-junctions demonstrate achromatic splitting and relatively small variation between left-handed (TI/T2) and right-handed orientation (T3/T4).

Model II with the increment of the radius of curvature of the photometry branch did not demonstrate a higher imbalance in splitting ratios as it was seen in the simulation. A possible reason is that simulations cannot always handle partially overlapping refractive index profiles such as the ULI profile of Figure 5.1.

However, Model I and Model II with a varying taper and vertical offset demonstrated some promising interferometry and photometry imbalance in broadband, as found in the simulation. Figure 5.7 shows the splitting ratios of the Y-junctions (left-handed) from the interferometry branch. Green-coloured splitting ratios ($\sim$ 20/80) are being considered promising candidates for the 4T-Nuller, where the Y-junction of the red colour splitting ratio is identical to those of existing Y-junctions in the 4T-Nuller. The results highlighted three candidates capable of demonstrating 20/80 splitting ratios, one based on Model I and two based on Model II.

Fast Fourier transform spectroscopy was used to characterise the selected Y-junctions. For Model I, a taper length of 2 mm and vertical offset of 7.5 μm exhibited the desired achromatic 20/80 splitting ratios. For Model II, taper lengths of 1.25 mm and 1.50 mm, both with a 7.5 μm offset, demonstrated the desired achromatic splitting ratios. Three of the results are depicted in Figure 5.8.

Important for the beam combiners is that the Y-junctions do not introduce excess losses. This not only means loss of photons and thus the necessity for longer observations but also can contribute to unwanted stray-light in the chip. Thus, the throughput of the three Y-junctions in Sample IV with the correct splitting ratios was measured and compared to the Sample III design Y-junctions also contained in Sample IV. The throughputs were measured using the same technique as used for the photonic building blocks and nullers presented in Chapter 4.

Figure 5.9 demonstrates the comparison between the Y-junctions within Sample IV, where the average of all modified Y-junctions of Model II [new] appears to have higher transmittance compared to Model I [new] and the existing 4T-Nuller Y-junctions identified as Model II [old].

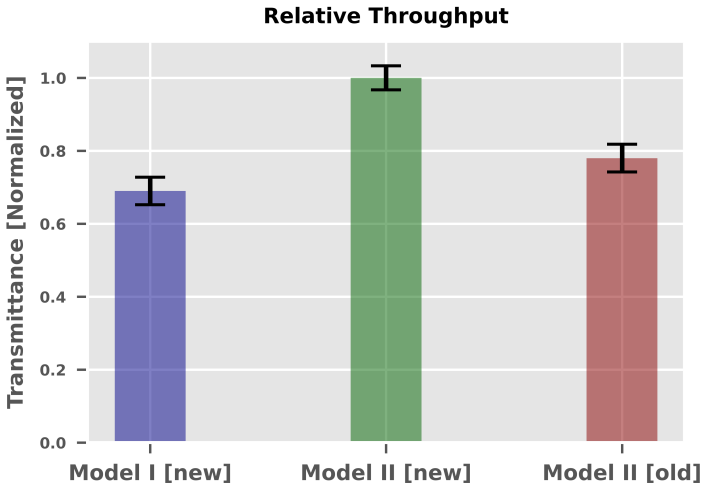

Figure 5.9: Within the Sample IV, Y-junctions of 45 mm radius of curvature in the photometry branch are classified into three categories, and by averaging, their throughputs are represented. (i) Model I [new] and (ii) Model II [new], for all of the Y-junctions, were fabricated with different taper and vertical offset. (ii) Model II [old] refers to the particular Y-junction which is equivalent to existing Y-junctions inside the 4T-Nullers of Sample III.

The Y-junction based on ModeL II with taper length of 1.50 mm and vertical offset 7.5 μm has the least variation between left-handed and right-handed orientation compared to ModeL II competitor and also has higher transmittance profile compare 20/80 Y-junction of ModeL II. Therefore, this Y-junction will be implemented in the next 4T-Nuller, which will ensure high transmittance and 20/80 achromatic splitting.

6

Directional Couplers

The performance of the nulling interferometers across the L' band relies on achromatic splitting and combining multiple telescope signals. The achromatic directional couplers (DC) are the key photonic components that determine the performance of the *single-* or *double-Bracewell* nulling interferometers, i.e. the 2T-Nuller and 4T-Nuller. Precise control of the optical path length or phase allows one to perform interferometric nulling, ensuring that the starlight and the unwanted scattered or reflected light destructively interfere at the directional coupler. This has been demonstrated using ultrafast laser inscribed 3D waveguides in the astronomical H-band (1.3 - 2 μm) for the GLINT instrument [90; 76] based on a *single-Bracewell* architecture.

A similar beam combiner, also fabricated using ULI, has recently been demonstrated for the K-band (2 - 2.4 μm) [176]. A more elaborate *double-Bracewell* architecture with three cascaded directional couplers was also reported and examined for the visible

wavelength of $\lambda = 633$ nm [177]. The ability to fabricate beam combiners spanning from the visible to the infrared spectrum demonstrates the versatility of ULI.

This chapter introduces laser-written directional couplers, their optimisation via simulation and experiment, and detailed characterisation of the chromatic splitting behaviour leading to optimised directional couplers that satisfy the NOTT requirements.

6.1 Waveguide directional couplers

To mathematically describe and model the behaviour of coupled optical waveguides and modes, one can use Coupled Mode Theory (CMT) [178]. CMT can describe two types of coupling: (1) evanescent field coupling between modes of adjacent waveguides, including directional couplers, power dividers, modulators, and switches, and (2) coupling between modes within the waveguide resulting from periodic index perturbations, such as fiber Bragg gratings and long period gratings [179].

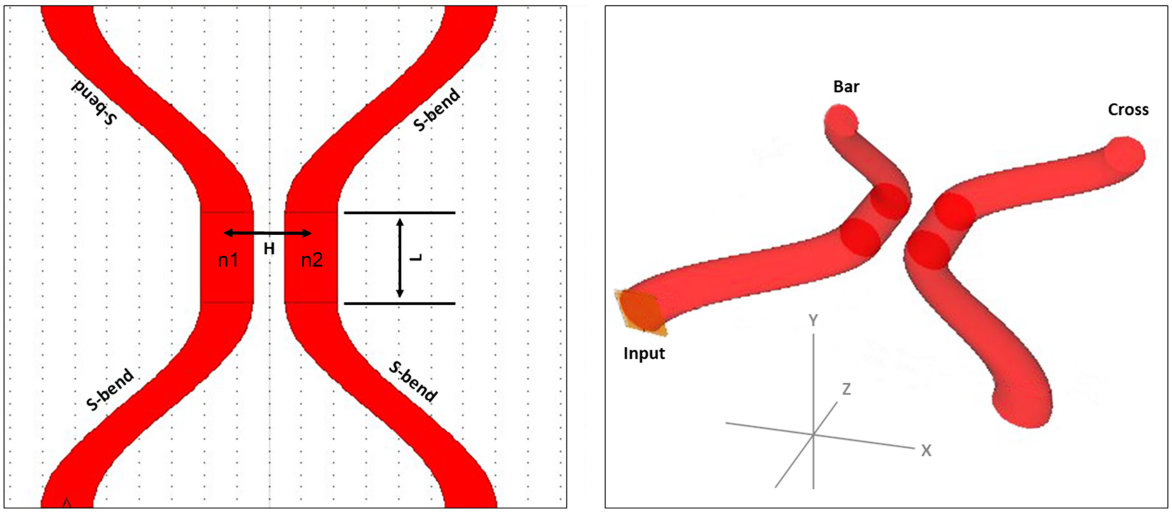

FIGURE 6.1: The left image illustrates a top view of a 2×2 directional coupler, showcasing the centre-to-centre separation H between the two parallel waveguides in the coupling region. The two waveguides feature refractive indices of n_1 and n_2, respectively. Four S-bends lead in and out of the coupling region. On the right, a 3D representation of the directional coupler with the labels *Bar* and *Cross* for a given *input*. Both images originate from RSoft CAD.

Directional couplers operate based on the evanescent field coupling between two closely spaced waveguides. Figure 6.1 illustrates a directional coupler created in RSoft

CAD for performing beam propagation simulation. The proximity region, separated by H with an interaction length L, facilitates the coupling of light through the evanescent fields. This allows for power exchange between the waveguides. A formal solution of Maxwell's wave equations with appropriate boundary conditions can be obtained to comprehensively describe the coupled waveguide geometry, resulting in the identification of super-modes for the coupled structure. For the directional coupler, one can assume that the individual waveguides are single-mode and the power exchange between the coupled waveguides is lossless. Thus, Equations (6.1) can describe the three-dimensional propagation of light according to its electric and magnetic field within the directional coupler. Here, $A(z)$ and $B(z)$ represent the amplitudes along the propagation direction, z axis, for the left ($WG1$) and right ($WG2$) waveguides, respectively. $E(x, y)$ and $M(x, y)$ are the transverse electric and magnetic spatial field profiles of the propagating light. The propagation constants of $WG1$ and $WG2$ are denoted by β_1 and β_2, respectively. They can be expressed in terms of the effective refractive index n_{eff} and wavelength as $\beta = n_{\text{eff}}.k_0$, where $k_0 = \frac{2\pi}{\lambda}$.

$$\begin{aligned} E(x, y, z) &= A(z)E_1(x, y)e^{-j\beta_1 z} + B(z)E_2(x, y)e^{-j\beta_2 z} \\ M(x, y, z) &= A(z)M_1(x, y)e^{-j\beta_1 z} + B(z)M_2(x, y)e^{-j\beta_2 z} \end{aligned} \tag{6.1}$$

According to electromagnetic principles, a travelling electric field E is always accompanied by a travelling magnetic field M with the same wave frequency and propagation constant but in an orthogonal direction. In the case of propagation, the electric field component is primarily considered due to its interaction with molecules or ions with the medium or waveguide, thereby giving rise to various effects, e.g. polarisation. Therefore, only E required to describe the propagating optical field instead of using both the electric and magnetic fields [160].

In general, directional couplers can be classified into two types: symmetric and asymmetric, based on the dephasing parameter $\Delta\beta = |\beta_1 - \beta_2|$ [180]. When $\Delta\beta = 0$ or $\beta_1 = \beta_2$, the coupler is considered symmetric,where $WG1$ and $WG2$ have identical optical properties. $\Delta\beta \neq 0$ or $\beta_1 \neq \beta_2$ indicates an asymmetrical directional coupler. This means $WG1$ and $WG2$ in the interaction region L have uniform but different

propagation constants, which can be achieved through variations in the waveguide's cross-section and/or refractive index contrast [179].

Using Equation (6.1), the power carried by the light propagating in $WG1$ and $WG2$, P_{WG1} and P_{WG2}, respectively, can be expressed in terms of amplitudes $A(z)$ and $B(z)$ and their complex conjugates $\overline{A(z)}$ and $\overline{B(z)}$ using Equation (6.2).

$$\begin{aligned} P_{WG1}(z) &= A(z) \cdot \overline{A(z)} = |A(z)|^2 \\ P_{WG2}(z) &= B(z) \cdot \overline{B(z)} = |B(z)|^2 \end{aligned} \tag{6.2}$$

Constructing a second-order differential equation for considering only $A(z)$ as defined in Equation (6.3) is also possible.

$$\frac{d^2A}{dz^2} - j\Delta\beta\frac{dA}{dz} + \kappa^2 A = 0 \tag{6.3}$$

This second order-differential equation can be solved for $A(z)$ and $B(z)$ using the initial condition $A(0) = A_0$ and $B(0) = B_0$ [179], and the solutions can be written in matrix form as described in Equation 6.4.

$$\begin{bmatrix} A(z) \\ B(z) \end{bmatrix} = \begin{bmatrix} cos(\gamma z) + j\left(\frac{\Delta\beta}{2\gamma}\right)\sin(\gamma z) & -j\left(\frac{\kappa}{\gamma}\right)\sin(\gamma z) \\ -j\left(\frac{\kappa}{\gamma}\right)\sin(\gamma z) & cos(\gamma z) + j\left(\frac{\Delta\beta}{2\gamma}\right)\sin(\gamma z) \end{bmatrix} \begin{bmatrix} A_0 \\ B_0 \end{bmatrix} \tag{6.4}$$

Where $\gamma = \sqrt{\left(\frac{\Delta\beta}{2}\right)^2 + \kappa^2}$ and

κ represents the coupling coefficient, which defines the coupling between the two waveguides based on their electric field overlap.

If $\Delta\beta = 0$, the directional coupler is symmetric and Equation (6.4) can be simplified to Equation (6.5).

$$\begin{bmatrix} A(z) \\ B(z) \end{bmatrix} = \begin{bmatrix} cos(\gamma z) & -j\left(\frac{\kappa}{\gamma}\right)\sin(\gamma z) \\ -j\left(\frac{\kappa}{\gamma}\right)\sin(\gamma z) & cos(\gamma z) \end{bmatrix} \begin{bmatrix} A_0 \\ B_0 \end{bmatrix} \tag{6.5}$$

For the asymmetrical directional coupler, Equation (6.4), if it is assumed that the initial power is launched into one waveguide such that $P_0 = A_0$, and the second waveguide is dark, i.e. $B_0 = 0$ on can obtain the solution$A(z) = A_0.[cos(\gamma z) + j\left(\frac{\Delta\beta}{2\gamma}\right)\sin(\gamma z)]$ and $B(z) = A_0.[-j\left(\frac{\kappa}{\gamma}\right)\sin(\gamma z)]$.

Looking at Figure 6.1, if the power P_0 is launched into $WG1$, then the corresponding output powers P_{bar} and P_{cross} can be calculated by using a pair of Equations(6.6) as a function of interaction length L with the help of the Equation (6.2).

$$\begin{aligned} P_{cross}(L) &= P_0 \cdot \left(\left[1 + \left(\frac{\Delta\beta}{2\kappa} \right)^2 \right]^{-1} \sin^2(\gamma L) \right) \\ &= P_0 \cdot \sigma \cdot \sin^2(\gamma L) \\ P_{bar}(L) &= P_0 - P_{cross}(L) \\ &= P_0 \cdot \left(1 - \sigma \cdot \sin^2(\gamma L)\right) \\ &= P_0(1-\sigma) + P_0 \cdot \sigma \cdot \cos^2(\gamma L) \end{aligned} \tag{6.6}$$

Here, $\sigma = \left[1 + \left(\frac{\Delta\beta}{2\kappa} \right)^2 \right]^{-1}$ is introduced to simplify the equation.

Equations(6.6) simplify for symmetric directional coupler with $\Delta\beta = 0$ to Equations (6.7)

$$\begin{aligned} P_{cross}(L) &= P_0 \cdot \sin^2(\kappa L) \\ P_{bar}(L) &= P_0 \cdot \cos^2(\kappa L) \end{aligned} \tag{6.7}$$

It is obvious from the equations that both symmetric and asymmetric couplers have sinusoidal exchanges of powers between their evanescently coupled waveguides with respect to the interaction length L. However, the symmetric couplers can facilitate the full power exchange from one waveguide to another, as seen in Figure 6.2. The difference in propagation constants in asymmetric directional couplers limits the maximum amount of power exchange to values less than 1. Furthermore, Figure 6.2 also illustrates the periodic back-and-forth coupling of light as L increases. Thus, there are many possible length values of L to achieve 50/50 power splitting between *bar* and *cross*.

Using the relation between P_{bar} and P_{cross} of the asymmetrical coupler, the splitting ratio can also be calculated using the Equation 6.8, used by Chen *et al.,* [181] and extended by and Diener *et al.,* [180] with an additional phase term.

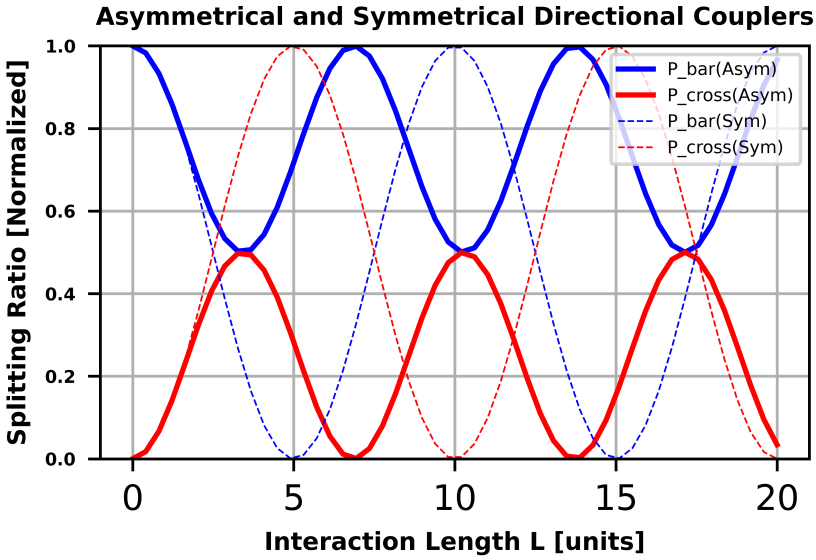

FIGURE 6.2: The two outputs (P_{bar} and P_{cross}) of a symmetric (dashed lines) and asymmetric directional coupler (solid lines) as a function of interaction length L which is produced using equations (6.6) and (6.7).

$$\frac{P_{cross}(\lambda)}{P_{bar}(\lambda) + P_{cross}(\lambda)} = \sigma^2 \cdot \sin^2(\frac{\kappa}{\sigma}L + \phi) \tag{6.8}$$

The additional term, ϕ is a phase term that accounts for light coupling within the S-bends leading into the coupling region. It has a significant contribution to the coupler's response and can be exploited to achieve achromaticity [182; 183; 184]. A simplified Equation (6.9) can be constructed from Equation (6.8), where $A = \sigma^2$ represents the maximum power coupling ratio and $C_{eff} = \kappa/\sigma$ represents the effective coupling coefficient.

$$\frac{P_{cross}(\lambda)}{P_{bar}(\lambda) + P_{cross}(\lambda)} = A \cdot \sin^2(C_{eff}L + \phi) \tag{6.9}$$

For a directional coupler to exhibit a broadband-flattened or achromatic response, $C_{eff}(\lambda)L + \phi(\lambda)$ requires to be constant across the wavelength range of interest. Otherwise, it will eventually lead to an imperfect dispersion cancellation. According to Equation 6.9, symmetric couplers are highly sensitive to imperfect dispersion cancellation around the $\pi/2$ phase point. Therefore, obtaining the broadband 50% splitting

by symmetric directional couplers is difficult compared to asymmetric directional couplers. The following simplified procedures can design asymmetrical couplers using: (i) considering $L = 0$, (ii) adjusting waveguide separation, H, to minimise dispersion in A and C_{eff} terms for an overall achromat/flat response across the bandwidth, (iii) Tuning L to adjust the coupling ratio. More details of this procedure in terms of the ULI manufacturing process are discussed by Chen *et al.,* [181]. Olivero *et al.,* [185] also demonstrated an alternative method for asymmetrical directional couplers using the UV direct laser writing technique. Their approach involved introducing high dephasing to restrict maximum power transfer to 50%.

In the context of this study, an alternative approach has been employed to fabricate asymmetrical directional couplers by lowering the feedrate to introduce asymmetry [150], as described in the following section.

6.2 Fabrication and optimisation chronology

In pursuit of the NOTT project requirements, an extensive range of asymmetric directional couplers across all GLS samples were manufactured and characterised. To find the optimal parameters and gain an understanding of reproducibility, reference directional couplers with different coupling region lengths were inscribed into the samples. Furthermore, all beam combiners, 2T-Nullers and 4T-Nullers, contain directional couplers that were investigated. The chromatic splitting ratios of these directional couplers have been experimentally determined across the 3.65-3.85 μm wavelength band utilising the Fast Fourier Transformation (FFT) Spectroscopy. Hereafter, the cross-coupling ratio or splitting ratios of the manufactured directional couplers were calculated according to $P_{cross}/(P_{cross} + P_{bar})$, where P_{bar} is the measured power that remained in the injection waveguide and P_{cross} is the power emerging from the opposite waveguide, i.e. the light that has coupled across.

The work began with directional couplers of 4T-Nullers from Sample I, and it was observed that one of the optical waveguides did not function properly for all of the nullers due to sub-optimal writing order. Afterwards, Sample II was fabricated,

which contains 7× 4T-Nuller with 5.0 to 6.2 mm coupling lengths with a step of 0.2 mm. Each 4T-Nuller contained three directional couplers with identical interaction lengths.

The writing order of the three individual modifications of each waveguides were not identical between all three directional couplers of the 4T Nuller. The first two directional couplers (DC1 and DC2) were written in the same order, called *inside out*, where the first track written was closest to the centre of the coupling region, then the second and third modification/track of the first waveguide. This was followed by the modification closest to the centre of the second waveguide and so forth. Due to the geometry of the 4T-Nuller, this meant that the central directional couplers (DC3) were fabricated in the opposite order, called *outside in*.

In parallel, a block of 7 × building block reference directional couples was also written with a more extended range of coupling length of 4.0 to 7.0 mm, with an interval of 0.5 mm. The writing order followed here is called *left to right*, where the left track was first inscribed, followed by the middle and right tracks.

For all directional couplers, the right waveguide features a change in propagation constant/effective index to introduce asymmetry inside the coupler for creating achromatic splitting, which is one essential requirement to obtain achromatic 50/50 splitting. To introduce this change, this section of the waveguide was written at a velocity of 55 mm/min, whereas the optimal writing velocity for waveguides was 100 mm/min, as discussed in Chapter 4. Lowering the feedrate to fabricate asymmetrical directional couplers using the multiscan technique in the thermal regime was standardised based on the work of Gretzinger *et al.,* [150]. Additionally, the pitch between asymmetrical directional couplers was maintained at 26 μm, and the radius of curvature of the cosine S-bend was fixed at 50 mm.

After performing FFT spectroscopy, it was observed that the bar and cross-ratios were significantly off from the required 50/50 ratio for the interaction lengths and writing order employed in the directional couplers within the 4T-Nullers, as exemplified in Figure 6.4 for DC1 and DC2.

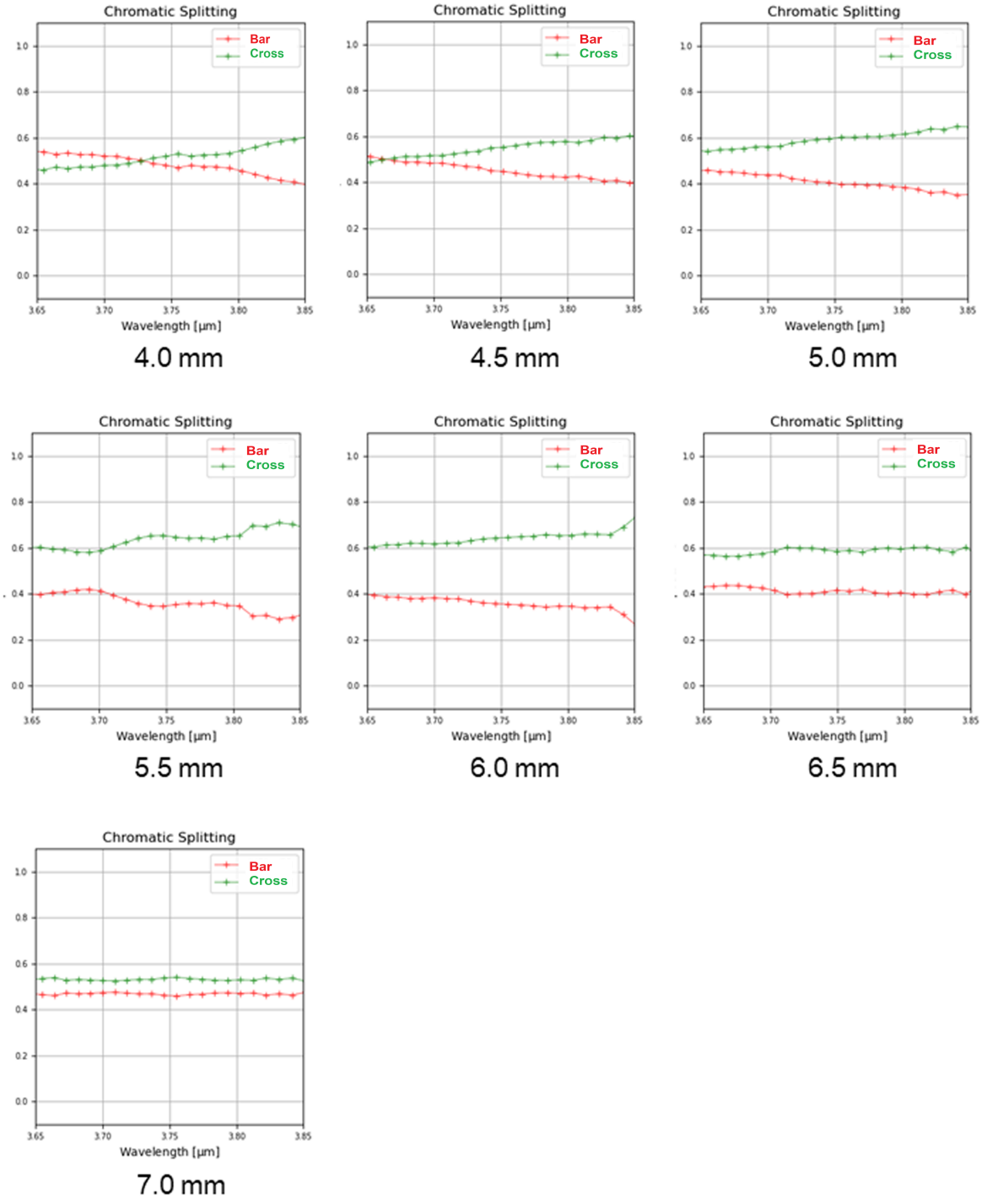

Figure 6.3: These plots depict the chromatic splitting ratios obtained from reference directional couplers with interaction lengths ranging from 4.0 mm to 7.0 mm at intervals of 0.5 mm in Sample II for injection left input. The red and green colours illustrate the bar's chromatic behaviour and cross-coupling ratios across the L' band range.

However, the building blocks 2 × 2 reference directional couplers were inscribed on the same chip with *left to right* writing order served as a guide to determine the appropriate writing order and interaction length needed to create 50/50 achromatic directional couplers.

Injection into one input of the 2 × 2 directional couplers revealed that achieving 50/50 coupling is feasible with either shorter or longer interaction lengths compared to those used as the directional couplers (DC1, DC2, and DC3) in the 4T-Nuller of this GLS glass sample.

The splitting ratio of directional couplers with longer interaction lengths, i.e., 7.0 mm, exhibits less chromatic behaviour compared to those with shorter interaction lengths, as illustrated in Figure 6.3.

Therefore, the longer interaction length has been considered as the ideal length for fabricating directional couplers for the nulling devices, with writing order *left to right* [35].

As part of the ongoing development of the NOTT nulling device, a new photonic chip, identified as SAMPLE III, was fabricated. Similar to the previous chip, SAMPLE III features a 4T-Nuller, but with interaction lengths ranging from 6.0 mm to 8.5 mm at intervals of 0.5 mm.

Additionally, a set of 2T-Nullers was added within the same range of interaction lengths. This time, the *left to right* writing order was chosen based on insights gained from the directional couplers of SAMPLE II. Apart from this change, all other parameters for directional couplers remain consistent with those of the previous chip, except for the output pitches, as illustrated in Figure 4.7. A block of 2 × 2 reference directional is also rewritten in this GLS glass sample as the previous chip within the same parameters for further comparison, which will be discussed in the next section.

Moreover, SAMPLE IV was manufactured for tailoring Y-junctions. A set of directional couplers similar to SAMPLE III's reference directional coupler was also fabricated with the same inscription properties. Table 6.1 summarises all the relevant details and parameter changes for the fabricated directional couplers in different iteration steps.

Table 6.1: Different iteration parameters of examined directional coupler. The following parameters are kept constant for all the iterations: S-bands radius of curvature = 50 mm, the pitch between coupling region = 26 μm

Types	Writing order	Int. length / interval (mm)	Input pitch (μm)	Output pitch (μm)
Sam.II (Ref. DC)	left to right	4.0-7.0 / 0.5	125	125
Sam.II (4TN DC1)	inside out	5.0-6.2 / 0.2	125	125
Sam.II (4TN DC2)	inside out	5.0-6.2 / 0.2	125	125
Sam.II (4TN DC3)	outside in	5.0-6.2 / 0.2	125	125
Sam.III (Ref. DC)	left to right	5.0-8.5 / 0.5	125	125
Sam.III (4TN DC1)	left to right	6.0-8.0 / 0.5	125	240
Sam.III (4TN DC2)	left to right	6.0-8.0 / 0.5	125	240
Sam.III (4TN DC3)	left to right	6.0-8.0 / 0.5	125	200
Sam.III (2TN DC)	left to right	6.0-8.0 / 0.5	125	125
Sam.IV (Ref. DC)	left to right	5.0-8.5 / 0.5	125	125

6.3 Discussion

6.3.1 Writing order

Essential to achieving the best interferometric contrast is a wavelength-independent coupling ratio as close to 50/50 as possible. As discussed in the previous section, there are noticeable differences in the wavelength responses and the trend of coupling ratios between the three directional couplers of the 4T-Nuller and across the reference directional couplers, depending on the modification/track inscription order.

Figure 6.4 demonstrates the spectrally resolved, from FFT spectroscopy, cross-coupling ratio of 3 directional couplers inside each 4T-Nullers for Sample II and III for the wavelength 3.75 μm. These cross-coupling ratios are plotted against the interaction length L. The difference between them lies in the order of the writing, as indicated in Table 6.1. This plot is an example of how the writing order during ultrafast inscriptions impacts splitting ratios.

A detailed Boson band mapping study with GLS glass for various writing orders, affiliated with publication [151], can uncover the behaviour of the writing order on refractive index and its impact on splitting ratios, which is a separate topic and beyond the scope of this work. However, this study has highlighted an intriguing topic for future research.

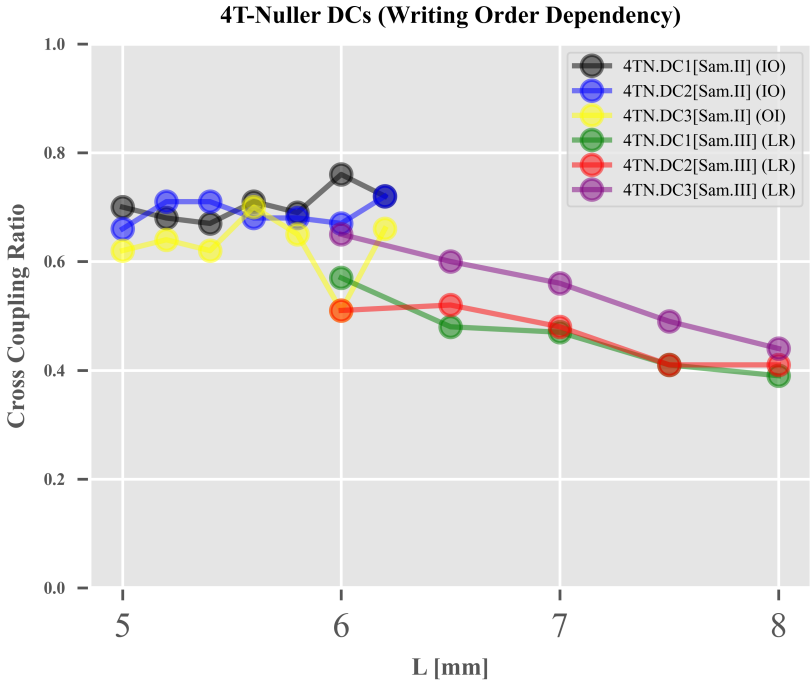

FIGURE 6.4: The trend of cross-coupling ratio for DC1 and DC2 in 4T-Nullers of SAMPLE II and III highlights the dependency on writing order. Label IO denotes *inside out* writing order, OI for *outside in*, while LR denotes *left to right* writing order. The data spectrally resolved for 3.75 μm.

6.3.2 Interaction length and reproducibility

Apart from the writing order, the splitting ratio is determined by the length of the coupling region, the coupling coefficient, and the dephasing or asymmetry introduced by the S-bends leading in and out of the coupling region. This section uses the results from coupled-mode theory to extract and compare coupling coefficients κ and dephasing $\Delta\beta$ across different devices and samples.

Following experimentation with directional couplers in SAMPLE II, all directional couplers (both reference and nullers) were inscribed using the same writing order. Consequently, the subsequent experimental findings permit further discussion.

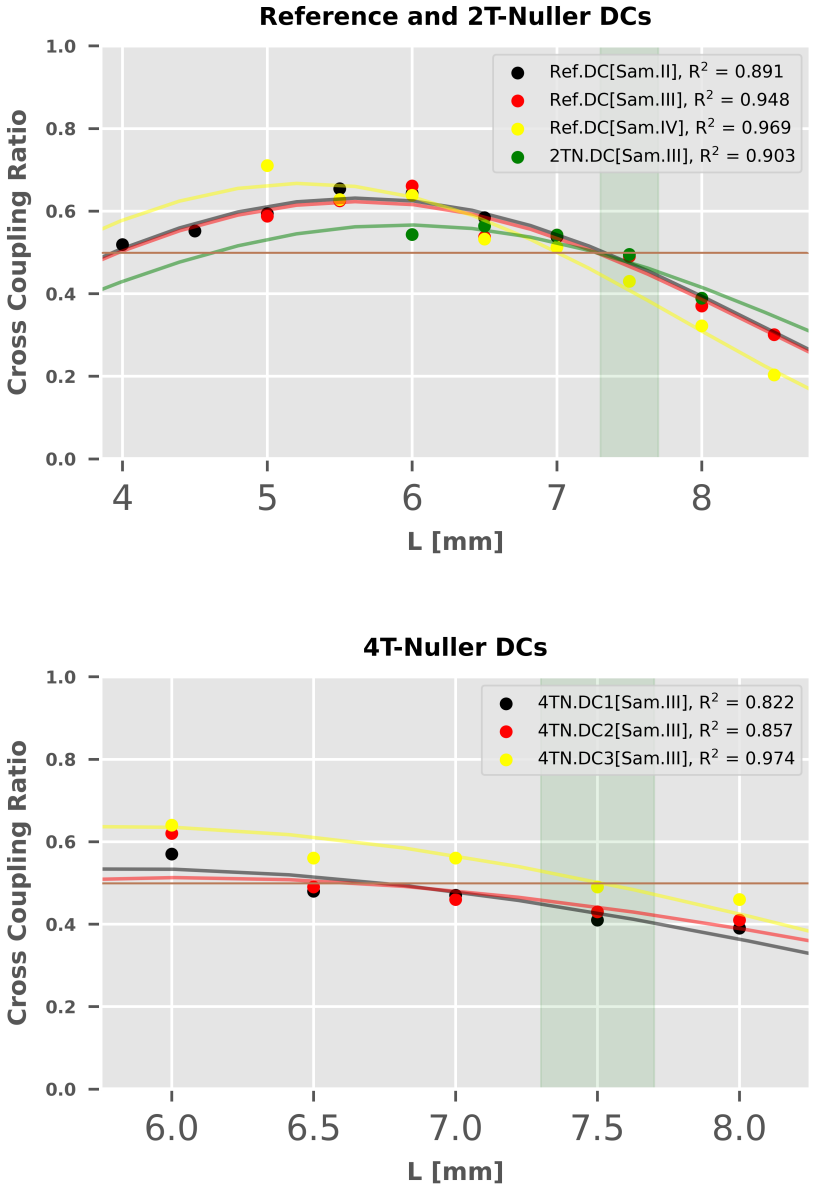

Figure 6.5: Top: Measured cross-coupling ratios of individual reference directional couplers and 2T-Nullers at $\lambda = 3.75$ μm wavelength. $[Sam.X]$ refers to the specific photonic chip sample. Bottom: 4TN-DC1, 4TN-DC2, and 4TN-DC3 are the three cascaded directional couplers of the 4T-Nuller. Within a 4T-Nuller, each directional coupler exhibits the same interaction length. Statistical R^2 values of all the plots quantify the goodness of the curve-fitting (using Equation 6.9). The green section indicates the acceptable device as a function of the interaction length. The brown Horizontal line shows the 50/50 region

Figure 6.5 presents the experimental cross-coupling ratios as data points for single directional couplers and cascaded directional couplers, specifically at a wavelength $\lambda = 3.75$ μm, which is the central wavelength of the L' band. These splitting ratios are plotted against the interaction length L. The differences in design of these couplers are summarised in Table 6.1

It has been found that the 50/50 cross-coupling ratio at $\lambda = 3.75$ μm wavelength for individual directional couplers is typically observed for an interaction length of $\approx$ 7.5 mm. Yet, in the 4T-Nullers, the 50/50 splitting ratios for DC1 and DC2 are for $\approx$ 6.5 mm interaction length, while DC3 requires an interaction length of 7.5 mm.

To extract coupling coefficients κ and dephasing $\Delta\beta$ the cross-coupling ratios were fitted by Equation 6.8, as shown in Figure 6.5. Best fits were found for $\phi = 0$, even though one would expect non-negligible coupling in the S-bends based on results by Gretzinger *et al.,* [150]. In the present case, it is likely due to the absence of experimental data at short interaction lengths L < 4 mm. The solid lines in Figure 6.5 represent the fitted curves, accompanied by their respective statistical coefficient R^2, indicating how well the data fits coupled-mode theory.

Table 6.2 illustrates the $\Delta\beta$ and κ values derived from the curve fitting. κ is influenced by the size of the waveguide and its index contrast, which, in turn, alters the mode-field profile, consequently affecting κ. When these factors change, they impact the mode-field profile within the waveguide. As a result, any alteration in the mode-field profile subsequently influences the value of κ. Besides, $\Delta\beta$ represents the relative change in waveguide properties. For ULI directional couplers, both waveguides are inscribed using the same pulse energy, and there is confidence in the accuracy of the computer-controlled stages, ensuring consistent movement at the correct velocity or feedrate. However, despite these factors being controlled, $\Delta\beta$ may still be influenced by long-range stress [148].

The obtained $\Delta\beta$ values of the reference directional couplers and the 2T-Nuller agree well despite being fabricated across different GLS glass batches (four photonic chips using two batches, LD1765 and LD1999). It highlights good reproducibility. Additionally, the central directional coupler (DC3) within the 4T-Nuller demonstrates

a similar $\Delta\beta$ to these single couplers. A noticeable discrepancy exists in $\Delta\beta$ between DC1 and DC2 compared to other couplers. Conversely, the κ values show relatively inconsistent behaviour across both single and cascaded architectures. Furthermore, it appears that the choice of GLS glass samples or substrates in this study does not exert a significant influence on either $\Delta\beta$ or κ, underscoring the remarkable reproducibility of directional couplers across various GLS glass samples.

Table 6.2: $\Delta\beta$ and κ parameters obtained from the fabricated directional couplers at 3.75 μm wavelength.

Photonic Chip	DC types	$\Delta\beta$ (rad/mm)	κ (rad/mm)
Sam.II (LD1999)	Ref. DC	0.34	0.22
Sam.III (LD1999)	Ref. DC	0.34	0.22
Sam.IV (LD1765)	Ref. DC	0.35	0.24
Sam.III (LD1999)	2TN-DC	0.34	0.20
Sam.III (LD1999)	4TN DC1	0.37	0.20
Sam.III (LD1999)	4TN DC2	0.36	0.19
Sam.III (LD1999)	4TN DC3	0.33	0.22

In comparison, Gretzinger *et al.* [123; 150] investigated $\Delta\beta$ and κ of asymmetrical directional couplers with 26 μm centre-to-centre waveguide separation at 4 μm wavelength. The directional couplers produced in 100 mm/min nominal fabrication feedrate showed higher transmittance, and the second waveguide of the coupling region was written with a lower freedrate, where velocity tapers were also included in the S-bends before and after the coupling region. These directional couplers were also fabricated using ULI in GLS glass based on a sequentially written triplet waveguide structure. In contrast, the velocity of the second waveguide was reduced from 75 to 55 mm/min to introduce asymmetry, which increases $\Delta\beta$ from 0.24 to 0.32 rad/mm, and also κ from 0.26 to 0.34 rad/mm. These results were obtained by adding zero length coupler term in their equation.

Moreover, concerning the directional couplers of 4T-Nuller, the input and output waveguide pitch changes depending on the device (see Table 6.1). The reference directional couplers exhibit 125 μm input and output pitch. In comparison, the central directional coupler of the 4T-Nuller (DC3) has an input pitch of 125 μm and output

pitch of 200 μm, and the pitch between the central and side combiners (I1 and I2 of DC1, and I4 and I3 of DC2) is 240 μm, as illustrated in Figure 4.7. Considering this output arrangement in the design, the length of S-bends used as inputs for DC1 and DC2 is 3.49 mm, identical to the reference directional couplers, while the length of S-bends leading signals from DC1 and DC2 to DC3 as inputs is 4.94 mm, both for a cosine S-bend with 50 mm minimum radius of curvature.

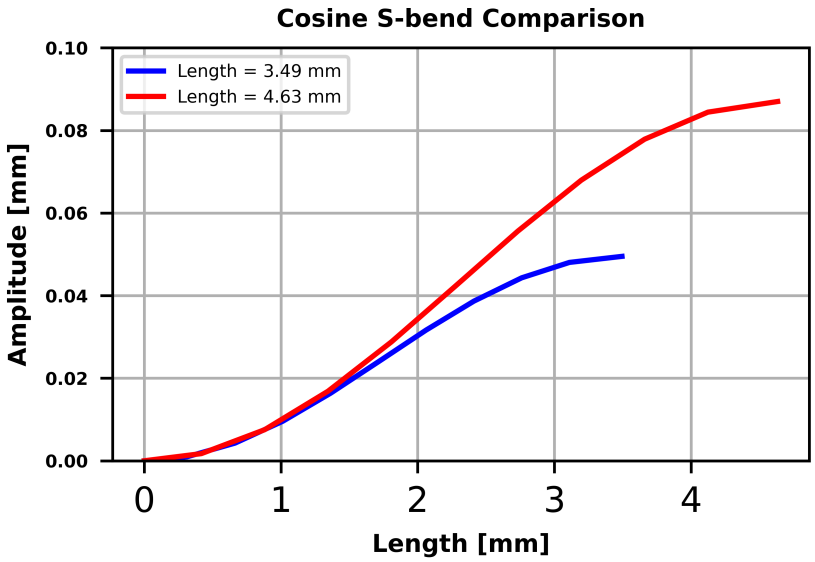

FIGURE 6.6: The length of the two cosine S-bends is calculated from the minimum radius of curvature (50 mm) and the amplitudes of the two S-bends. Amplitude is calculated based on the input/output pitch and the pitch in the coupling region, as given in Table 6.1

As shown in Figure 6.6, shorter cosine S-bends with equal minimum radius of curvature result in the waveguides being marginally closer for a longer distance. This facilitates more cross-coupling, hence requiring a shorter coupling length.

Therefore, DC1 and DC2, with their longer S-bends, should require longer interaction lengths to achieve 50/50 cross-coupling compared to the reference directional couplers or DC3. Yet, this contradicts the experimental observation, where DC1 and DC2 require shorter interaction lengths compared to all other directional couplers.

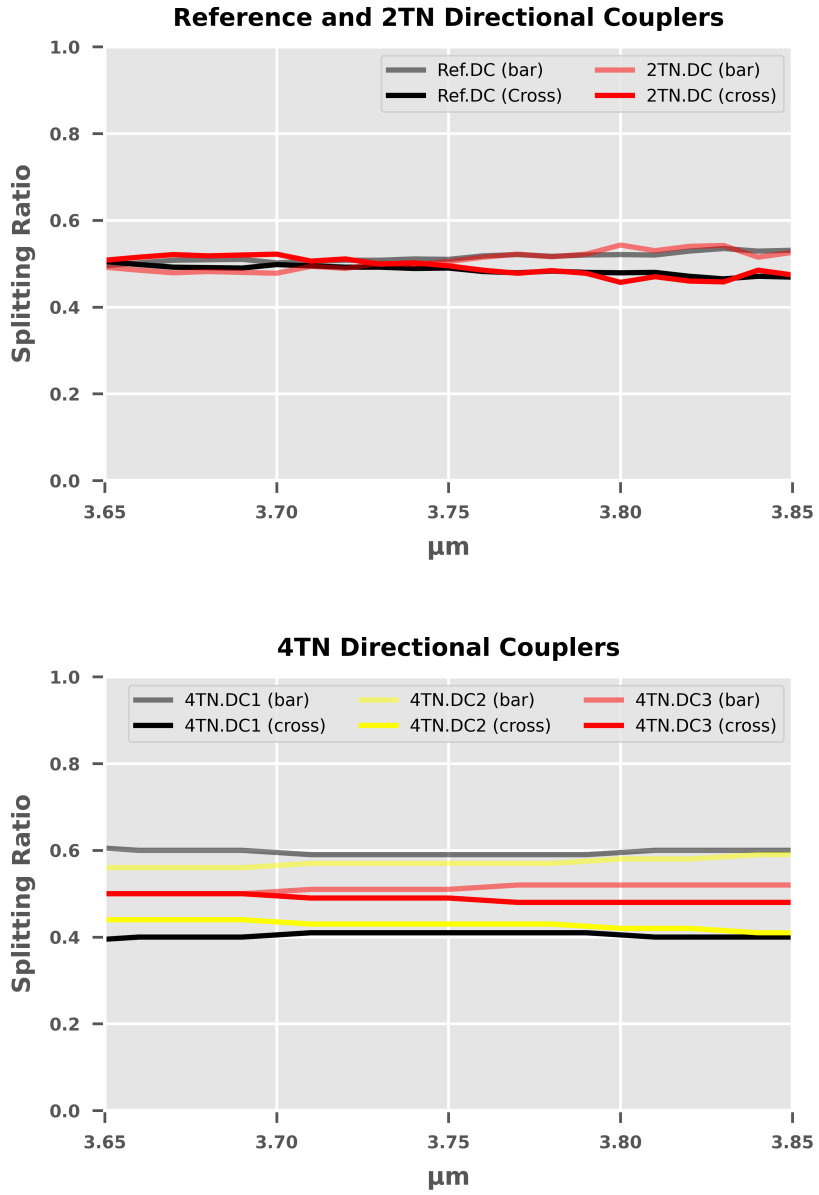

Figure 6.7: The upper image illustrates the achromatic splitting characteristics of 50/50 directional couplers measured for a reference and a 2T-Nuller with an interaction length of 7.5 mm, across the L' band of $\lambda = 3.65$ *to* 3.85 μm. The lower image portrays the achromatic splitting ratios of the 4T-Nuller. While the central combiner (DC3) exhibits a 50/50 splitting across the L' band, DC1 and DC2 deviate from the 50/50 ratio. All three directional couplers of the 4T-Nuller share the same interaction length of 7.5 mm.

Thus, the S-bends can likely be ruled out to cause the difference in the splitting ratio. There is also a possibility of being affected by the influence of long-range stresses induced by the ULI process due to sequential fabrication. Despite the different interaction lengths, there is no significant difference in chromaticity between DC1/2 and DC3 at their respective 50/50 splitting ratio point.

The reference directional couplers and 2T-Nuller DCs, both owning an interaction length of 7.5 mm, exhibit a very balanced bar and cross-splitting ratio of 52/48 with $\pm$ 0.03/0.03 standard deviation across λ = 3.65 to 3.85 μm, as shown in Figure 6.7.

Within the SAMPLE III, a 4T-Nuller, composed of three interconnected directional couplers (DC1, DC2, and DC3) of the interaction length of 7.5 mm, demonstrates imbalanced DC1 and DC2 even though their cross-coupling behaviours are comparable across the L' band to each other. However, the central directional coupler or DC3 attains a balanced 50/50 configuration across the broadband, as vividly illustrated in Figure 6.7. Due to the fact that the central combiner produces the self-calibrated null, which requires achromatic 50/50 splitting ratios, this particular 4T-Nuller is considered as the key testing 4T-Nuller for assessing nulling performance, facilitating a comprehensive understanding of 4-telescopic nulling behaviour, examination methods, and the ensuing results, all of which are discussed in detail in Chapter 8.

7

Nulling with 2-telescope beam combiners

The 2T-Nuller serves as a stepping stone to the 4T beam combiner required for the NOTT instrument. The 2T-Nuller is a basic beam combiner utilising a single 2×2 directional coupler and two Y-junctions for photometry. While a single 2×2 directional coupler can perform nulling interferometry, it does not provide simultaneous photometric information. In comparison, this 2T-Nulller shares a design similar to the GLINT nulling beam combiner[90], which advanced by introducing photometric channels before the 2×2 directional coupler, providing the ability for simultaneous photometric measurements along with the actual nulled and anti-null channel. This allows a more accurate estimation of the null depth compared to non-simultaneous photometric measurements using chopping, for instance. This design is inherited from J.P. Berger *et al.,* [186].

This chapter presents the experimental interferometric characterisation of the 2T-Nullers equipped with a 50/50 achromatic directional coupler. This serves as a benchmark, contributing to a deeper understanding of the nulling capabilities of a more complex 4-telescope beam combiner using the double-Bracewell architecture.

7.1 2-telescope nulling beam combination scheme

In the context of astronomical nulling interferometry, the preliminary objective is to achieve destructive interference of an astronomical source by precisely adjusting the phases and amplitudes between two coherent light waves coming from two telescopes, denoted T1 and T2, separated by a certain baseline, as shown in Figure 7.1

Two monochromatic light beams of wavelength λ, represented by electric fields $\vec{E_1}$ and $\vec{E_2}$, are captured by T1 and T2, respectively. The phases of the two beams are ϕ_1 and ϕ_2, and the amplitudes are E_{01} and E_{02}. Accordingly, the electric fields of the two beams can be expressed as $\vec{E_1} = E_{01}e^{i\phi_1}$ and $\vec{E_2} = E_{02}e^{i\phi_2}$.

However, from the point of detection, the detected signals are represented by their intensities, where the generalised intensity, I, is the time-averaged component and is proportional to the square of the amplitude E_0 of its electric field $\vec{E}$, $I \propto \langle E_0 \rangle^2$. This relationship can also be expressed using the complex conjugate electric fields $\vec{E}^*$ as $I_T = |E_0|^2 = |\vec{E}.\vec{E}^*|$ [160].

Then, for two detected signals, after applying the principle of superposition, the electric field in the beam combiner can be expressed as $\vec{E_T} = \vec{E_1} + \vec{E_2}$. The intensity I_T of the resulting interferometric signal can be derived as Equation (7.1) via the individual beam intensities, I_a and I_b, where $\phi = \phi_a - \phi_b$ is the phase difference between two detected signals. These relations lead to Equation (7.1)

$$\begin{aligned} I_T &= |\vec{E_T}.\vec{E_T}^*| \\ &= (\vec{E_1} + \vec{E_2}).(\vec{E_1} + \vec{E_2})^* \\ &= E_{01}^2 + E_{02}^2 + E_{01}E_{02}.(e^{i\phi} + e^{-i\phi}) \\ &= I_a + I_b + 2\sqrt{I_a.I_b}\cos(\phi) \end{aligned} \tag{7.1}$$

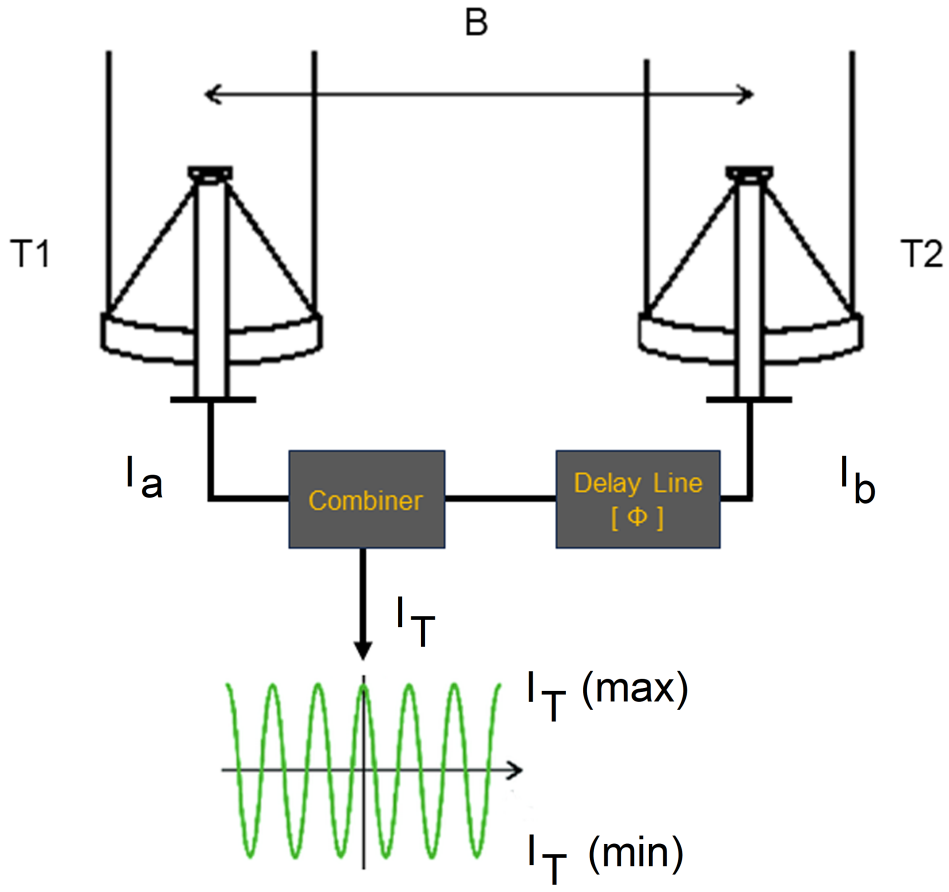

FIGURE 7.1: The schematic diagram represents a simple 2-telescope interferometer for a monochromatic optical signal. Telescopes T1 and T2, separated by a baseline B, receive respective intensities I_a and I_b from an astronomical source. A delay line is introduced with one of the signals to equalize optical path length before reaching the combiner section, called Nuller in nulling interferometry, where both signals are combined according to the principle of wave superposition to generate the interferometric signal I_T. Continuous scanning of the delay line introduces constructive and destructive interferometric fringes denoted as $I_T(max)$ and $I_T(min)$.

Equation (7.1) suggests that the maximum and minimum intensities of interference, denoted as $I_T(max)$ and $I_T(min)$, depend on the phase difference ϕ between the two beams I_a and I_b, and thus can be expressed as Equation (7.2).

$$\begin{aligned} I_T(max) &= I_a + I_b + 2\sqrt{I_a.I_b} = |E_{01} + E_{02}|^2 \\ I_T(min) &= I_a + I_b - 2\sqrt{I_a.I_b} = |E_{01} - E_{02}|^2 \end{aligned} \tag{7.2}$$

In astronomical interferometry, different values of ϕ are introduced by scanning a high-precision delay line, which is similar to any classical Michelson interferometer, and as a result, different intensities are obtained as fringes while scanning. Figure 7.1 illustrates this process. $I_T(max)$ and $I_T(min)$ lead to quantitative measures of the interferogram by calculating the raw or instrumental contrast and extinction ratio or null depth of the interferogram using Equation (7.3). Both, contrast and null depth, are key parameters for characterising the performance of an interferometer, and the null depth is the primary concern for nulling interferometry [187; 88].

$$\begin{aligned} C &= \frac{I_T(max) - I_T(min)}{I_T(max) + I_T(min)} \\ N &= \frac{I_T(min)}{I_T(max)} \end{aligned} \tag{7.3}$$

The instrumental contrast is linked to the visibility and phase resolution, whereas the null depth aims to improve the sensitivity of the instruments for fainter off-axis emissions by attenuating starlight. Their relation is described according to Equation (7.4) [188].

$$\begin{aligned} C &= \frac{1 - N}{1 + N} \\ N &= \frac{1 - C}{1 + C} \end{aligned} \tag{7.4}$$

Thus far, the discussion has revolved around an ideal and error-free two-beam interference. However, in any practical interferometer, various imperfections can induce an increased level of light leakage. A time series of null-depth measured values N_m can be described by Equation (7.5), wherein N_a represents the true astrophysical null depth containing non-stellar off-axis emission, $N_s(B)$ is due to stellar leakage, and N_i denotes the instrumental null depth contribution.

$$N_m = N_a + N_s(B) + N_i \tag{7.5}$$

The term $N_s(B)$ can be expressed as $N_s(B) = \frac{\pi^2}{16} \cdot (\frac{B\delta\theta_s}{\lambda})^2$, where B is the baseline of the interferometer and θ_s is the angle of the start signal that yields over the null, and $\delta\theta_s$ is stellar diameter measurement accuracy. For Palomar Fiber Nuller (PFN) $\theta_s = 166\sqrt{N_s}$ in mas at wavelength 2.15 μm. Accurate star diameter measurements can help to omit this effect [88].

$$N_i = \frac{1}{4}(\overline{\Phi_a^2} + \overline{\Phi_t^2} + \overline{\Phi_d^2} + \overline{\Phi_p^2} + \overline{\alpha^2} + \overline{\delta^2}) \tag{7.6}$$

Equation (7.6) describes the instrumental null components, in sequence, the spatial variance of the wavefront phase difference between the beam apertures, the temporal variance of the average phase difference within one integration time period, the spectral variance of the dispersion across the passband, the variance of the retardance between the two polarisation states, the variance of the residual polarisation rotation angle between the beams, and the variance of the amplitude imbalance. Each of these variances can be calculated over a distinct variable. However, the timescales involved between the different contributing disturbances to the instrumental null depth may differ significantly. Some terms remain relatively stable, while others exhibit rapid variations. Therefore, the astrophysical null depth is not determined directly by the measured or average measured null $\overline{N_m}$. Instead, Equation (7.7) is employed, utilising a statistical method developed by E. Serabyn *et al.*[188; 88] with a straightforward approach by subtracting N_i and average instrumental null contribution $\overline{N_i}$ from $\overline{N_m}$.

$$N_a = \overline{N_m} - N_i - \overline{N_i} \tag{7.7}$$

7.1.1 Photometrically corrected interferogram

During the interferometric measurement, the injected flux into the beam combiner can change, leading to imbalance and a reduction in interferometric contrast. For long recordings in a laboratory, this can be caused by scanning the delay-line or temperature

changes resulting in misalignment. On a telescope, the main source is the Earth's atmosphere. Therefore, the concept of *photometrically corrected interferogram* is widely used to adjust or correct by taking into account the variations in the photometric brightness at the inputs during the scanning, which was first used on-sky for an H-band integrated optics beam combiner at the VLTI [189]. This correction is applied to mitigate the impact of unequal brightness or intensity fluctuations. The goal is to improve the accuracy of the measurements.

A photometrically corrected interferogram for a 2-telescope interferometer can be established in a simple form, if I_a and I_b, referred to as photometric signals, are individually available or measurable for a specific interference signal I_T. Then the intensity properties of Equation (7.1) can be written as Equation (7.8), where I_{pc} is denoted as the photometrically corrected interferogram — a normalised representation of raw interferogram I_T, with a property of having maximum and minimum range in between -1 to $+1$. Equation (7.3) allows estimating the photometrically corrected contrast and null as Equation (7.9).

$$I_{pc} = \frac{I_T - I_a - I_b}{2\sqrt{I_a.I_b}} \tag{7.8}$$

$$\begin{aligned} C_{pc} &= \frac{I_{pc}(max) - I_{pc}(min)}{I_{pc}(max) + I_{pc}(min)} \\ N_{pc} &= \frac{I_{pc}(min)}{I_{pc}(max)} \end{aligned} \tag{7.9}$$

The advantage of the photometric correction lies in the fact that the raw contrast or null, Equation (7.3), is equal to the photometrically corrected contrast or null, Equation (7.9), for the condition $I_a = I_b$. Otherwise, if the photometries are unbalanced, it affects the level of raw contrast or null compared to the actual values, which is associated with the fringe decrease due to unbalanced flux.

7.2 Experimental results with the 2T-Nuller

To perform nulling interferometry with the 2-telescope nulling beam combiner, a 2T-Nuller with a directional coupler of 7.5 mm interaction length is used from Sample III. The directional couplers feature a splitting ratio $\approx$ 50/50 and are achromatic, as illustrated in Figure 6.7 in Chapter 6. The Y-junctions for photometry are also achromatic, as shown in Figure 5.4 of Chapter 5, with an average splitting ratio between photometry and interferometry of $\approx$ 40/60. An achromatic $\approx$ 50/50 reference directional coupler of interaction length 7.5 mm from the same chip was used as a baseline to assess if the higher complexity of the 2T-Nuller versus a simple directional coupler affects the interferometric performance.

The experimental setup involves injecting two broadband L' beams from a supercontinuum source (SCS) into the 2T-Nuller (first Michelson interferometer of characterisation setup II, as depicted in Figure 3.3).

A delay line actuated by a servo motor was used to adjust the beam injected into input T2 for setting the zero-optical path difference (0-OPD) region to record the interference. Figure 7.2 shows a camera image of the four outputs of the 2T-Nuller with the interferometric outputs I_1 and I_2 and photometric outputs P_1 and P_2. Moving the delay line facilitates the detection of interferometric fringes within the coherent envelope of the broadband source spanning from 3.65 to 3.85 μm wavelength.

The sum of flux from the interferometric outputs, I_1 and I_2, for injecting either into input T1 or T2 is unequal. The directional coupler inside the 2T-Nuller is 50/50 and achromatic, irrespective of the injection port. If the total output flux is normalised according to $(I_1+I_2) = 1.0$ for injection into input T2, then it was found that $(I_1+I_2) = 0.72$ for injection into T1.

This indicates it is because the losses between the optical path for input T1 and T2 injections are not identical. Given that the Y-junctions for photometry exhibit a similar splitting ratio, the excess loss in the T1 arm is from a defect in the S-bend for stray-light suppression. Indeed, defects were found under the optical microscope. To achieve the best possible interferometric contrast, equal flux is importance. Therefore,

careful manual detuning was performed by titling one of the injection mirrors to achieve balanced flux at the chip's output I_2. This compensates for the chip's imperfections and a flux imbalance between the injection beams inherent to the test bench. To evaluate the null depth, the delay line is scanned, and the position where the I_2 intensity exhibits its maximum destructive interference (or minimum intensity) is considered the position of zero optical path difference (0-OPD).

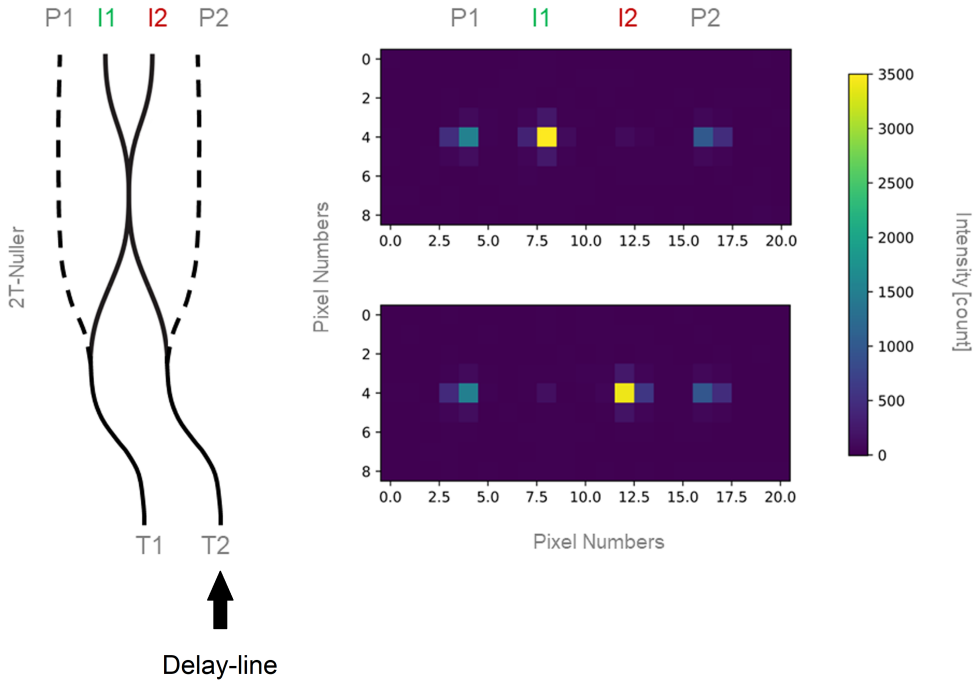

FIGURE 7.2: The left-hand side depicts the waveguide layout of the integrated optics 2T-Nuller, combining the signals from T1 and T2 across an achromatic 50/50 directional coupler. This produces π-phase shifted interferometric outputs I_1 and I_2. As the phase or optical path difference between the inputs is scanned, alternating one output exhibits constructive interference while the other exhibits destructive interference. Outputs P_1 and P_2 correspond to the photometry channels splitting the input using a Y-junction. The right-hand side image illustrates the detected broadband outputs (P_1, I_1, I_2, and P_2) using a camera. A delay line is placed before T2. The top image shows the case when I_1 is constructive, and I_2 exhibits destructive interference, while the bottom image depicts the reversed situation. Each pixel on the detector is 30×30 μm, similar to the waveguide MFD mentioned in Chapter 4. Nearby pixels are illuminated by the beam combiner's output, because its waveguide positions do not exactly match an interger multiple of the detector's pixel pitch.

7.2.1 Process of recording interferograms

The process for performing nulling interferometry here uses the *Dynamic Method*. This involves moving the delay line within the coherent length of the light source. The delay line is scanned at its minimum speed across several fringes (typically 5 to 10) around the 0-OPD location.

These fringes are captured at a framerate between 125 and 250 Hz. This ensures that the zero optical path difference (OPD) region fell within these fringes. The camera software generates *.irb* files containing the recorded data. The recorded data allow for the extraction of the flux from each photometry and interferometry output as a function of the recorded frames. A random region of nine pixels outside these outputs is used to determine the background. The plot in Figure 7.3 illustrates the outputs and fringes extracted in this manner without any further correction.

This simultaneous photometry information from P_1 and P_2 alongside interferometric outputs I_1 and I_2 contains the intensity information of inputs T1 and T2. The mathematical relation between simultaneous photometry and interferometry can be expressed as $I_1 \propto P_1$ and $I_2 \propto P_2$.

After performing this simultaneous recording, a non-simultaneous recording was also taken into place for the photometry information. Non-simultaneous photometry refers to the interferometric output signal, while another beam is not launched on the second input. Such non-simultaneous recording is typically used to perform interferometry with 2×2 directional couplers [159].

During this process, data was recorded after blocking one injection, followed by recording data after blocking the other injection. The intensity of each interferometric output for individual beams was considered as the photometry data for that specific output. For example, to have photometry of interferometric output I_2 in a non-simultaneous technique, first T2 was blocked and recorded data for T1, which is one photometry (similar to I_a of Equation (7.1)), then secondly T1 was blocked to record I_2's intensity for T2 (which is I_b of Equation (7.1)).

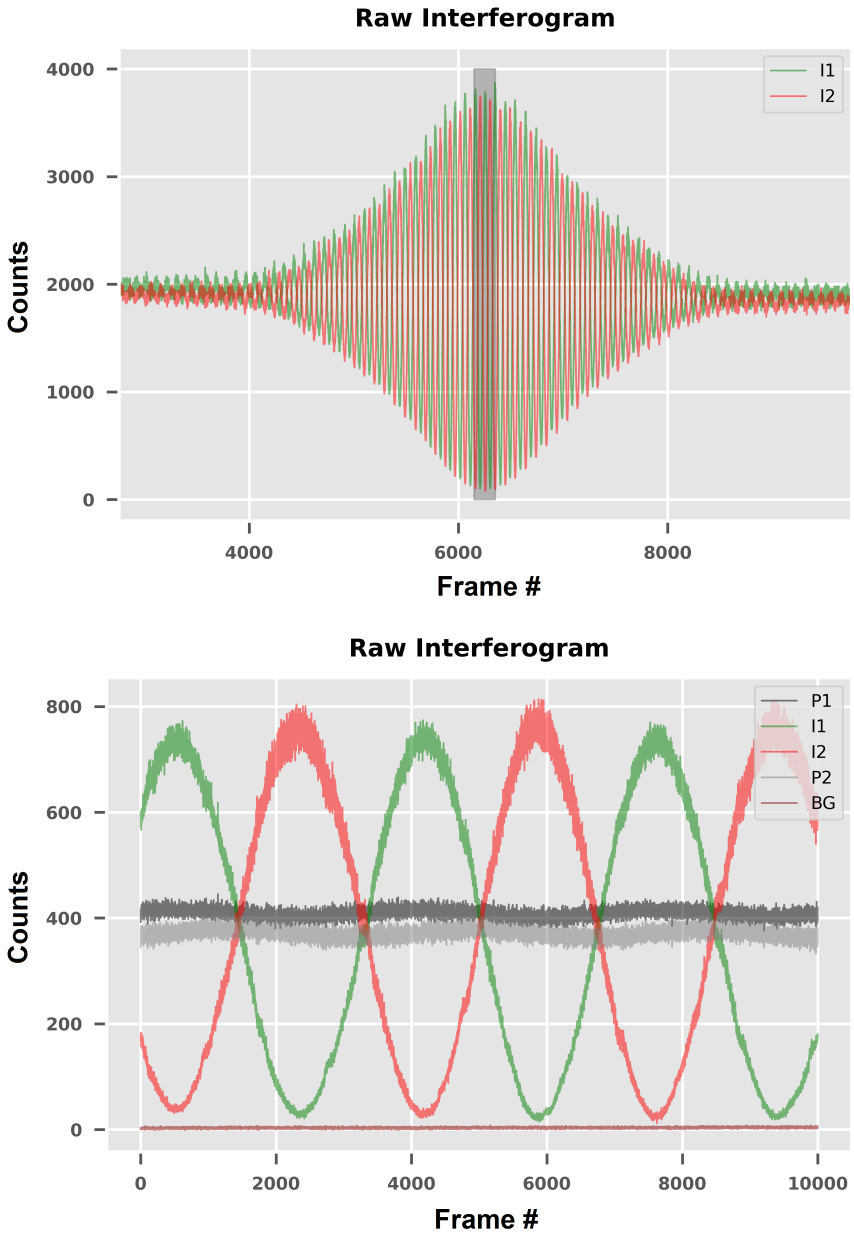

FIGURE 7.3: The figure shows the raw broadband interferogram obtained while scanning the delay line as a function of recorded frames. The plot at the top displays the entire interferogram within its coherent length, while the region marked as grey corresponds to where the interferometric outputs I_1 and I_2 reach their maximum and minimum values due to interference. The grey highlighted region is scanned at the slowest possible speed to produce the bottom plot. In addition to the interferometric signals, also simultaneous photometry signals P_1 and P_2 are shown, revealing a periodic variation over the scanning length due to coherent background or crosstalk. This plot also compares the background signal BG obtained by averaging intensity values from nine randomly selected nearby pixels around the output facets. It is apparent that the intensity of I_1 and I_2 during their respective destructive fringes are above the average background level.

7.2.2 Extracting contrast and null depth

Four different analysis techniques were used to determine each measurement's contrast and null depth as a part of the *Dynamic Method*. They can be classified as follows: (i) raw contrast and null (C_r and N_r), where the minimum and maximum values of the recorded interferogram are identified and by using Equation (7.3), contrast and null were calculated. However, this approach can be severely affected by high-frequency noise, as seen in Figure 7.3 (bottom), showing that the signals I_1 and I_2 both contain high-frequency noise. This noise was evident in the recorded signals and originated from detector read-out noise and the intensity/spectrum instabilities of the feeding supercontinuum source. (ii) raw-fitted contrast and null (C_{rf} and N_{rf}). The main purpose of this approach is to minimise the impact of high-frequency noise. To do so, a monochromatic cosine function is fitted to the interferogram data centred around the 0-OPD region with the help of a Python-based *curve fitting* script. Careful attention during fitting is paid to ensure a statistical confidence level $R^2 \approx 0.99$. After fitting, maximum and minimum values for the interferogram are identified from the fitted cosine to calculate the contrast and null using Equation (7.3). (iii) contrast and null with non-simultaneous photometrically corrected interferogram ($C_{pc[ns]}$ and $N_{pc[ns]}$), and (iv) contrast and null ($C_{pc[s]}$ and $N_{pc[s]}$) with simultaneous photometrically corrected interferogram.

The third and fourth approaches were used to calculate the contrast and null using a cosine curve fitting to a photometrically corrected interferogram, similar to the second approach. However, for non-simultaneous photometrically corrected interferograms, non-simultaneous photometry data was obtained from the interferometric outputs by sequentially blocking one of the inputs before or after recording the fringes, as described in the previous section. In addition, for the case of a simultaneous photometrically corrected interferogram, the simultaneously recorded photometry data was used. With Equation (7.9), the contrast and the null depth can be calculated for either of the two approaches. Figure 7.4 depicts the photometrically corrected interferograms for non-simultaneous and simultaneous approaches.

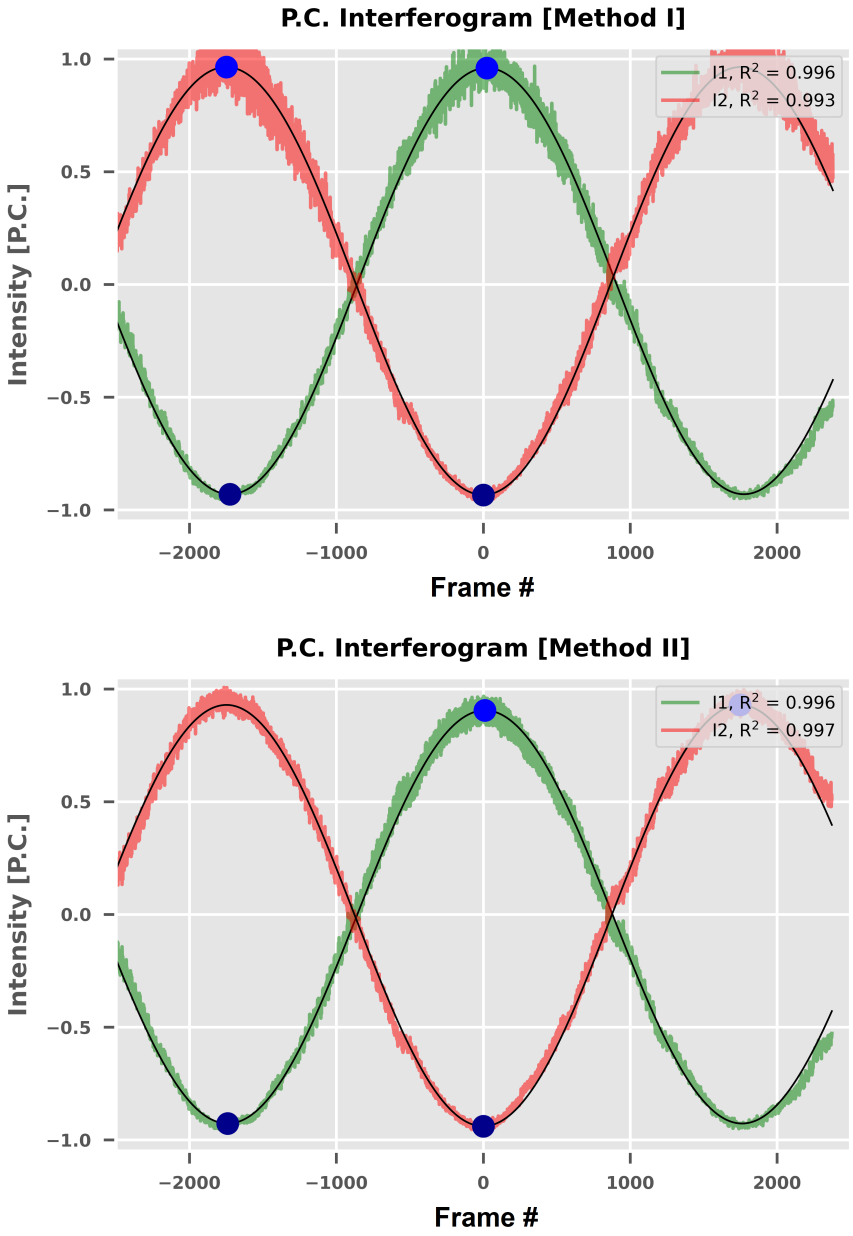

FIGURE 7.4: Two approaches are employed to derive the photometrically corrected interferogram. The upper image illustrates the non-simultaneously photometrically corrected interferogram of outputs I_1 and I_2. The bottom plot demonstrates a photometrically corrected interferogram using the simultaneous photometric outputs P_1 and $P2$. Each fringe pattern is fitted with a cosine curve for both plots to rectify high-frequency noise. The R^2 values indicate the accuracy of the fitting. Blue and dark blue dots denote the maximum and minimum values of each fringe, respectively.

7.2.3 Discussion

The nulling interferometry measurements obtained from the 2T-Nuller reveal several key findings, discussed below. Firstly, Figure 7.3 illustrates that the photometry outputs (P_1 and P_2) of the 2T-Nuller exhibit periodicity/fringes. Such fringes are possible if any cross-talk couples into photometric outputs. However, it has been confirmed that there is no static cross-talk from the 2T-Nuller or 4T-Nuller in the L' band, as observed in Figure 4.6 and 4.7 of Chapter 4. These images were obtained using the mid-infrared camera when injecting into the individual inputs. Camera frames were recorded for a period of 8 seconds and then summed up. They reveal that the photometry output from non-illuminated inputs shows no discernible signal that is distinct from the surrounding background.

Thirdly, the interferometric contrast of the 2T-Nuller is 0.96 ± 0.013 for the four different approaches, as indicated in Figure 7.5. The supercontinuum source (SCS) was used for these measurements. However, the source suffers from intensity and spectral fluctuations inherent to the nonlinear optical processes that cause the spectral broadening. In contrast, the thermal blackbody source (BBS) is more stable and exhibits a broader bandwidth, as illustrated in Figure 3.4. However, the BBS is dim compared to the SCS [190] and thus could not be used with 2T-Nuller due to its lower throughput, as discussed in Chapter 4, and because the light is spread across 4 waveguides at the output rather than just two for an individual reference directional coupler. To compare the 2T-Nullers to the reference directional couplers contrast and null depth were measured using BBS and SCS. Since the 2×2 directional coupler does not have photometry channels, a simultaneous photometrically corrected interferogram can not be measured.

Interferometric measurements using a thermal BBS resulted in a raw contrast C_r level of 0.97 ± 0.009. The C_{rf} and $C_{pc[ns]}$ contrasts are both within 0.94 ± 0.004. When using the SCS, similar to the 2T-Nuller, C_r and C_{rf} are 0.96 ± 0.010, and the photometrically corrected non-simulations interferogram exhibits a contrast $C_{pc[ns]}$ of 0.93 ± 0.015. The improved stability of the BBS provides a slightly higher contrast. When comparing the reference directional couplers to the 2T-Nuller, the contrast levels

for the SCS are within the margin of error. Therefore, the added complexity of the 2T-Nuller has not negative influence on the nulling capabilities of the directional couplers. Placing a linear polariser into the injection beam has shown that the polarisation has no difference within the margins of error on the contrast level [35].

The null-depths for the 2T-Nuller, calculated as the reciprocal of contrast, are $\approx 0.02 \pm 0.007$ for the raw null N_r, raw-fitted null N_{rf}, non-simultaneous and simultaneous photometrically corrected nulls, $N_{pc[ns]}$ and $N_{pc[s]}$, as seen in Figure 7.5. Similar trends are observed for the reference directional coupler against SCS, showing a null depth of 0.018 ± 0.005 as raw and 0.03 ± 0.008 for raw-fitted and non-simultaneous photometrically corrected null. Using the same reference directional coupler, blackbody source experiments yielded a raw null of 0.014 ± 0.005, both N_{rf} and $N_{pc[ns]}$ provided a value of 0.02 ± 0.002.

The contrast and null acquired with the reference directional coupler are summarised in Table 7.1.

TABLE 7.1: Contrast and Null of reference directional coupler with BBS and SCS and polariser

Source	Polaraiser	C_r	C_{rf}	$C_{pc[ns]}$
BBS	No	0.97±0.009	0.94±0.004	0.94±0.004
SCS	No	0.96±0.010	0.96±0.010	0.93±0.015
SCS	Yes	0.96±0.021	-	-
		N_r	N_{rf}	$N_{pc[ns]}$
BBS	No	0.014±0.005	0.014±0.005	0.02±0.002
SCS	No	0.018±0.005	0.03±0.008	0.03±0.008
SCS	Yes	0.019±0.008	-	-

In summary, the contrast and nulls of the 2T-Nuller are comparable, regardless of the four approaches used to obtain them. Moreover, the contrast and null characteristics of the reference directional coupler closely resemble those of the 2T-Nuller when utilising the supercontinuum source.

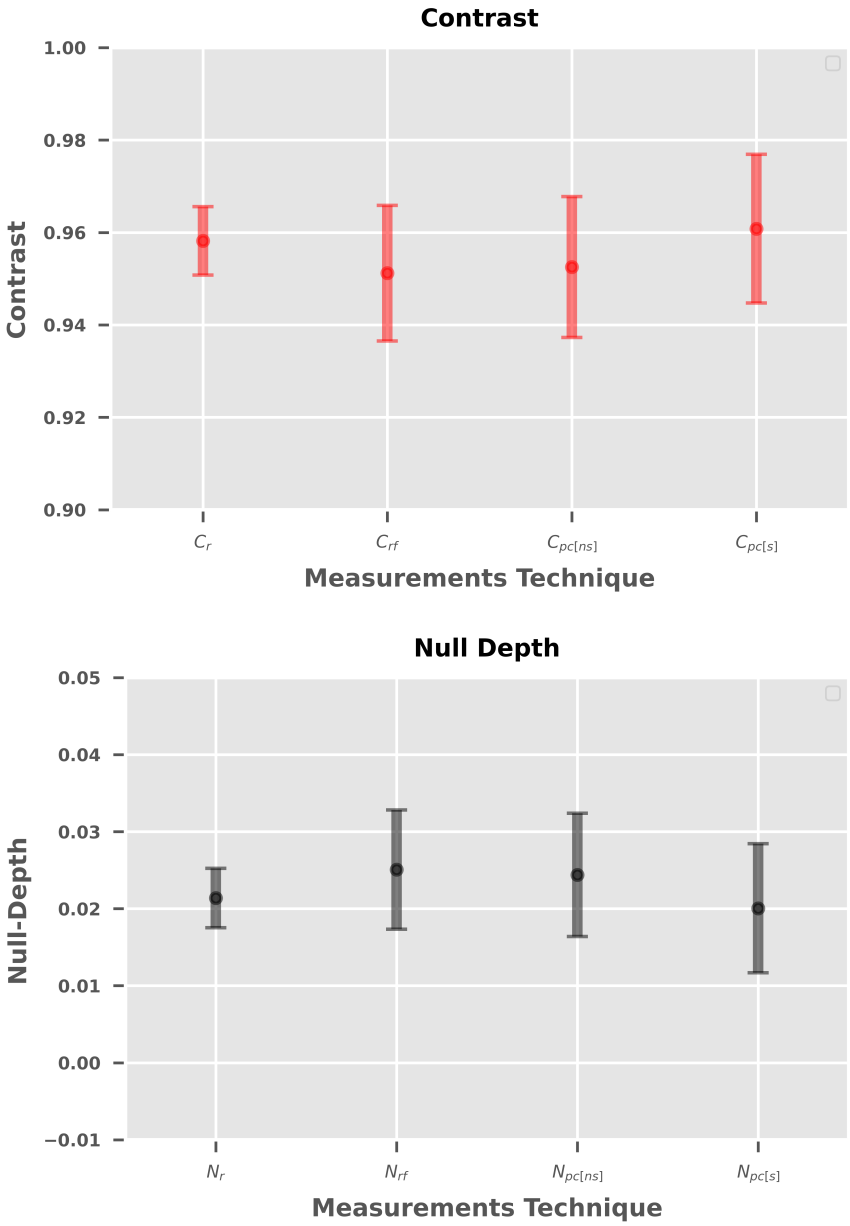

Figure 7.5: Comparison of the 4 different analysis methods to retrieve contrasts and null depths for output I_2 of a 2T-Nuller. In order, from left to right, the graphs show the raw contrast/null depth calculated from interferogram measurements where high-frequency noise is not considered. Next, the raw-fitted values, that are obtained by fitting a cosine curve to the raw data are plotted. This is followed by the contrast/null depths for the non-simultaneous photometrically corrected interferogram and simultaneous photometrically corrected interferogram, respectively. The scatter plot values are the mean of at least 3 experimental measurements, and the error bars indicate their standard deviations. The distribution suggests that all approaches are comparable within their respective error bars.

The comparison between supercontinuum source, supercontinuum source with polariser, and blackbody source with the reference directional couplers suggests that these factors have negligible impact on the contrast and null within the limitations of the test bench. This means the source properties or polarisation also should not gigantic impact the performance of the 2T-Nuller or 4T-Nuller. In summary, null depths in the range of 10^{-2} across a bandwidth of 3.65 - 3.85 μm have been achieved without considering any statistical or numerical mechanism for improving null depth, such as Numerical Self-Calibration (NSC). However, a comparable 2T-Nuller in design implemented on-sky, such as GLINT operating at a wavelength of 1.55 μm, exhibits reaching 10^{-3} within a monochromatic wavelength of $\Delta\lambda/\lambda = 0.05$ μm [91], and Palomar Fiber Nuller (PFN) in K-band demonstrates extinction of 10^{-4} using NSC.

8

Nulling with the 4-telescope beam combiner

The ASGARD/NOTT 4-telescope beam combiner, also referred to as the 4T-Nuller, is based on a *double-Bracewell* architecture, comprising three cascaded 2×2 directional couplers featuring 50/50 achromatic splitting ratios. In the first stage, the initial pair of directional couplers individually generate nulled signals.

Subsequently, in the second stage, these nulled signals are combined by the central directional coupler, producing two nulled outputs with mirrored transmission maps. The difference between these two nulls creates a self-calibrated astrophysical null [157]. In terms of design and laboratory performance, this 4T-Nuller is more complex compared to the 2T-Nuller, which requires a different approach to examine the nulling performance.

This chapter presents a comprehensive mid-infrared broadband characterisation of the 4T-Nuller in its complete four-telescope nulling configuration. The 4T-Nuller

was simultaneously illuminated by four beams from the supercontinuum source, and the extinction ratios of the two nulled outputs were measured before self-calibration. These measurements were conducted under broadband illumination and without any polarisation control.

The examined 4T-Nuller is considered for integration into ASGARD/NOTT in the instrument's first deployment phase.

8.1 4-telescope nulling beam combination

In the case of a 2-telescope interferometer, a delay line in front of one of the two inputs can be used as a phase shifter before injecting both coherent signals into the beam combiner. This is a classical single-Bracewell arrangement, as shown in Figure 7.1.

To convert to a 4-telescope interferometer, one can follow the scheme of Angel & Woolf [79] by adding a second layer of beam combination elements. This is typically classified as a double-Bracewell beam combiner.

The characterisation of a double-Bracewell beam combiner requires at least 3 independent delay lines to introduce specific phase shifts before being injected into the 4-telescope beam combiner, as illustrated in Figure 8.2.

The signals received by telescopes T1, T2, T3 and T4 are denoted with respect to electric fields $\vec{E}_1$, $\vec{E}_2$, $\vec{E}_3$, and $\vec{E}_4$. Each field can be expressed as $\vec{E}_n = E_{0n}e^{i\phi_n}$, where n ranges from 1 to 4. Each field has an associated phase ϕ_n and amplitude E_{0n}.

Using a strategy analogous to Equation (7.1), Equation (8.1) can be derived for a combined interferogram I_T of 4-beams with intensities I_a, I_b, I_c and I_d, respectively.

It becomes apparent from Equation (8.1) that the determination of the interferogram I_T in the context of the 4-telescope beam combination is significantly more intricate due to the additional phase and intensity terms.

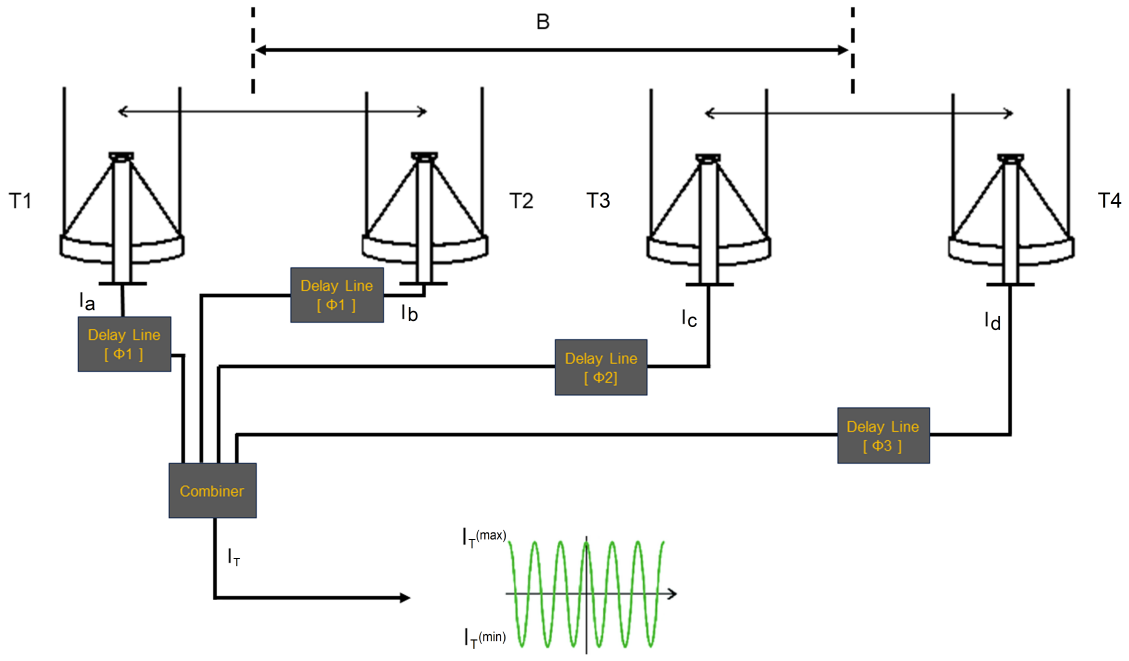

FIGURE 8.1: The schematic diagram of a 4-telescope interferometer for a monochromatic optical signal inspired by the double-Bracewell scheme of Angel & Woolf [79]. Telescopes T1 and T2, separated by a particular baseline, receive respective intensities I_a and I_b from an astronomical source such as a single-Bracewell scheme, as illustrated in Figure 7.1. Similarly, telescopes T2 and T3 receive intensities I_c and I_d from the same sources using the same baseline length. The centre-to-centre distance of these two baselines, B, is the baseline of this 4-telescope interferometer. Four delay lines are introduced to equalise the lengths of the optical paths before reaching the beam combiner, where four signals are combined according to the principle of wave superposition to generate the interferometric signal I_T. Different delay position arrangements can introduce overall constructive and destructive interferometric fringes, denoted as $I_T(max)$ and $I_T(min)$, respectively.

$$
\begin{aligned}
I_T &= |\vec{E_T}.\vec{E_T}^*| \\
&= (\vec{E_1} + \vec{E_2} + \vec{E_3} + \vec{E_4}).(\vec{E_1} + \vec{E_2} + \vec{E_3} + \vec{E_4})^* \\
&= (\sum_{n=1}^{4} |E_{0n}|e^{i\phi_n}) \cdot (\sum_{n=1}^{4} |E_{0n}|e^{-i\phi_n}) \\
&= I_a + I_b + I_c + I_d + \sum_{n=1}^{4} \sum_{m=1, m\neq n}^{4} E_{0n}E_{0m}^* e^{i(\phi_n - \phi_m)}
\end{aligned}
\tag{8.1}
$$

Furthermore, the computational challenge extends to applying photometric correction, as the derived generalised interferogram leads to multiple trigonometric functions from its exponential term. In contrast, the 2-telescope configuration contains only one trigonometric function (Equation (7.8)). Also, the system requires simultaneous scanning of multiple delay lines for adding different phase values across the injected beams to fully solve Equation (8.1). This task would require a more elaborate experimental test bed. Hence, a systematic case-by-case approach has been adopted to characterise the interferometric and nulling performance of the 4-telescope beam combiner, designated as the *Static Method*. This approach has been used previously for simple 2T telescope combiners such as directional couplers and multimode interference (MMI) couplers [130].

Explaining the *Static Method* requires understanding of the internal behaviour of the 4T-Nuller using a phasor representation of the electric field.

8.1.1 Self-calibrated null using the 4T-Nuller

Figure 8.2 shows a sketch of the 4T-Nuller to assist in the understanding of how the electric fields are split and combined inside the beam combiner. The inputs T1, T2, T3, and T4 are designated with colour codes: green, yellow, red, and blue, respectively. Each signal is depicted as a phasor, where the arrow's length indicates the amplitude (not scaled) and its direction represents the phase.

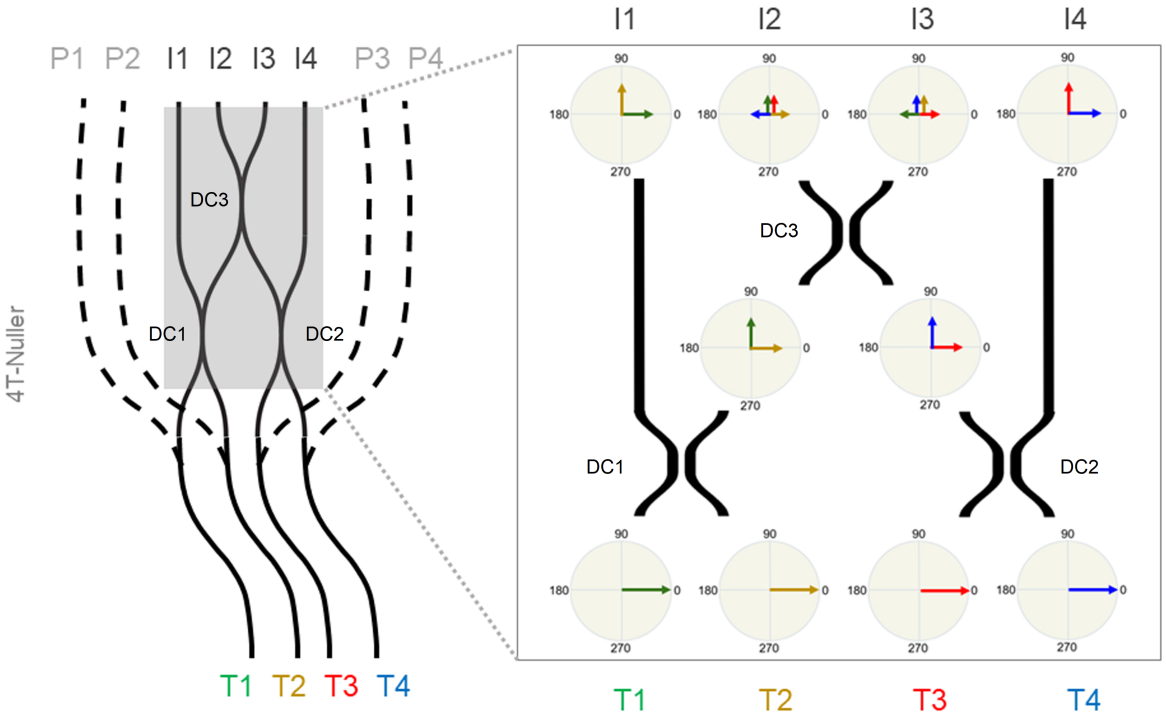

FIGURE 8.2: The left side features a schematic of the 4T-Nuller's internal waveguide layout, while the right side provides a representation of how the electric fields of the four inputs T1, T2, T3, and T4 are split and combined within the interferometric section of the 4T-Nuller. The inputs T1, T2, T3, and T4 are colour-coded as green, yellow, red, and blue, respectively. Each signal is represented by a phasor, where the length of the arrow corresponds to the amplitude and the arrow's direction to the phase. All injected beams exhibit identical amplitude and phase. Subsequently, 50/50 directional couplers split the *intensity* in half and introduce a phase shift of $\pi/2$ upon cross-coupling. Based on this, one can determine the interferometric output intensities labelled I1, I2, I3, and I4 from the superposition of the input complex amplitudes under the condition $I \propto |A|^2$

It can be considered that in the beginning, the injection has all beams with identical, i.e. zero path-length delay or phase offset and of equal amplitude. The initial two 50/50 directional couplers, DC1 and DC2, split the injection intensity in half and impart a phase shift of $+\pi/2$ on the cross-coupled beams, where light couples from one waveguide across to the other. The phase shift is intrinsic to directional couplers, as discussed in detail in Chapter 6. The third directional coupler, DC3, combines the signals from one arm each of DC1 and DC2. The signals undergo 50/50 splitting in the second stag,e and a $+\pi/2$ phase shift is applied upon cross-coupling.

For performing a nulling beam combination with the 4T-Nuller, it necessitates the adoption of a self-calibrated null configuration, exemplified in Case [I] in Figure 8.3. One can create different kinds of configurations that allow two nulled outputs from I_2 and I_3, but a self-calibrated null configuration refers to a case where I_2 and I_3 will have such an arrangement where T1 and T2 beam will cancel each other and T3 and T4 beam will cancel each other. For Case [I], two of the injection beams, T1 and T4, share the same phase. The two other beams, T2 and T3, are introduced into the beam combiner with a $+3\pi/2$ phase difference compared to T1 and T4.

This arrangement generates two mirrored transmission map nulls I_2 and I_3 from the two outputs of the central combiner. The other two interferometric outputs, I_1 and I_2, produce constructively superpositioned signals of T1 - T2 and T3, -T4, respectively. Alternative phase arrangements at the injections can also be used to obtain the two nulled outputs from DC3.

Following, to determine the maximum achievable intensity levels at I_2 and I_3, as well as their respective null depths Case [II] and Case [III] are considered.

Nulling interferometry requires stability, particularly when the signals are in destructive interference. It demands continuous wavefront control and precise path length matching between input signals. This rapid correction of differential piston variations directly influences the leakage term in the null channel. So far, statistical models and methods have been developed to measure null-depth under environmental variations, as discussed in Chapter 7 for the 2T-Nuller.

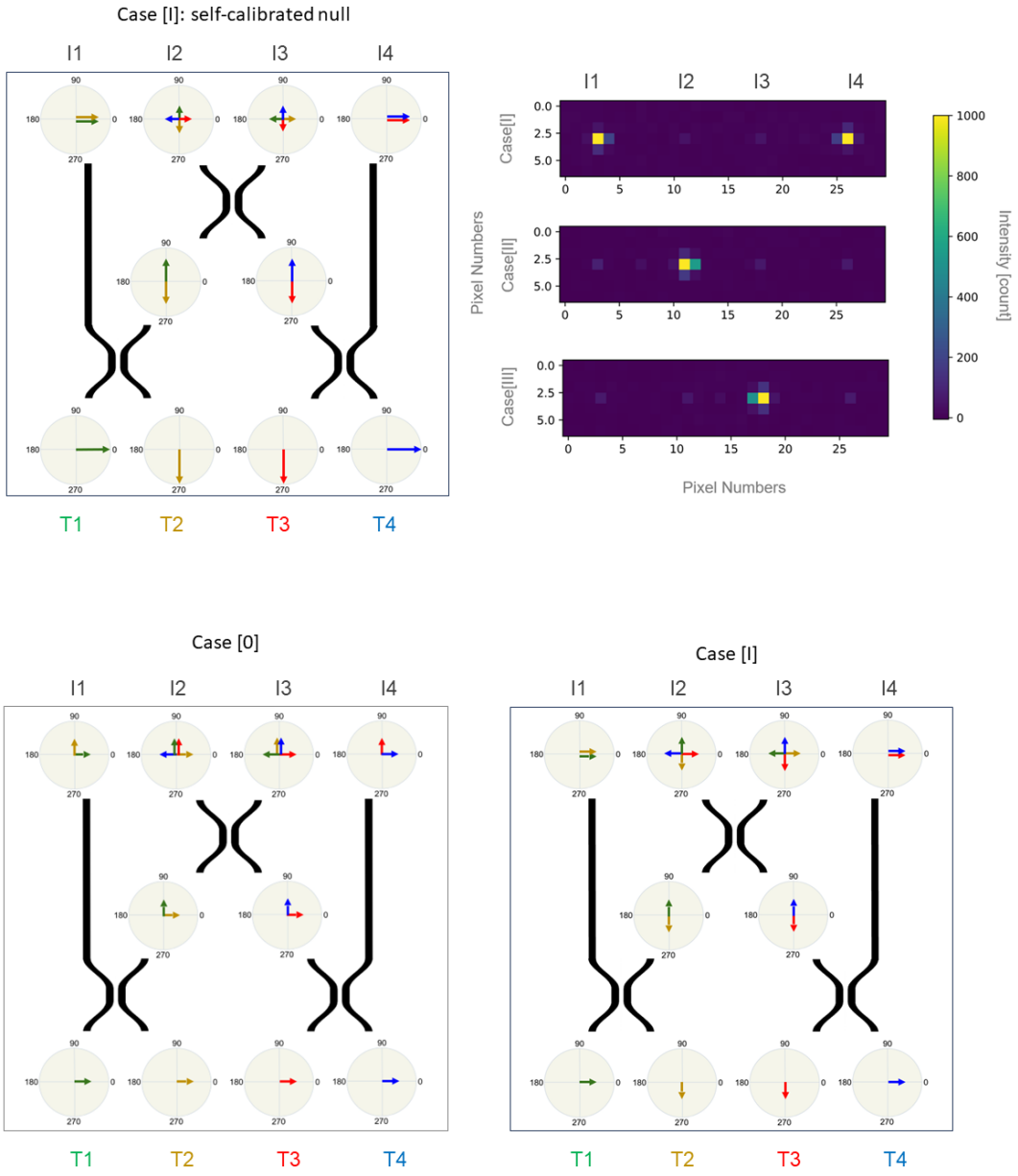

FIGURE 8.3: Three distinct injection scenarios, Cases [I] to [III], are investigated using the 4T-Nuller and presented in schematic as derived from the arrangement depicted in Figure 8.2. In Case [I], two distinctive nulls are generated at the central directional coupler. Such configuration will be used during on-sky operation. Cases [II] and [III] aid in determining the maximum achievable intensity levels at I_2 and I_3, as well as their respective null depths, individually.

However, this approach adds additional challenges due to the extensive model fitting requirements. Usually, model fitting significantly increases complexity because it requires large datasets to identify accurate statistics, such as used in Kernel [191].

Hereafter, the concept of direct self-calibrated nulling emerges as a handy solution, where multiple nulling outputs can be used to mitigate the impact of residual wavefront errors and other experimental errors. Such a solution has been previously proposed for the double-Bracewell architecture [79; 192; 82], and improved over time, such as recent improvement adds the advantage of mitigating photon noise and closure phase to combat optical aberrations using a tri-coupler [31].

A more versatile solution is found in more recent integrated optics based two staged beam combiners of 3×3 and 3×6 couplers, which can generate nulled outputs with linear combinations that yield self-calibrated observables, known as kernel-nulls [45]. A kernel-null is robust against upstream differential pistons and phase errors [191]. Kernel-nulls are created by subtracting the measured intensities of two nulled outputs, where the electric field in the two outputs are complex conjugates of each other. Hence, it is also called a differential null. Recent advances have demonstrated kernel-nulls for 3-input [157] and 4-input [193; 194] photonic beam combiners using UV-photolithography fabricated MMI couplers.

Creating the complex conjugate of input fields using photonic interferometers involves a beam-combination architecture where the input beams are recombined by phase offsets, as illustrated in Case [I] of Figure 8.3. Mathematically, Case [I] is expressed as Equation (8.2) for two nulled outputs, $null_1(t)$ and $null_2(t)$, created by the central combiner. k as a function of time t is the self-calibrated null or the kernel null defined as the difference between $null_1(t)$ and $null_2(t)$ [157],

$$k(t) = |null_1(t) – null_2(t)| \tag{8.2}$$

Equation (8.2) means that the kernel null is unaffected by instrumental errors since the difference between $null_1(t)$ and $null_2(t)$ cancels them [193; 43].

Apart from mathematical representation, Figure 8.4 represents a transmission map of a kernel null for a linearly arranged 4-telescope interferometer. Subtracting the two nulled outputs preserves the planet's transmission while removing starlight (or any residual).

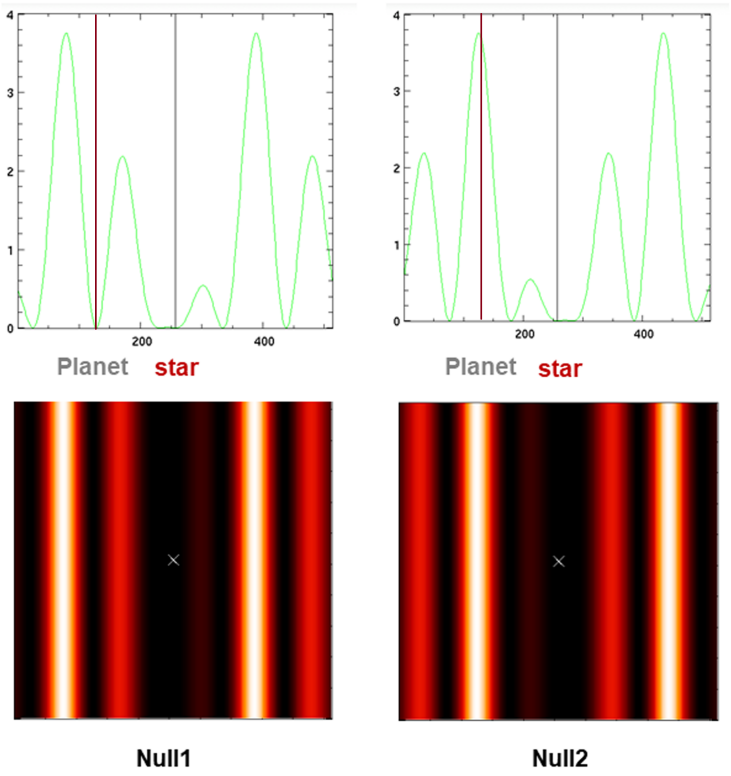

FIGURE 8.4: Example of a 4-telescope nuller transmission map gives the transmitted flux for a source depending on its angular position in this map. The centred positions of the star (black line) and planet (brown line) along the horizontal line, approximately at 210 and 130, respectively, for the two nulled outputs labelled as $Null_1$ and $Null_2$. The subtraction between the transmission maps enables the removal of the star's signal while the planet remains visible. The field of view of this transmission map is 50 mas, and the coordinate origin is set arbitrarily in the centre of the map where the central star is located (white cross).

8.2 Experimental characterisation of the 4T-Nuller

The particular 4T-Nuller chosen for performing the interferometric characterisation featured directional couplers with an interaction length of 7.5 mm, fabricated as part of SAMPLE III. For this interaction length, the central directional coupler, DC3, exhibited 50/50 splitting, while for the same interaction length, the first two directional couplers, DC1 and DC2, showed 60/40 splitting. However, all directional couplers showed achromaticity. The splitting ratios of the Y-junctions for photometry were 40/60. The wavelength-resolved splitting ratios are shown in Figure 5.3. To obtain a deep null, the splitting ratio of the central directional coupler is most crucial and should be as close to 50/50 as possible.

8.2.1 Input-dependent flux imbalance

As discussed for the 2T-Nuller, perfectly balanced flux before the directional coupler is mandatory to achieve the highest contrast or deepest null. In order to assess the flux imbalance of the 4T-Nuller, the relative amount of light emerging from every output, including photometry, was measured by individually injecting the same beam of the test bench sequentially into each of the four inputs T1, T2, T3, and T4. For each separate injection, the resulting outputs consisted of one photometric signal and three interferometric signals.

Optimisation of the input coupling was achieved via a 5-axis stage on which the GLS chip was mounted while real-time monitoring of the corresponding output intensities was performed using the mid-IR camera. The camera measures the flux across 3.65 to 3.85 μm. Figure 8.5 shows the output intensities acquired after averaging across the frames of a 20 seconds long recording.

Due to the 60/40 splitting ratio of DC1 and DC2, the amount of light reaching DC3 depends on the injection input. Looking at Figure 8.5, for injection into the inputs T2 and T3, the central outputs I_2 and I_3 are higher compared to those for the inputs T1 and T4. Thus, like for the 2T-Nuller, the injection beams were adjusted manually by tilting the mirrors to ensure that, for every input signal, the amount of flux emerging

from the central directional coupler DC3 was equal. This adjustment was crucial for achieving the desired balance required for the self-calibration process, which ensures that the beam combination scheme maintains uniform intensity levels across all beams.

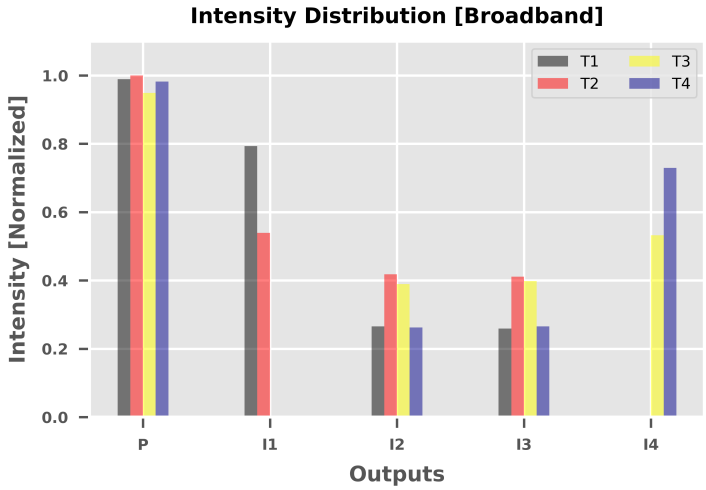

Figure 8.5: Normalised output intensities for the four inputs T1, T2, T3, and T4 of the 4T-Nuller under sequential broadband illumination of each individual input (T1 to T4). Normalisation is performed against the maximum illumination

8.2.2 Dynamic cross-talk

Figure 7.3 in Chapter 7 shows that the photometry channels of the 2T-Nuller exhibit a small sinusoidal variation in the output flux as the delay line moves. This coherent background was assumed to be from cross-talk within the chip. However, under static-illumination of just a single input, no light could be detected, even for long exposures, at the photometry output of the dark input. This illustrates that there is no static cross-talk in the 2T-Nuller. The same static experiment was repeated for the 4T-Nuller with identical results.

To check for dynamic cross-talk, the interferometric test bench (see Figure 3.3) was used. An injection state was created by adjusting the delay line of T2 to bring I_1 to constructive interference with light from T1. Then, inputs T3 and T4 were injected,

and the delay line of T4 was moved while monitoring I_1 for any periodic intensity changes. A recorded time trace is depicted in Figure 8.6 (top).

A similar approach was adopted to check for interference on I_4. First, the delay between T3 and T4 was adjusted to maximise the flux from I_4. Inputs T1 and T2 were then injected, and the delay line for T2 was scanned. Like I_1, I_4 also did not exhibit any periodic flux variations, as illustrated in Figure 8.6 (bottom). These results show no dynamic cross-talk between the interferometry inputs on opposite sides of the chip.

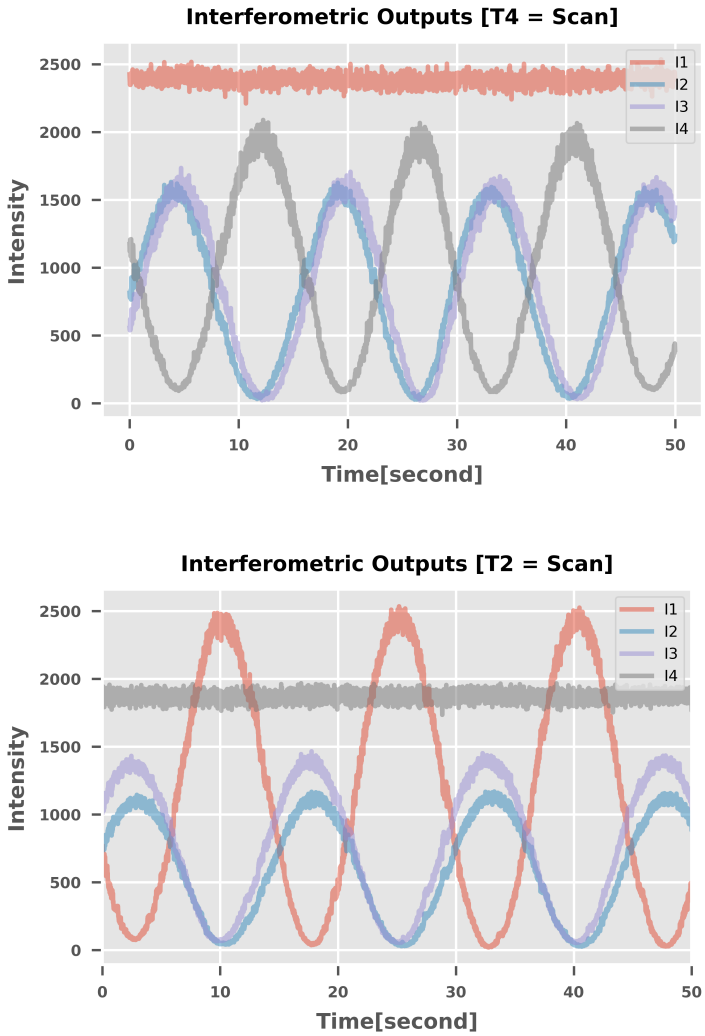

FIGURE 8.6: Time series of the interferometric signals when either scanning the T4 delay-line (top) or the T2 delay-line (bottom). No dynamic cross-talk could be observed in output I_1 and I_4, respectively.

However, the scenario differs for photometric channels. Periodic flux variations were observed in their outputs when different delay lines were scanned within the coherent envelope of the injected light. Within the setup, the injection beam for T1 originated from a static mirror. Therefore, T1's beam was not scanned. The T2, T3, and T4 beams were each incorporated with delay lines. Subsequently, after injecting all four beams into the four inputs simultaneously, T2 was scanned first, followed by the T3 beam, and finally, the T4.

Table 8.1 lists which input delay line causes periodic variations in the photometry channels.

Table 8.1: Dynamic cross-talk between input and photometric channels; yes refers to the presence of periodic variations, and no refers to an absence of periodic variations.

Delaylines/Scan	P_1	P_2	P_3	P_4
T1	not applicable	not applicable	not applicable	not applicable
T2	yes	yes	yes	no
T3	no	yes	yes	yes
T4	no	no	yes	yes

Comparing the results in Table 8.1 to the 4T-Nuller's geometry (see Figure 8.2) shows each input influences its nearest neighbour photometric outputs. A potential source for this dynamic cross-talk could be the Y-junctions themselves. Comparing the throughput between reference directional couplers and Y-junctions indicates that Y-junctions are $\approx 7\% \pm 4\%$ more lossy than directional couplers.

The Y-junctions in the 4T-Nuller are not ideal with their 40/60 splitting ratios. The optimised Y-junctions slated for the iteration of the 4T-Nuller have $\approx 22\%$ higher transmission compared to 40/60 Y-junctions, as discussed in Chapter 5. With lower photon loss and hence less background light, it is expected that the dynamic cross-talk will be less.

As the interferometric sections remained unaffected by this dynamic cross-talk, alternative Y-junctions inscription parameters are available for future iterations, and

the decision was made to perform nulling or astronomical performance using the *static method*, which does not require photometric channels. The primary emphasis shifted towards the nulling measurements from cross-talk to fit the timeframe of this thesis. Afterwards, more attention can be given to investigating cross-talk.

8.2.3 Measuring null depth

Nulling with the 4-telescope beam combiner is more complex compared to the 2-telescope beam combiner because, by design, the four interferometric outputs do not produce simultaneous constructive and destructive interference fringes. Hence, a specific injection state, as illustrated in Figure 8.3, is required. Unlike with the 2T-Nuller, the photometry signals were not used during the 4T-Nuller measurements. In the experimental setup, the initial beam injected into T1 was considered a reference, while the subsequent beams T2, T3, and T4 were equipped with individual delay lines. The schematic diagrams of Figure 8.3 portray the signal propagating through each directional coupler, undergoing coupling and accumulating a $+\pi/2$ phase shift. The self-calibrated null, Case [I], is the optimal scenario in which central outputs I_2 and I_3 produce two perfect nulls similar to the kernel null.

To create this injection state experimentally, individual scanning of T2, T3, and T4 delays was conducted to ensure that collectively, they created the desired condition when all beams from the four inputs of the 4T-Nuller were combined. For instance, the I_1 and I_2 outputs were observed while simultaneously launching two beams in the input T1 and T2 of the 4T-Nuller. The beam of T2 was scanned to reach the fringle where I_2 is in destructive most. Similarly, other beams out injections were employed and scanned two at a time to ensure that I_2 and I_3 were collectively in distinctive fringes for all combinations.

The same approach was employed to create the situations described in Case [II] and Case [II]. These cases can be used to measure the contrast or null depth at I_2 and I_3, respectively.

The raw null, N[raw], for the self-calibration injection state was calculated using Equation (8.3). Here, the two central nulls are determined as the sum of destructively

interfered intensities ΣI_- divided by the sum of the constructively interfered intensities ΣI_+. This quantification represents the total extinction or nulling ability of the 4T-Nuller. The self-calibrated null N[self-calibration] is defined as the absolute difference between destructive or nulled intensities, i.e. the kernel, divided by the sum of constructive intensities.

$$\begin{aligned} N[\text{raw}] &= \frac{\sum I_-}{\sum I_+}, \\ N[\text{self-calibrated}] &= \frac{k(t)}{\sum I_+}. \end{aligned} \tag{8.3}$$

The plots of Figure 8.7 (top and middle) were obtained by recording output intensities at a frame rate of 50 Hz over a 60-second period. The delay lines were set to create the injection state of Case [I]. The left graph illustrates nulled output intensities I_2 and I_3 over time together with the detector background. The background signal was taken from a pixel value away from the output of the chip, as illustrated in the top right corner of Figure 8.3. It is noticeable that after the initial ≈ 30 seconds, the intensities of I_2 and I_3 drift and gradually increase due to environmental changes in the laboratory. Hence only the first 20 seconds are considered for the subsequent analysis. The laboratory conditions are affected by the presence of the operator and heat output from the different running electronic systems, such as the supercontinuum source itself. The nulled signals can also be influenced by the higher tension in the internal spring of the delay line and vibrations. This sensitivity of interferometric characterisation of beam combiners to environmental influences has been previously discussed in a study focusing on 10 μm wavelength, where the first 20 seconds demonstrated optimal results [195].

8.2.4 Discussion

The average raw null, N [raw], is found to be 0.0273 with a standard deviation of 0.0058. The average self-calibrated null, N [self-calibration], is 0.00075 with a standard deviation of 0.00069, calculated from the kernel by subtracting both central nulled outputs. Signal-to-noise ratios between self-calibrated null and the average of arbitrary

nine background pixes were found to be 0.000016.

Figure 8.7 (bottom) shows the raw null and self-calibrated null, obtained using Equation 8.3. Self-calibration is not presented as the absolute value as stated in the equation. It is to represent that subtraction between nulled outputs (I_2 and I_3) goes below complete zero, which is a combined reason that appears from the high-frequency noise and read-out noise of the detector.

The individual nulls, by extracting the flux levels for I_2 and I_3, were identified through the input states of Case [II] and Case [III]. The rejection levels were determined as 0.051 $\pm$ 0.002 and 0.052 $\pm$ 0.002, respectively. This finding indicates that the rejection levels of both central outputs are notably comparable. These extinction ratios are relatively higher compared to the achromatic directional couplers or 2T-Nuller due to the fact that two of the directional couplers at the initial phase are not 50/50 achromat of this particular 4T-Nuller.

Besides, the science case for ASGARD/NOTT is to detect exoplanets with masses of 10 $M_{Jupiter}$ masses orbiting a Sun-like star. This investigation encompasses three distinct age categories, falling within a magnitude scale of 8 $\pm$3 within the L' band [33].

By denoting m_s as the magnitude of the parent star and m_p as the magnitude of the planets observed by NOTT, the intensity level of the planet I_p with respect to its star I_s can be expressed as $m_p - m_s = 2.5 \log(\frac{I_s}{I_p})$, relying on the foundational principles of the magnitude scale standardised by Pogson [196] using much earlier star cataloguing technique introduced by Hipparchus.

This gives the starlight nulling or cancellation requirement as $\frac{I_p}{I_s} = 10^{-2}$ to 10^{-5} to detect exoplanets within the specified magnitude range of 8 $\pm$3. This range aligns with the experimentally obtained broadband nulls from both, the 2T-Nuller and 4T-Nuller. By implementing 4T-Nuller self-calibration, the starlight cancellation can be increased to the level of 10^{-4}. A comparison between conventional raw null and self-calibrated null is presented in Table 8.2.

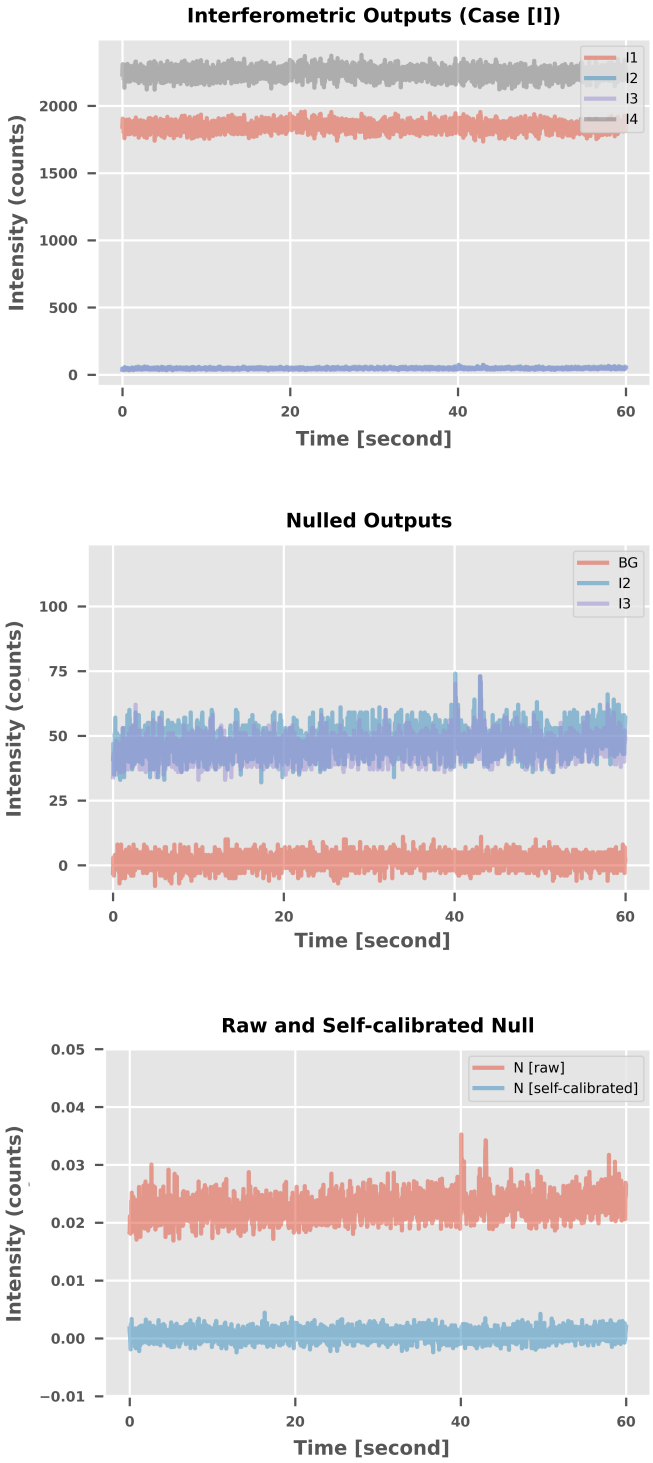

Figure 8.7: (Top) Injection state of Case [I] showing the intensity counts over time of all four interferometric outputs I_1 to I_4. (Middle) zooming to the two null outputs (I_2 and I_3) from the central combiner of the 4T-Nuller. A background signal (BG) has been extracted from a detector array away from the 4T-Nuller's outputs. (Bottom) Raw and self-calibrated null depth according to $(I_2 + I_3)/(I_1 + I_4)$ for the raw null and $(I_2 - I_3)/(I_1 + I_4)$ for the self-calibrated null. In the context of self-calibration, the absolute value of $|I_2 - I_3|$ is not utilised for demonstration.

Self-calibration achieves contrasts close to the requirement for detecting giant exoplanets already in warm laboratory experiments without using any Cryostat, which will house the beam combiner in the final instrument. In the warm, unstabilised environment, the measurements are influenced by the surrounding thermal background, as seen in Figure 3.4 (bottom). The residual thermal background appears at longer wavelengths beyond the L' bandpass that certainly influenced the null-depth measurements. Installing the 4T-Nuller inside a cryostat during operations is expected to enhance performance due to the absence of such residual signals. The photonic chip with the characterised 4T-Nuller is planned for testing inside a cryostat in mid-2024.

TABLE 8.2: Summary of the measured broadband null depths in the warm laboratory environment and the approximate contrast level required for achieving the ASGARD/NOTT science case.

2T-Nuller	**4T-Nuller**	**4T-Nuller (self-cal.)**	**ASGARD/NOTT (req.)**
Star: null	Star: null	Star: null	Planets: estimated
10^{-2}	10^{-2}	10^{-4}	10^{-2} –10^{-5}*

* within the magnitude 8 ±3

In recent years, nulling interferometry has seen a renaissance, particularly with the help of integrated optics inspired by the successes of the GLINT instrument at Subaru. GLINT, an extension of the original two-telescope prototype, employs a four-input chip utilising directional couplers to generate sixteen spectrally dispersed outputs, including nulls, anti-nulls, and photometric channels. Insights derived from the GLINT experiment indicate that broadband nulls, post-dispersion, can achieve a much deeper null, approximately 3.8 times deeper in the case of GLINT, compared to its achromatic broadband nulls [76].

Within the lab demonstration, the contrast level has been found in the level of 10^{-3}, while on-sky observations of α Boo in nulling mode detected stellar leakage in the range of 10^{-2}, consistent with the expected stellar diameter [44]. The development of kernel nullers produces raw nulls of 10^{-3}, and the kernel distribution resulting from the subtraction of the two nulled outputs via self-calibration improves the null to $\approx 10^{-4}$.

Such advancements allow for the detection of simulated 10^{-2} dimmer companions at $\sim$ 2 mas separation in laboratory settings, signifying the progress in ground-based nulling techniques [157].

The laboratory-demonstrated raw and self-calibrated null range between 10^{-2} and 10^{-4} suggests that the tested 4T-Nuller in warm optics lab has capabilities comparable to existing state-of-the-art on-sky nulling devices, which can even further improve in temperature controlled on-sky situation.

Moreover, simultaneous with this dissertation's focus on developing the 4T-Nuller, a simulation package known as SCIFYsim is being developed at KU Leuven. The preliminary results from SCIFYsim estimate a self-calibrated null depth in the range of 10^{-3} to 10^{-4} at 3.75 μm for the overall instrument [43], which can detect faint astronomical objects up to 5 mas [50]. The experimentally measured null depth in broadband aligns with this level. Continued refinement of SCIFYsim's algorithms will provide further insights into the instrument's overall capabilities in addressing specific science cases.

9

Conclusion

This dissertation presented the development of a mid-infrared 4-telescope photonic beam combiner. The beam combiner is based on the double-Bracewell architecture and will be employed in the upcoming VLTI visitor instrument ASGARD/NOTT to perform nulling interferometry. The science goal of the instrument is the detection of young giant exoplanets located in their host star's snowline.

The work began with specific objectives aimed at ensuring that the 4-telescope photonic beam combiner meets the criteria outlined in the table 9.1. This table also highlights the accomplishment of the work alongside the specifications. Moreover, the work presented in this thesis builds upon the PhD research conducted by Thomas Gretzinger at Macquarie University [123], where he utilised the ultrafast laser inscription technique to fabricate low-loss triple track waveguides, also known as triplets and

asymmetric directional couplers. These components were developed using the multiscan method in a thermal regime within GLS glass, specifically for astrophotonics applications in the mid-infrared spectrum.

Table 9.1: Key photonic requirements for the ASGARD/NOTT [35; 33; 65; 34].

On-chip waveguides	Operational range	3.5-4.0 μm (GLS glass)	known
	Mode-field profile	Single-mode	known
Y-junctions	Splitting for photometric tap	20/80	40/60 (exist), 20/80 (identified)
	Chromaticity	Achromatic	Yes
Directional couplers	Splitting for beam combination	50/50	1 of 3 (exist), 3 of 3 (identified)
	Chromaticity	Achromatic	Yes
	Phase shift between two outputs	180 degree	Yes
4T-Nuller	Optical throughput	$\approx$ 50%*	$\sim$ 53%*
	Contrast level (raw and self-cal.)	$10^{-2} - 10^{-5}$	$10^{-2} - 10^{-4}$**

* without Fresnel loss

* * without cryostat

9.1 Current state of development

The work of this thesis can be intensified into two sections: (i) identifying correct Ultrafast Laser Inscription parameters to fabricate that can lead to fabricating a 4-telescope beam combiner through characterisation and iteration, and (ii) in-lab characterisations from the astronomical or on-sky perspective. The overall work can be summarised in the following order:

The Mode Field Diameters (MFDs) of the fabricated triple track waveguides (triplets) were measured against 3.39 μm, revealing measurements within the range of 26 to 28 μm. 0.21 to 0.29 dB/cm propagation loss was found in L' band for the triplets. The throughput difference between cosine S-bends and straight waveguides was found to be negligible. These results are relatively comparable to the previous work done by T. Gretzinger *et al.,* [150].

Next, the fabrication parameters of asymmetric directional couplers were optimised with iteration to achieve achromatic 50/50 splitting ratio. An optimal interaction length of 7.5 mm asymmetrical directional couplers demonstrated achromatic behaviour with a variation of 0.02% within the range 3.65 to 3.85 μm. It was also observed that the writing order significantly impacts the splitting ratios of directional couplers. The *left to right* writing order was found to be the correct order to obtain such achromaticity. Maintaining consistent writing orders and interaction length resulted in reproducible splitting ratios after performing iterations in two different batches of GLS glass.

Fabricated asymmetric Y-junctions from the insights of previous work in GLS glass [150] were found to have a 40/60 achromatic splitting ratio between photometry and interferometry branches. These Y-junctions were incorporated in nulling beam combiners. However, the requirement for NOTT is achromatic 20/80, which was later achieved by redesigning the Y-junctions. This involved 3D vertical offsetting (7.5 μm) of the photometry channel from the interferometry plane and determining the correct taper length (1.5 mm). This redesigned Y-junction not only achieved an achromatic 20/80 splitting ratio but also exhibited higher throughput compared to the previous 40/60 Y-junctions and is considered to be implemented in future iterations.

Subsequently, a two-telescope beam combiner (2T-Nuller) was designed and characterised as a part of the astronomical perspective. The characterisation technique used is called the *dynamic method*, where contrast and null results were obtained using four mechanisms: raw interferogram, curve-fitting interferogram to reduce high-frequency noise, photometrically corrected interferogram, and simultaneous photometrically corrected interferograms using photometry branches. All methods displayed comparable contrast and null levels, ~ 0.95 and $\sim 10^{-2}$, respectively. These results are comparable to the work of J. Tepper [159], who reported a contrast of ~ 0.94 in GLS glass at the University of Cologne with a symmetric directional coupler. Moreover, dynamic crosstalk was observed in the 2T-Nuller's photometry channel, which remains unresolved within the time frame of this thesis and requires extended characterisation.

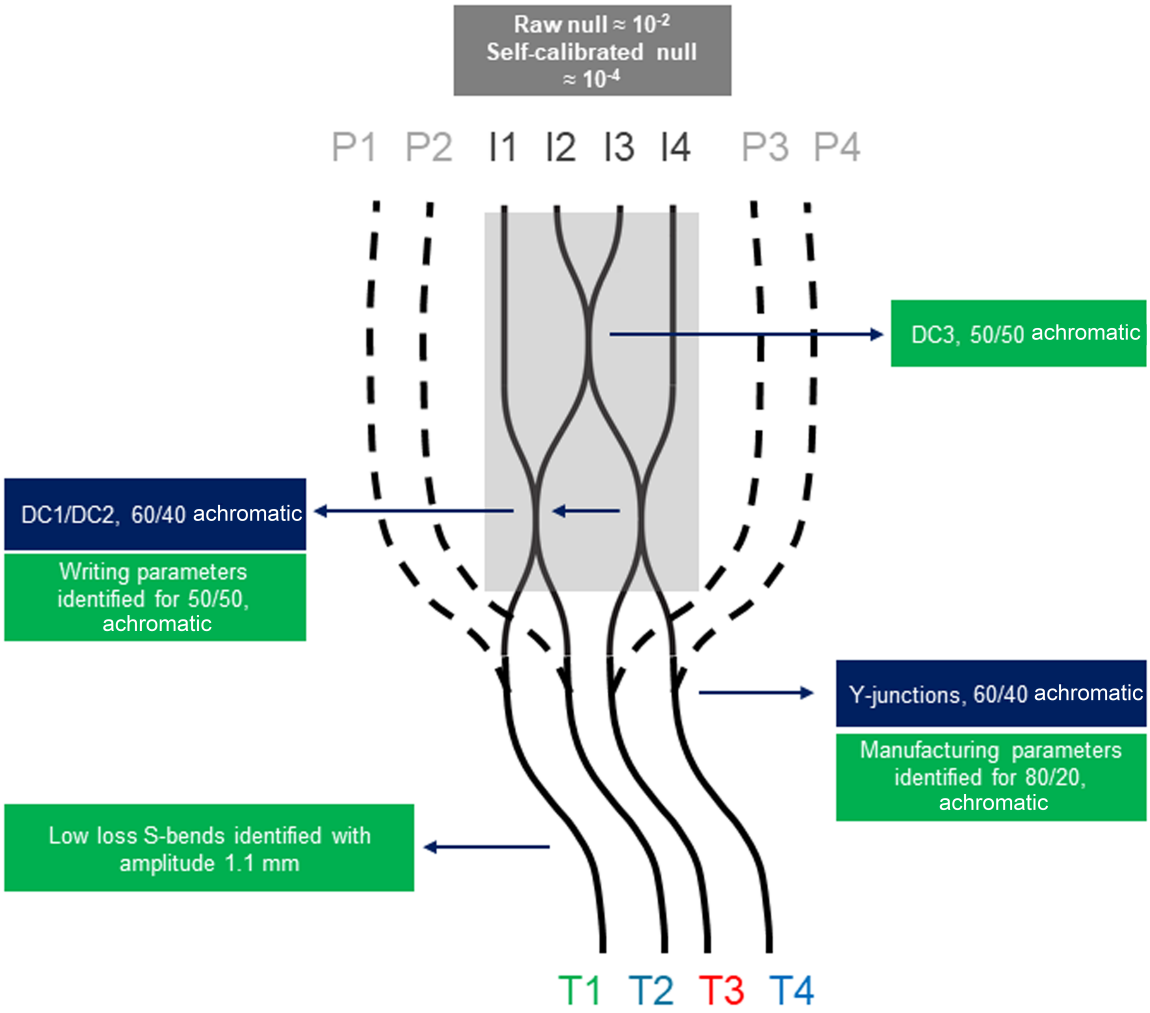

Figure 9.1: Summary of the current status of the ASGARD/NOTT's 4T-Nuller. The key performance of the beam combiner components achieved as part of this thesis are highlighted alongside with the ASGARD/NOTT requirements.

Finally, the four-telescope beam combiner (4T-Nuller) of double-Bracewell architecture, the main requirement of the NOTT, was characterised using the *static method* with a four-telescope configuration. The examined 4T-Nuller's throughput was $\approx 37\%$ (with Fresnel loss). The Y-junctions had a $\sim 40/60$ achromatic splitting ratio for photometric separation and a two-staged configuration in its interferometric section. The first stage contains two achromatic directional couplers (DC1/DC2) with 60/40 splitting ratios, and the second stage combines two nulled signals with another directional coupler (DC3) of 50/50 achromat. The 4T-Nuller was used to identify raw nulls, which were of a similar order of 10^{-2} as in 2T-Nullers. However, in self-calibration mode, it reached up to 10^{-4} in warm optics lab environments.

Figure 9.1 provides a visual representation of the examined 4T-Nuller, annotating the achievements achieved and identifying areas that require further improvement for the second phase of the upgrade.

9.2 Future work

9.2.1 Installation and tests

The installation of the 4T-Nuller chip, as depicted in Figure 9.2, within the NOTT cold-optics cryostat is anticipated to be completed by the second half of 2024. Before full instrument tests, anti-reflection coatings on the end-faces of the beam combiner are required to mitigate Fresnel reflection losses. At this moment, 4T-Nuller is undergoing differential dispersion testing. Preliminary results are demonstrated in Appendix A. Null measurements need to be carried out using the procedure devised for self-calibrating nulling, as outlined in Chapter 8, while the chip operates within the cold optics environment of the cryostat. This leverages a recently developed test bench at KU Leuven, Belgium [34]. KU Leuven is performing the lab assembly of the instrument and developing the instrument control algorithms and alignment routines. The test phase will ensure the chip's performance within the cold environment optics. Based on the findings, further investigation is needed to align with the simulation packages

currently under development and identify any non-compliance with instrument requirements. This will help determine which specific science cases can be accomplished and which may be compromised.

Upon completion of these steps, the chip will be dispatched for final integration into the ASGARD main suite.

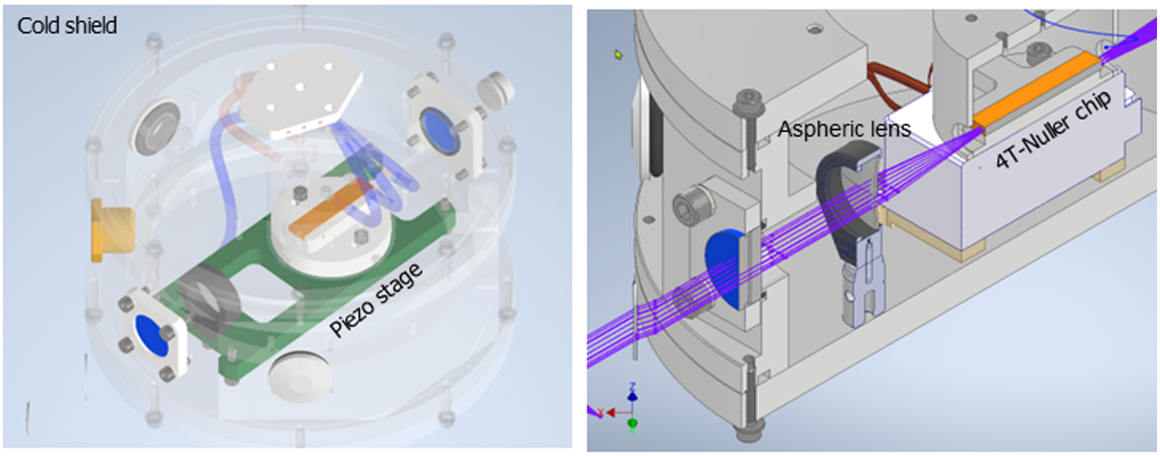

Figure 9.2: The schematic of the cryostat shows the location of the photonic chip on top of a piezo stage for alignment. In front of the photonic chip is the aspheric injection lens that focuses the beams from the 4 Unit Telescopes (UTs) of the VLTI facility. Image source: ASGARD workshop 2023, KU Leuven.

9.2.2 Beam combiner upgrade

The current 4T-Nuller deviates slightly off from the ideal specifications required for NOTT. Hence, the fabrication of a new beam combiner is anticipated that incorporates the optimised Y-junctions to achieve achromatic 20/80 splitting between interferometry and photometry, where the length of the three cascaded directional couplers also has to be adjusted to meet 50/50 splitting. With the identified geometric parameters to achieve that requirement, multiple identical 4T-Nullers can be placed inside a single substrate to mitigate the influence of defects intrinsic to the GLS glass samples.

A

Appendix: Differential dispersion

Differential dispersion refers to the difference in the dispersion as a function of wavelength experienced by two light waves as they propagate through a multiport photonic component, such as a directional couplers for instance. Dispersion causes the different wavelengths of light to travel at different speeds, leading to a spreading of the light pulses over time. Typically, dispersion is a limitation factor when using integrated optics or fibres for interferometry. It is associated with different propagation constants and/or different lengths between the two optical paths of lengths L_1 and L_2. This is illustrated for a coupler in Figure A.1.

The dispersion parameter D is quantified as $D = \tau_G/\lambda$, where τ_G is the group delay and λ is the wavelength of light. The group delay represents the time needed at wavelength λ to travel through a particular optical path. The dispersion is associated with the interferogram's phase. Equation (A.1) describes the relation between dispersion

and phase [197].

$\Delta D = D_1 - D_2$ is the average dispersion parameters between two optical paths L_1 and L_2, c is the speed of light, and $d^2\phi/d\sigma^2$ is the second derivative of the phase ϕ with respect to the wavenumber σ.

$$\frac{d^2\phi}{d\sigma^2} = -2\pi c\lambda^2(D_2\Delta L + L_1\Delta D) \tag{A.1}$$

For the directional couplers, due to their symmetric waveguide paths, one can assume that $\Delta L = 0$. Thus, Equation (A.1) can be simplified to $\frac{d^2\phi}{d\sigma^2} = -2\pi c\lambda^2 \cdot L\Delta D$, where $L = L_1 = L_2$. This simplified relation can be fitted as a polynomial to the second derivative of the phase over the bandwidth. The phase as a function of wavelength can be obtained from the interferogram through the Fourier transform.

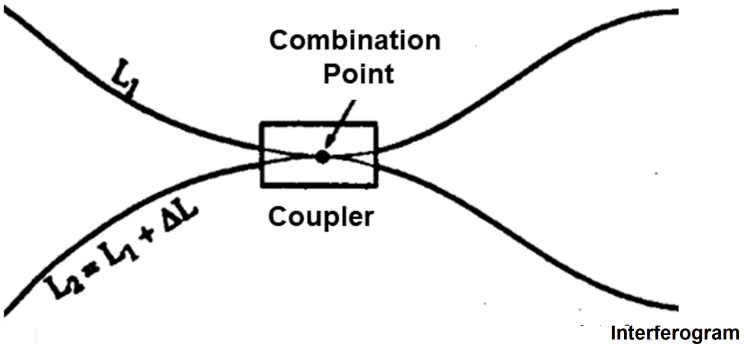

FIGURE A.1: Layout of a coupler, indicating the length of L_1 and L_2 before the region of beam combination. Image credit: [197].

To measure the dispersion parameter of the 4T-Nuller, only one of the Michelson interferometers (MI-1) from experimental setup II of Figure 3.3 was used.

First, an interferogram of the bench was obtained without the beam combiner in place. The interferogram was measured using the supercontinuum source (SCS) after OPD correction using 3.39 μm HeNe laser using photometrically corrected interferogram.

A similar approach was employed to identify $L \cdot \Delta D$ of the 4T-Nuller's output I_1 of DC1 by injection into T1 and T2. To obtain the phase of output I_4 of DC2, light was injected into T3 and T4. For injection into T1 and T2, the metrology signal from 3.39 μm HeNe laser to calibrate the delay lines was recorded from output I_4, while for T3 and T4, the metrology signal was collected from I_1. $L.\Delta D$ of the test bench was subtracted from the 4T-Nuller data to remove the test bench's influence. Figure A.2 shows the calculated phases.

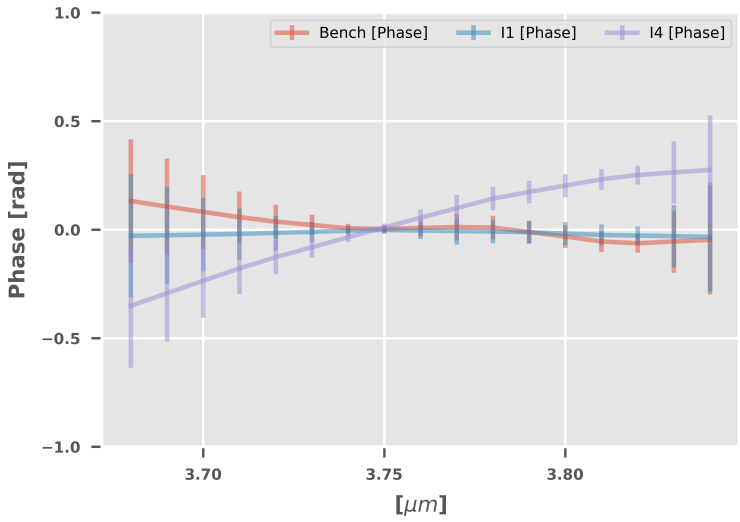

FIGURE A.2: Normalised phases for the two outputs I_1 and I_4 as well as the phase of the bench without chip over the L' band. The lines represent the average values of three measurements while the error bars represent three times of standard deviation.

$L.\Delta D \approx 3.3 \times 10^5$ ps/nm is identified for I_1 and I_4. This value is in good agreement with $L.\Delta D \approx 3.6 \times 10^5$ ps/nm obtained by Tepper *et al.*, [159] for an ULI directional coupler for the L band.

The dispersion parameters for I_2 and I_3 could not be investigated due to limitations of recording simultaneous metrology interferograms with the monochromatic 3.39 μm HeNe laser. For injection into T2 and T3, all outputs are illuminated by a superposition of light from the supercontinuum source and the reference laser, yet the delay calibration requires an isolated signal from the HeNe laser alone.

References

[1] G. Bruno. *On the infinite, the universe and the worlds: Five cosmological dialogues*. Trans. by Scott Gosnell. Port Townsend, WA: Huginn, Muninn and Co (2014). 1

[2] *Nasa exoplanet science institute. 2024, nasa exoplanet archive*. URL `https://exoplanetarchive.ipac.caltech.edu/index.html`. 2, 3

[3] M. Mayor and D. Queloz. *A jupiter-mass companion to a solar-type star*. nature **378**(6555), 355 (1995). 2

[4] A. Wolszczan and D. A. Frail. *A planetary system around the millisecond pulsar psr1257+ 12*. Nature **355**(6356), 145 (1992). 2

[5] D. Charbonneau, T. M. Brown, D. W. Latham, and M. Mayor. *Detection of planetary transits across a sun-like star*. The Astrophysical Journal **529**(1), L45 (1999). 2

[6] L. Sun, S. Gu, X. Wang, A. C. Cameron, D. Cao, Y. Wang, Y. Xiang, H.-K. Hui, C.-T. Kwok, B. Yeung, *et al. Refined system parameters and ttv study of transiting exoplanetary system hat-p-20*. The Astronomical Journal **153**(1), 28 (2016). 2

[7] V. Bozza, L. Mancini, A. Sozzetti, *et al. Methods of detecting exoplanets*. Astrophysics and Space Science Library: Berlin, Germany **428** (2016). 2, 3

[8] J.-P. Beaulieu, D. P. Bennett, P. Fouqué, A. Williams, M. Dominik, U. Jørgensen, D. Kubas, A. Cassan, C. Coutures, J. Greenhill, *et al. Discovery of a cool planet of 5.5 earth masses through gravitational microlensing.* Nature **439**(7075), 437 (2006). 2

[9] Z. Dai, D. Ni, L. Pan, and Y. Zhu. *Five methods of exoplanet detection.* In *Journal of Physics: Conference Series*, vol. 2012, p. 012135 (IOP Publishing, 2021). 2

[10] R. Galicher and J. Mazoyer. *Imaging exoplanets with coronagraphic instruments.* Comptes Rendus. Physique **24**(S2), 1 (2023). 3, 4

[11] R. Akeson, X. Chen, D. Ciardi, M. Crane, J. Good, M. Harbut, E. Jackson, S. Kane, A. Laity, S. Leifer, *et al. The nasa exoplanet archive: data and tools for exoplanet research.* Publications of the Astronomical Society of the Pacific **125**(930), 989 (2013). 3

[12] Q. M. Konopacky, T. S. Barman, B. A. Macintosh, and C. Marois. *Detection of carbon monoxide and water absorption lines in an exoplanet atmosphere.* Science **339**(6126), 1398 (2013). 4

[13] J. Wang, J. R. Kolecki, J.-B. Ruffio, J. J. Wang, D. Mawet, A. Baker, R. Bartos, G. A. Blake, C. Z. Bond, B. Calvin, *et al. Retrieving the c and o abundances of hr 7672 ab: A solar-type primary star with a benchmark brown dwarf.* The Astronomical Journal **163**(4), 189 (2022). 4

[14] J.-B. Ruffio, Q. M. Konopacky, T. Barman, B. Macintosh, K. K. Hoch, R. J. De Rosa, J. J. Wang, I. Czekala, and C. Marois. *Deep exploration of the planets hr 8799 b, c, and d with moderate-resolution spectroscopy.* The Astronomical Journal **162**(6), 290 (2021). 4

[15] J. J. Wang, J.-B. Ruffio, E. Morris, J.-R. Delorme, N. Jovanovic, J. Pezzato,

D. Echeverri, L. Finnerty, C. Hood, J. Zanazzi, *et al. Detection and bulk properties of the hr 8799 planets with high-resolution spectroscopy.* The Astronomical Journal **162**(4), 148 (2021). 4

[16] I. A. Snellen, B. R. Brandl, R. J. De Kok, M. Brogi, J. Birkby, and H. Schwarz. *Fast spin of the young extrasolar planet β pictoris b.* Nature **509**(7498), 63 (2014). 4

[17] J. W. Xuan, M. L. Bryan, H. A. Knutson, B. P. Bowler, C. V. Morley, and B. Benneke. *A rotation rate for the planetary-mass companion dh tau b.* The Astronomical Journal **159**(3), 97 (2020). 4

[18] M. L. Bryan, S. Ginzburg, E. Chiang, C. Morley, B. P. Bowler, J. W. Xuan, and H. A. Knutson. *As the worlds turn: constraining spin evolution in the planetary-mass regime.* The Astrophysical Journal **905**(1), 37 (2020). 4

[19] I. Crossfield, B. Biller, J. Schlieder, N. Deacon, M. Bonnefoy, D. Homeier, F. Allard, E. Buenzli, T. Henning, W. Brandner, *et al. A global cloud map of the nearest known brown dwarf.* Nature **505**(7485), 654 (2014). 4

[20] D. Defrère, O. Absil, J.-P. Berger, T. Boulet, W. Danchi, S. Ertel, A. Gallenne, F. Hénault, P. Hinz, E. Huby, *et al. The path towards high-contrast imaging with the vlti: the hi-5 project.* Experimental Astronomy **46**, 475 (2018). 4, 6, 14, 24, 31, 73

[21] S. Itoh and T. Matsuo. *A coronagraph with a sub-λ/d inner working angle and a moderate spectral bandwidth.* The Astronomical Journal **163**(6), 279 (2022). 4

[22] *Very large telescope interferometer (vlti) - european southern observetory* (2024). URL https://exoplanetarchive.ipac.caltech.edu/index.html. 5

[23] B. I. Vasil'ev and O. Mannoun. *Ir differential-absorption lidars for ecological monitoring of the environment.* Quantum Electronics **36**(9), 801 (2006). 5

[24] A. Matter, B. Lopez, P. Antonelli, M. Lehmitz, F. Bettonvil, U. Beckmann, S. Lagarde, W. Jaffe, R. Petrov, P. Berio, *et al. An overview of the mid-infrared spectro-interferometer matisse: science, concept, and current status.* Optical and Infrared Interferometry and Imaging V **9907**, 45 (2016). 5

[25] S. Gillessen, F. Eisenhauer, G. Perrin, W. Brandner, C. Straubmeier, K. Perraut, A. Amorim, M. Schöller, C. Araujo-Hauck, H. Bartko, *et al. Gravity: a four telescope beam combiner instrument for the vlti.* In *Optical and Infrared Interferometry II*, vol. 7734, pp. 318–337 (SPIE, 2010). 5

[26] J.-B. Le Bouquin, J.-P. Berger, B. Lazareff, G. Zins, P. Haguenauer, L. Jocou, P. Kern, R. Millan-Gabet, W. Traub, O. Absil, *et al. Pionier: a 4-telescope visitor instrument at vlti.* Astronomy & Astrophysics **535**, A67 (2011). 5, 15

[27] A. Mérand. *The vlti roadmap.* The Messenger **171**, 12 (2018). 5, 6

[28] F. Eisenhauer, J. D. Monnier, and O. Pfuhl. *Advances in optical/infrared interferometry.* Annual Review of Astronomy and Astrophysics **61** (2023). 6, 31

[29] E. Aller-Carpentier, R. Dorn, F. Delplancke-Stroebele, J. Paufique, L. Andolfato, C. Dupuy, E. Fedrigo, P. Gitton, P. Jolley, P. Lilley, *et al. Naomi: a new adaptive optics module for interferometry.* In *Optical and Infrared Interferometry IV*, vol. 9146, pp. 405–413 (SPIE, 2014). 7

[30] B. Mennesson, C. Hanot, E. Serabyn, K. Liewer, S. Martin, and D. Mawet. *High-contrast stellar observations within the diffraction limit at the palomar hale telescope.* The Astrophysical Journal **743**(2), 178 (2011). 7, 24

[31] S. Lacour, P. Tuthill, J. Monnier, T. Kotani, L. Gauchet, and P. Labeye. *A new interferometer architecture combining nulling with phase closure measurements.* Monthly Notices of the Royal Astronomical Society **439**(4), 4018 (2014). 7, 25, 130

[32] A. Arriola, S. Mukherjee, D. Choudhury, L. Labadie, and R. R. Thomson. *Ultrafast laser inscription of mid-ir directional couplers for stellar interferometry.* Optics Letters **39**(16), 4820 (2014). 7

[33] D. Defrère, A. Bigioli, C. Dandumont, G. Garreau, R. Laugier, M.-A. Martinod, O. Absil, J.-P. Berger, E. Bouzerand, B. Courtney-Barrer, *et al. L-band nulling interferometry at the vlti with asgard/hi-5: status and plans.* In *Optical and Infrared Interferometry and Imaging VIII*, vol. 12183, pp. 184–199 (SPIE, 2022). 7, 9, 12, 14, 15, 16, 64, 73, 138, 143

[34] M.-A. Martinod, D. Defrère, M. Ireland, S. Kraus, F. Martinache, P. Tuthill, A. Bigioli, E. Bouzerand, J. Bryant, S. Chhabra, *et al. High-angular resolution and high contrast observations from y to l band at the very large telescope interferometer with the asgard instrumental suite.* Journal of Astronomical Telescopes, Instruments, and Systems **9**(2), 025007 (2023). 7, 8, 9, 10, 12, 16, 63, 64, 143, 146

[35] A. Sanny, S. Gross, L. Labadie, D. Defrère, A. Bigioli, R. Laugier, C. Dandumont, and M. Withford. *Development of the 4-telescope photonic nuller of hi-5 for the characterization of exoplanets in the mid-ir.* In *Optical and Infrared Interferometry and Imaging VIII*, vol. 12183, pp. 425–434 (SPIE, 2022). 7, 16, 41, 62, 64, 65, 79, 98, 120, 143

[36] S. Kraus, D. Mortimer, S. Chhabra, Y. Lu, I. Codron, T. Gardner, N. Anugu, J. D. Monnier, J.-B. Le Bouquin, M. Ireland, *et al. High spectral-resolution interferometry down to 1 micron with asgard/bifrost at vlti: Science drivers and project overview.* In *Optical and Infrared Interferometry and Imaging VIII*, vol. 12183, pp. 631–649 (SPIE, 2022). 12, 13, 14

[37] *A measure of the size of the magnetospheric accretion region in tw hydrae.* Nature **584**(7822), 547 (2020). 13

[38] *Spatially resolved rotation of the broad-line region of a quasar at sub-parsec scale.* Nature **563**(7733), 657 (2018). 13

[39] E. Hone, S. Kraus, A. Kreplin, K.-H. Hofmann, G. Weigelt, T. Harries, and J. Kluska. *Gas dynamics in the inner few au around the herbig b [e] star mwc297-indications of a disk wind from kinematic modeling and velocity-resolved interferometric imaging.* Astronomy & Astrophysics **607**, A17 (2017). 13

[40] G. Weigelt, K.-H. Hofmann, D. Schertl, N. Clementel, M. Corcoran, A. Damineli, W.-J. de Wit, R. Grellmann, J. Groh, S. Guieu, *et al. Vlti-amber velocity-resolved aperture-synthesis imaging of η carinae with a spectral resolution of 12 000-studies of the primary star wind and innermost wind-wind collision zone.* Astronomy & Astrophysics **594**, A106 (2016). 13

[41] R. Abuter, M. Accardo, A. Amorim, N. Anugu, G. Avila, N. Azouaoui, M. Benisty, J.-P. Berger, N. Blind, H. Bonnet, *et al. First light for gravity: Phase referencing optical interferometry for the very large telescope interferometer.* Astronomy & Astrophysics **602**, A94 (2017). 13

[42] M. W. Broadley, D. V. Bekaert, L. Piani, E. Füri, and B. Marty. *Origin of life-forming volatile elements in the inner solar system.* Nature **611**(7935), 245 (2022). 13

[43] R. Laugier, D. Defrère, J. Woillez, B. Courtney-Barrer, F. A. Dannert, A. Matter, C. Dandumont, S. Gross, O. Absil, A. Bigioli, *et al. Asgard/nott: L-band nulling interferometry at the vlti-i. simulating the expected high-contrast performance.* Astronomy & Astrophysics **671**, A110 (2023). 14, 16, 130, 141

[44] L. Labadie. *A report on the status of astrophotonics for interferometry and beyond.* In *Optical and Infrared Interferometry and Imaging VIII*, vol. 12183, pp. 372–389 (SPIE, 2022). 14, 140

[45] F. Martinache and M. J. Ireland. *Kernel-nulling for a robust direct interferometric detection of extrasolar planets.* Astronomy & Astrophysics **619**, A87 (2018). 14, 25, 130

[46] A. Wallace, M. Ireland, and C. Federrath. *Constraints on planets in nearby young moving groups detectable by high-contrast imaging and gaia astrometry.* Monthly Notices of the Royal Astronomical Society **508**(2), 2515 (2021). 14

[47] P. Padovani and M. Cirasuolo. *The extremely large telescope.* Contemporary Physics pp. 1–18 (2023). 14

[48] A. Wallace and M. Ireland. *The likelihood of detecting young giant planets with high-contrast imaging and interferometry.* Monthly Notices of the Royal Astronomical Society **490**(1), 502 (2019). 14

[49] C. Dandumont, R. Laugier, A. Emsenhuber, J. Gagne, O. Absil, A. Bigioli, M. Bonavita, G. Garreau, M. Ireland, M.-A. Martinod, *et al. Vlti/hi-5: detection yield predictions for young giant exoplanets.* In *Optical and Infrared Interferometry and Imaging VIII*, vol. 12183, pp. 779–793 (SPIE, 2022). 14

[50] R. Laugier, D. Defrère, A. Matter, S. Gross, B. Courtney-Barrer, F. Dannert, J. Woillez, O. Absil, and C. Dandumont. *The expected performance of nulling at the vlti down to 5 mas.* In *Proceedings of SPIE: The International Society for Optical Engineering*, vol. 12183 (International Society for Optical Engineering, Bellingham, United States . . . , 2022). 14, 141

[51] N. van der Marel, J. P. Williams, M. Ansdell, C. F. Manara, A. Miotello, M. Tazzari, L. Testi, M. Hogerheijde, S. Bruderer, S. E. van Terwisga, *et al. New insights into the nature of transition disks from a complete disk survey of the lupus star-forming region.* The Astrophysical Journal **854**(2), 177 (2018). 14

[52] N. Van der Marel, T. Birnstiel, A. Garufi, E. Ragusa, V. Christiaens, D. J. Price, S. Sallum, D. Muley, L. Francis, and R. Dong. *On the diversity of asymmetries in gapped protoplanetary disks.* The Astronomical Journal **161**(1), 33 (2020). 14

[53] B. J. Norfolk, S. T. Maddison, C. Pinte, N. Van Der Marel, R. A. Booth, L. Francis, J.-F. Gonzalez, F. Ménard, C. M. Wright, G. Van Der Plas, *et al. Dust traps and the formation of cavities in transition discs: a millimetre to sub-millimetre*

comparison survey. Monthly Notices of the Royal Astronomical Society **502**(4), 5779 (2021). 14

[54] J.-L. Beuzit, M. Feldt, K. Dohlen, D. Mouillet, P. Puget, F. Wildi, L. Abe, J. Antichi, A. Baruffolo, P. Baudoz, *et al. Sphere: a planet finder instrument for the vlt*. In *Ground-based and airborne instrumentation for astronomy II*, vol. 7014, pp. 476–487 (SPIE, 2008). 15

[55] Q. Kral, A. V. Krivov, D. Defrère, R. van Lieshout, A. Bonsor, J.-C. Augereau, P. Thébault, S. Ertel, J. Lebreton, and O. Absil. *Exozodiacal clouds: hot and warm dust around main sequence stars*. Astronomical Review **13**(2), 69 (2017). 15

[56] A. Bonsor, M. C. Wyatt, Q. Kral, G. Kennedy, A. Shannon, and S. Ertel. *Using warm dust to constrain unseen planets*. Monthly Notices of the Royal Astronomical Society **480**(4), 5560 (2018). 15

[57] V. Faramaz, S. Ertel, M. Booth, J. Cuadra, and C. Simmonds. *Inner mean-motion resonances with eccentric planets: a possible origin for exozodiacal dust clouds*. Monthly Notices of the Royal Astronomical Society p. stw2846 (2016). 15

[58] J. K. Rigley and M. C. Wyatt. *Dust size and spatial distributions in debris discs: predictions for exozodiacal dust dragged in from an exo-kuiper belt*. Monthly Notices of the Royal Astronomical Society **497**(1), 1143 (2020). 15

[59] D. Defrère, P. Hinz, G. M. Kennedy, J. Stone, J. Rigley, S. Ertel, A. Gaspar, V. Bailey, W. Hoffmann, B. Mennesson, *et al. The hosts survey: Evidence for an extended dust disk and constraints on the presence of giant planets in the habitable zone of β leo*. The Astronomical Journal **161**(4), 186 (2021). 15

[60] D. Defrère, C. Stark, K. Cahoy, and I. Beerer. *Direct imaging of exoearths embedded in clumpy debris disks*. In *Space Telescopes and Instrumentation 2012: Optical, Infrared, and Millimeter Wave*, vol. 8442, pp. 267–274 (SPIE, 2012). 15

[61] S. Ertel, D. Defrère, P. Hinz, B. Mennesson, G. M. Kennedy, W. C. Danchi, C. Gelino, J. M. Hill, W. F. Hoffmann, J. Mazoyer, *et al. The hosts survey for exozodiacal dust: observational results from the complete survey.* The Astronomical Journal **159**(4), 177 (2020). 15

[62] S. Ertel, O. Absil, D. Defrere, J.-B. Le Bouquin, J.-C. Augereau, L. Marion, N. Blind, A. Bonsor, G. Bryden, J. Lebreton, *et al. A near-infrared interferometric survey of debris-disk stars-iv. an unbiased sample of 92 southern stars observed in h band with vlti/pionier.* Astronomy & Astrophysics **570**, A128 (2014). 15

[63] N. Scott, R. Millan-Gabet, E. Lhomé, T. Ten Brummelaar, V. Coudé Du Foresto, J. Sturmann, and L. Sturmann. *Jouvence of fluor: upgrades of a fiber beam combiner at the chara array.* Journal of Astronomical Instrumentation **2**(02), 1340005 (2013). 15

[64] F. Kirchschlager, S. Ertel, S. Wolf, A. Matter, and A. V. Krivov. *First l band detection of hot exozodiacal dust with vlti/matisse.* Monthly Notices of the Royal Astronomical Society: Letters **499**(1), L47 (2020). 15

[65] G. Garreau, A. Bigioli, R. Laugier, G. Raskin, J. Morren, J.-P. Berger, C. Dandumont, H.-D. K. Goldsmith, S. Gross, M. Ireland, *et al. Asgard/nott: L-band nulling interferometry at the vlti. ii. warm optical design and injection system.* Journal of Astronomical Telescopes, Instruments, and Systems **10**(1), 015002 (2024). 16, 63, 64, 143

[66] M. Shao and M. Colavita. *Long-baseline optical and infrared stellar interferometry.* Annual Review of Astronomy and Astrophysics **30**(1), 457 (1992). 19

[67] A. R. Thompson, J. M. Moran, and G. W. Swenson. *Interferometry and synthesis in radio astronomy* (Springer Nature, 2017). 19

[68] D. F. Buscher. *Practical optical interferometry.* 11 (Cambridge University Press, 2015). 19

[69] A. Quirrenbach. *Interferometric imaging from space.* In *Observing Photons in Space: A Guide to Experimental Space Astronomy*, pp. 313–332 (Springer, 2013). 19

[70] A. Glindemann. *Principles of stellar interferometry* (Springer Science & Business Media, 2011). 19

[71] J. D. Monnier. *Optical interferometry in astronomy.* Reports on Progress in Physics **66**(5), 789 (2003). 19

[72] A. Quirrenbach. *Optical interferometry.* Annual Review of Astronomy and Astrophysics **39**(1), 353 (2001). 19

[73] M. J. Reid and M. Honma. *Microarcsecond radio astrometry.* Annual Review of Astronomy and Astrophysics **52**, 339 (2014). 20

[74] R. N. Bracewell. *Detecting nonsolar planets by spinning infrared interferometer.* Nature **274**(5673), 780 (1978). 21, 49, 61

[75] O. Wallner, K. Ergenzinger, R. Flatscher, and U. Johann. *Darwin mission and configuration trade-off.* In *Advances in Stellar Interferometry*, vol. 6268, pp. 695–705 (SPIE, 2006). 21, 23

[76] M.-A. Martinod, B. Norris, P. Tuthill, T. Lagadec, N. Jovanovic, N. Cvetojevic, S. Gross, A. Arriola, T. Gretzinger, M. J. Withford, *et al. Scalable photonic-based nulling interferometry with the dispersed multi-baseline glint instrument.* Nature communications **12**(1), 2465 (2021). 21, 89, 140

[77] J. T. Hansen. *Towards Optical & Infrared Interferometry From Space.* Ph.D. thesis, The Australian National University (Australia) (2023). 23

[78] A. Léger, J.-M. Mariotti, B. Mennesson, M. Ollivier, J. Puget, D. Rouan, and J. Schneider. *Could we search for primitive life on extrasolar planets in the near future?* Icarus **123**(2), 249 (1996). 23

[79] J. Angel and N. Woolf. *An imaging nulling interferometer to study extrasolar planets*. The astrophysical journal **475**(1), 373 (1997). 23, 25, 124, 125, 130

[80] E. Serabyn. *Nulling interferometry: symmetry requirements and experimental results*. In *Interferometry in optical astronomy*, vol. 4006, pp. 328–339 (SPIE, 2000). 24

[81] P. M. Hinz, J. R. P. Angel, W. F. Hoffmann, D. W. McCarthy Jr, P. C. McGuire, M. Cheselka, J. L. Hora, and N. J. Woolf. *Imaging circumstellar environments with a nulling interferometer*. Nature **395**(6699), 251 (1998). 24

[82] E. Serabyn, B. Mennesson, M. Colavita, C. Koresko, and M. Kuchner. *The keck interferometer nuller*. The Astrophysical Journal **748**(1), 55 (2012). 24, 130

[83] P. Hinz, D. Defrere, A. Skemer, V. Bailey, J. Stone, E. Spalding, A. Vaz, E. Pinna, A. Puglisi, S. Esposito, *et al. Overview of lbti: a multipurpose facility for high spatial resolution observations*. In *Optical and Infrared Interferometry and Imaging V*, vol. 9907, pp. 8–21 (SPIE, 2016). 24

[84] B. Norris, N. Cvetojevic, S. Gross, N. Jovanovic, P. N. Stewart, N. Charles, J. S. Lawrence, M. J. Withford, and P. Tuthill. *High-performance 3d waveguide architecture for astronomical pupil-remapping interferometry*. Optics express **22**(15), 18335 (2014). 24

[85] B. Mennesson, R. Millan-Gabet, E. Serabyn, M. Colavita, O. Absil, G. Bryden, M. Wyatt, W. Danchi, D. Defrere, O. Doré, *et al. Constraining the exozodiacal luminosity function of main-sequence stars: complete results from the keck nuller mid-infrared surveys*. The Astrophysical Journal **797**(2), 119 (2014). 24

[86] S. Ertel, D. Defrere, P. Hinz, B. Mennesson, G. M. Kennedy, W. Danchi, C. Gelino, J. Hill, W. Hoffmann, G. Rieke, *et al. The hosts survey—exozodiacal dust measurements for 30 stars*. The Astronomical Journal **155**(5), 194 (2018). 24

[87] C. Hanot, B. Mennesson, S. Martin, K. Liewer, F. Loya, D. Mawet, P. Riaud, O. Absil, and E. Serabyn. *Improving interferometric null depth measurements using statistical distributions: theory and first results with the palomar fiber nuller.* The Astrophysical Journal **729**(2), 110 (2011). 24

[88] E. Serabyn, B. Mennesson, S. Martin, K. Liewer, and J. Kühn. *Nulling at short wavelengths: theoretical performance constraints and a demonstration of faint companion detection inside the diffraction limit with a rotating-baseline interferometer.* Monthly Notices of the Royal Astronomical Society **489**(1), 1291 (2019). 24, 110, 111

[89] J. Kühn, B. Mennesson, K. Liewer, S. Martin, F. Loya, R. Millan-Gabet, and E. Serabyn. *Exploring intermediate (5–40 au) scales around ab aurigae with the palomar fiber nuller.* The Astrophysical Journal **800**(1), 55 (2015). 24

[90] T. Lagadec, B. Norris, S. Gross, A. Arriola, T. Gretzinger, N. Cvetojevic, M.-A. Martinod, N. Jovanovic, M. Withford, and P. Tuthill. *The glint south testbed for nulling interferometry with photonics: Design and on-sky results at the anglo-australian telescope.* Publications of the Astronomical Society of Australia **38**, e036 (2021). 24, 74, 89, 107

[91] T. Lagadec, B. Norris, S. Gross, A. Arriola, T. Gretzinger, N. Cvetojevic, J. Lawrence, M. Withford, and P. Tuthill. *Glint south: a photonic nulling interferometer pathfinder at the anglo-australian telescope for high contrast imaging of substellar companions.* In *Optical and Infrared Interferometry and Imaging VI*, vol. 10701, pp. 238–245 (SPIE, 2018). 25, 122

[92] B. R. Norris, N. Cvetojevic, T. Lagadec, N. Jovanovic, S. Gross, A. Arriola, T. Gretzinger, M.-A. Martinod, O. Guyon, J. Lozi, *et al. First on-sky demonstration of an integrated-photonic nulling interferometer: the glint instrument.* Monthly Notices of the Royal Astronomical Society **491**(3), 4180 (2020). 25

[93] R. Laugier, N. Cvetojevic, and F. Martinache. *Kernel nullers for an arbitrary number of apertures.* Astronomy & Astrophysics **642**, A202 (2020). 25

[94] S. Martin, G. Serabyn, K. Liewer, and B. Mennesson. *Achromatic broadband nulling using a phase grating.* Optica **4**(1), 110 (2017). 25

[95] F. Hénault and A. Spang. *Cheapest nuller in the world: crossed beamsplitter cubes.* In *Optical and Infrared Interferometry IV*, vol. 9146, pp. 21–32 (SPIE, 2014). 25

[96] M. A. Butt. *Integrated optics: Platforms and fabrication methods.* Encyclopedia **3**(3), 824 (2023). 26

[97] S. Gross and M. Withford. *Ultrafast-laser-inscribed 3d integrated photonics: challenges and emerging applications.* Nanophotonics **4**(3), 332 (2015). 26, 27, 31, 73, 74

[98] R. Stoian. *Volume photoinscription of glasses: three-dimensional micro-and nanostructuring with ultrashort laser pulses.* Applied Physics A **126**, 1 (2020). 28

[99] L. V. Keldysh *et al. Diagram technique for nonequilibrium processes.* Sov. Phys. JETP **20**(4), 1018 (1965). 28

[100] K. Itoh, W. Watanabe, S. Nolte, and C. B. Schaffer. *Ultrafast processes for bulk modification of transparent materials.* MRS bulletin **31**(8), 620 (2006). 29, 30

[101] P. Dekker, M. Ams, G. Marshall, D. Little, and M. Withford. *Annealing dynamics of waveguide bragg gratings: evidence of femtosecond laser induced colour centres.* Optics express **18**(4), 3274 (2010). 29

[102] C. Hnatovsky, R. Taylor, P. Rajeev, E. Simova, V. Bhardwaj, D. Rayner, and P. Corkum. *Pulse duration dependence of femtosecond-laser-fabricated nanogratings in fused silica.* Applied Physics Letters **87**(1) (2005). 29

[103] D. Simanovskii, H. Schwettman, H. Lee, and A. Welch. *Midinfrared optical breakdown in transparent dielectrics.* Physical review letters **91**(10), 107601 (2003). 29

[104] M. Beresna, M. Gecevičius, and P. G. Kazansky. *Ultrafast laser direct writing and nanostructuring in transparent materials.* Advances in Optics and Photonics **6**(3), 293 (2014). 30

[105] Y. Shimotsuma, P. G. Kazansky, J. Qiu, and K. Hirao. *Self-organized nanogratings in glass irradiated by ultrashort light pulses.* Physical review letters **91**(24), 247405 (2003). 30

[106] E. Glezer, M. Milosavljevic, L. Huang, R. Finlay, T.-H. Her, J. P. Callan, and E. Mazur. *Three-dimensional optical storage inside transparent materials.* Optics letters **21**(24), 2023 (1996). 30

[107] R. R. Gattass, L. R. Cerami, and E. Mazur. *Micromachining of bulk glass with bursts of femtosecond laser pulses at variable repetition rates.* Optics Express **14**(12), 5279 (2006). 30

[108] S. M. Eaton, H. Zhang, P. R. Herman, F. Yoshino, L. Shah, J. Bovatsek, and A. Y. Arai. *Heat accumulation effects in femtosecond laser-written waveguides with variable repetition rate.* Optics express **13**(12), 4708 (2005). 31

[109] L. Li, W. Kong, and F. Chen. *Femtosecond laser-inscribed optical waveguides in dielectric crystals: a concise review and recent advances.* Advanced Photonics **4**(2), 024002 (2022). 31

[110] R. Osellame, G. Cerullo, and R. Ramponi. *Femtosecond laser micromachining: photonic and microfluidic devices in transparent materials*, vol. 123 (Springer, 2012). 31

[111] R. R. Gattass and E. Mazur. *Femtosecond laser micromachining in transparent materials.* Nature photonics **2**(4), 219 (2008). 31

[112] H. Lin, Z. Luo, T. Gu, L. C. Kimerling, K. Wada, A. Agarwal, and J. Hu. *Mid-infrared integrated photonics on silicon: a perspective.* Nanophotonics **7**(2), 393 (2017). 31, 67

[113] G. E. Madden, D. Choudhury, W. N. MacPherson, and R. R. Thomson. *Development of low-loss mid-infrared ultrafast laser inscribed waveguides.* Optical Engineering **56**(7), 075102 (2017). 31, 67

[114] W. Blanc, Y. G. Choi, X. Zhang, M. Nalin, K. A. Richardson, G. C. Righini, M. Ferrari, A. Jha, J. Massera, S. Jiang, *et al. The past, present and future of photonic glasses: A review in homage to the united nations international year of glass 2022.* Progress in Materials Science p. 101084 (2023). 32

[115] M. Khalid, G. Y. Chen, H. Ebendorff-Heidepreim, and D. G. Lancaster. *Femtosecond laser induced low propagation loss waveguides in a lead-germanate glass for efficient lasing in near to mid-ir.* Scientific reports **11**(1), 10742 (2021). 31

[116] J.-P. Bérubé, A. Le Camus, S. H. Messaddeq, Y. Petit, Y. Messaddeq, L. Canioni, and R. Vallée. *Femtosecond laser direct inscription of mid-ir transmitting waveguides in bgg glasses.* Optical Materials Express **7**(9), 3124 (2017). 31

[117] M. Smayev, V. Dorofeev, A. Moiseev, and A. Okhrimchuk. *Femtosecond laser writing of a depressed cladding single mode channel waveguide in high-purity tellurite glass.* Journal of Non-Crystalline Solids **480**, 100 (2018). 31

[118] A. Ródenas, G. Martin, B. Arezki, N. Psaila, G. Jose, A. Jha, L. Labadie, P. Kern, A. Kar, and R. Thomson. *Three-dimensional mid-infrared photonic circuits in chalcogenide glass.* Optics Letters **37**(3), 392 (2012). 31, 50

[119] A. Arriola, S. Gross, M. Ams, T. Gretzinger, D. Le Coq, R. Wang, H. Ebendorff-Heidepriem, J. Sanghera, S. Bayya, L. Shaw, *et al. Mid-infrared astrophotonics: study of ultrafast laser induced index change in compatible materials.* Optical Materials Express **7**(3), 698 (2017). 31, 50

[120] S. Gross, N. Jovanovic, A. Sharp, M. Ireland, J. Lawrence, and M. J. Withford. *Low loss mid-infrared zblan waveguides for future astronomical applications.* Optics Express **23**(6), 7946 (2015). 32, 49

[121] A.-M. Loireau-Lozac'h, M. Guittard, and J. Flahaut. *Verres formes par les sulfures l2s3 des terres rares avec le sulfure de gallium ga2s3.* Materials Research Bulletin **11**(12), 1489 (1976). 32

[122] S. Gross. *Direct-write mid-IR waveguide lasers.* Ph.D. thesis (2012). 35, 50

[123] T. Gretzinger. *Integrated photonics for mid-infrared stellar interferometry.* Ph.D. thesis, Macquarie University (2022). 35, 36, 47, 60, 69, 103, 142

[124] R. Wayne. *Chapter 9 - Differential Interference Contrast (DIC) Microscopy* (Academic Press, San Diego, 2014), second edition ed. URL https://www.sciencedirect.com/science/article/pii/B9780124114845000093. 37

[125] G. Thériault. *The beginner's guide on spot size of laser beam* (2024). URL https://www.gentec-eo.com/blog/spot-size-of-laser-beam. 40

[126] J. Tepper, R. Diener, L. Labadie, S. Minardi, S. Gross, A. Arriola, M. Withford, and S. Nolte. *Photonics-based mid-infrared interferometry: the challenges of polychromatic operation and comparative performances.* In *Optical and Infrared Interferometry and Imaging VI*, vol. 10701, pp. 351–361 (SPIE, 2018). 41

[127] J. W. Cooley and J. W. Tukey. *An algorithm for the machine calculation of complex fourier series.* Mathematics of computation **19**(90), 297 (1965). 45

[128] D. Hillerkuss, M. Winter, M. Teschke, A. Marculescu, J. Li, G. Sigurdsson, K. Worms, S. B. Ezra, N. Narkiss, W. Freude, *et al. Simple all-optical fft scheme enabling tbit/s real-time signal processing.* Optics express **18**(9), 9324 (2010). 45

[129] V. Coudé du Foresto, G. Perrin, and M. Boccas. *Minimization of fiber dispersion effects in double fourier stellar interferometers.* Astronomy and Astrophysics, Vol. 293, p. 278-286 (1995) **293**, 278 (1995). 46

[130] J. Tepper. *Towards high-resolution and high-contrast imaging in mid-infrared astronomy: Integrated optics beam combiners for astrointerferometry.* Ph.D. thesis, Universität zu Köln (2017). 47, 126

[131] R. Osgood Jr and X. Meng. *Principles of Photonic Integrated Circuits* (Springer, 2021). 48, 60, 74

[132] R. He, I. Hernández-Palmero, C. Romero, J. R. V. de Aldana, and F. Chen. *Three-dimensional dielectric crystalline waveguide beam splitters in mid-infrared band by direct femtosecond laser writing.* Optics express **22**(25), 31293 (2014). 49, 74

[133] H.-D. Nguyen, A. Ródenas, J. R. V. de Aldana, G. Martín, J. Martínez, M. Aguiló, M. C. Pujol, and F. Díaz. *Low-loss 3d-laser-written mid-infrared linbo 3 depressed-index cladding waveguides for both te and tm polarizations.* Optics Express **25**(4), 3722 (2017). 49

[134] D. W. Hewak, D. Brady, R. J. Curry, G. Elliott, C.-C. Huang, M. Hughes, K. Knight, A. Mairaj, M. Petrovich, R. Simpson, *et al. Chalcogenide glasses for photonics device applications* (2010). 49

[135] J. Burghoff, C. Grebing, S. Nolte, and A. Tünnermann. *Efficient frequency doubling in femtosecond laser-written waveguides in lithium niobate.* Applied physics letters **89**(8), 081108 (2006). 49

[136] J. L. Archambault, L. Reekie, and P. S. J. Russell. *100% reflectivity bragg reflectors produced in optical fibres by single excimer laser pulses.* Electronics Letters **29**(5), 453 (1993). 49

[137] C. D'Amico, C. Caillaud, P. K. Velpula, M. Bhuyan, M. Somayaji, J.-P. Colombier, J. Troles, L. Calvez, V. Nazabal, A. Boukenter, *et al. Ultrafast laser-induced refractive index changes in ge 15 as 15 s 70 chalcogenide glass.* Optical Materials Express **6**(6), 1914 (2016). 49

[138] S. Gross, M. Dubov, and M. J. Withford. *On the use of the type i and ii scheme for classifying ultrafast laser direct-write photonics.* Optics express **23**(6), 7767 (2015). 49

[139] T. Gretzinger, S. Gross, M. Ams, A. Arriola, and M. J. Withford. *Ultrafast laser inscription in chalcogenide glass: thermal versus athermal fabrication.* Optical Materials Express **5**(12), 2862 (2015). 50, 51

[140] M. Hughes, W. Yang, and D. Hewak. *Fabrication and characterization of femtosecond laser written waveguides in chalcogenide glass.* Applied Physics Letters **90**(13) (2007). 50, 53

[141] J. E. McCarthy, H. T. Bookey, N. D. Psaila, R. R. Thomson, and A. K. Kar. *Mid-infrared spectral broadening in an ultrafast laser inscribed gallium lanthanum sulphide waveguide.* Optics express **20**(2), 1545 (2012). 50, 53

[142] C. B. Schaffer, J. F. García, and E. Mazur. *Bulk heating of transparent materials using a high-repetition-rate femtosecond laser.* Applied Physics A **76**, 351 (2003). 51

[143] M. Ams, G. Marshall, D. Spence, and M. Withford. *Slit beam shaping method for femtosecond laser direct-write fabrication of symmetric waveguides in bulk glasses.* Optics express **13**(15), 5676 (2005). 51

[144] P. Bado, A. Said, M. Dugan, T. Sosnowski, and S. Wright. *Dramatic improvements in waveguide manufacturing with femtosecond lasers.* NFOEC, Dallas (2002). 51

[145] J. Liu, Z. Zhang, C. Flueraru, X. Liu, S. Chang, and C. P. Grover. *Waveguide shaping and writing in fused silica using a femtosecond laser.* IEEE Journal of selected topics in quantum electronics **10**(1), 169 (2004). 51

[146] J. E. McCarthy, H. T. Bookey, N. D. Psaila, R. R. Thomson, and A. K. Kar. *Mid-infrared spectral broadening in an ultrafast laser inscribed gallium lanthanum sulphide waveguide.* Optics express **20**(2), 1545 (2012). 51

[147] D. Lee, R. R. Thomson, and C. R. Cunningham. *Performance of volume phase gratings manufactured using ultrafast laser inscription.* In *Modern Technologies*

in Space-and Ground-based Telescopes and Instrumentation II, vol. 8450, pp. 982–990 (SPIE, 2012). 51

[148] R. Diener, G. Tabacchi, S. Nolte, and S. Minardi. *Structural modification of gallium lanthanum sulfide glass induced by ultrafast laser inscription.* In *Laser-based Micro-and Nanoprocessing XI*, vol. 10092, pp. 60–65 (SPIE, 2017). 51, 102

[149] R. Diener. *Mid-infrared photonic devices for stellar interferometry.* Ph.D. thesis (2018). 51

[150] T. Gretzinger, S. Gross, A. Arriola, and M. J. Withford. *Towards a photonic mid-infrared nulling interferometer in chalcogenide glass.* Optics express **27**(6), 8626 (2019). 51, 59, 64, 69, 76, 95, 96, 102, 103, 143, 144

[151] T. Gretzinger, T. T. Fernandez, S. Gross, A. Arriola, and M. J. Withford. *Boson band mapping: revealing ultrafast laser induced structural modifications in chalcogenide glass.* Optics Letters **45**(13), 3369 (2020). 53, 83, 99

[152] K. L. Kruse and C. T. Middlebrook. *Fan-out routing and optical splitting techniques for compact optical interconnects using single-mode polymer waveguides.* Journal of Modern Optics **62**(sup2), S1 (2015). 57, 58

[153] P. Buchmann and A. Houghton. *Optical y-junctions and s-bends formed by preferentially etched single-mode rib waveguides in inp.* Electronics Letters **19**(18), 850 (1982). 57

[154] F. Mustieles, E. Ballesteros, and P. Baquero. *Theoretical s-bend profile for optimization of optical waveguide radiation losses.* IEEE Photonics Technology Letters **5**(5), 551 (1993). 59

[155] A. Kumar and S. Aditya. *Performance of s-bends for integrated-optic waveguides.* Microwave and Optical Technology Letters **19**(4), 289 (1998). 59

[156] S. Ridgway and J.-M. Mariotti. *Deriving object visibilities from interferograms obtained with a fiber stellar interferometer.* Astronomy and Astrophysics Supplement series **121**(2), 379 (1997). 61

[157] N. Cvetojevic, F. Martinache, P. Chingaipe, R. Laugier, K. Ławniczuk, R. G. Broeke, R. Ligi, M. N'Diaye, and D. Mary. *3-beam self-calibrated kernel nulling photonic interferometer.* arXiv preprint arXiv:2206.04977 (2022). 62, 123, 130, 141

[158] M. Toyoshima, T. Jono, K. Nakagawa, and A. Yamamoto. *Optimum divergence angle of a gaussian beam wave in the presence of random jitter in free-space laser communication systems.* JOSA A **19**(3), 567 (2002). 66

[159] J. Tepper, L. Labadie, R. Diener, S. Minardi, J.-U. Pott, R. Thomson, and S. Nolte. *Integrated optics prototype beam combiner for long baseline interferometry in the l and m bands.* Astronomy & Astrophysics **602**, A66 (2017). 66, 115, 144, 150

[160] S. O. Kasap. *Optoelectronics and photonics: principles and practices. 2nd* (Pearson, 2012). 67, 76, 91, 108

[161] L. Labadie, J.-P. Berger, N. Cvetojevic, R. Haynes, R. Harris, N. Jovanovic, S. Lacour, G. Martin, S. Minardi, G. Perrin, *et al. Astronomical photonics in the context of infrared interferometry and high-resolution spectroscopy.* In *Optical and Infrared Interferometry and Imaging V*, vol. 9907, pp. 322–342 (SPIE, 2016). 67

[162] M. Kuznetsov. *Radiation loss in dielectric waveguide y-branch structures.* Journal of lightwave technology **3**(3), 674 (1985). 67

[163] A. Myerson. *Handbook of industrial crystallization* (Butterworth-Heinemann, 2002). 70, 71

[164] C. N. Nanev. *Theory of nucleation.* In *Handbook of Crystal Growth*, pp. 315–358 (Elsevier, 2015). 71

[165] D. Kashchiev and G. Van Rosmalen. *Nucleation in solutions revisited.* Crystal Research and Technology: Journal of Experimental and Industrial Crystallography **38**(7-8), 555 (2003). 71

[166] E. V. Khamskiĭ and A. Tybulewicz. *Crystallization from solutions* (1969). 71

[167] R. Li and A. B. Seddon. *Gallium–lanthanum–sulphide glasses: a review of recent crystallisation studies.* Journal of non-crystalline solids **256**, 17 (1999). 71

[168] J. D. Love and N. Riesen. *Single-, few-, and multimode y-junctions.* Journal of Lightwave technology **30**(3), 304 (2011). 73, 74

[169] R. Stoian and J. Bonse. *Ultrafast laser nanostructuring: the pursuit of extreme scales*, vol. 239 (Springer Nature, 2023). 73

[170] D. Homoelle, S. Wielandy, A. L. Gaeta, N. Borrelli, and C. Smith. *Infrared photosensitivity in silica glasses exposed to femtosecond laser pulses.* Optics Letters **24**(18), 1311 (1999). 74

[171] J. Lv, Y. Cheng, W. Yuan, X. Hao, and F. Chen. *Three-dimensional femtosecond laser fabrication of waveguide beam splitters in linbo 3 crystal.* Optical Materials Express **5**(6), 1274 (2015). 74

[172] Y. Ren, L. Zhang, H. Xing, C. Romero, J. R. V. de Aldana, and F. Chen. *Cladding waveguide splitters fabricated by femtosecond laser inscription in ti: Sapphire crystal.* Optics & Laser Technology **103**, 82 (2018). 75

[173] C. Doerr, M. Cappuzzo, E. Chen, A. Wong-Foy, L. Gomez, A. Griffin, and L. Buhl. *Bending of a planar lightwave circuit 2/spl times/2 coupler to desensitize it to wavelength, polarization, and fabrication changes.* IEEE photonics technology letters **17**(6), 1211 (2005). 75

[174] M. Izutsu, Y. Nakai, and T. Sueta. *Operation mechanism of the single-mode optical-waveguide y junction.* Optics letters **7**(3), 136 (1982). 75

[175] K. Færch and M. Svalgaard. *Symmetrical waveguide devices fabricated by direct uv writing.* IEEE Photonics Technology Letters **14**(2), 173 (2002). 76

[176] A. Benoît, F. A. Pike, T. K. Sharma, D. G. MacLachlan, A. N. Dinkelaker, A. S. Nayak, K. Madhav, M. M. Roth, L. Labadie, E. Pedretti, *et al. Ultrafast laser inscription of asymmetric integrated waveguide 3 db couplers for astronomical k-band interferometry at the chara array.* JOSA B **38**(9), 2455 (2021). 89

[177] R. Errmann, S. Minardi, L. Labadie, B. Muthusubramanian, F. Dreisow, S. Nolte, and T. Pertsch. *Interferometric nulling of four channels with integrated optics.* Applied Optics **54**(24), 7449 (2015). 90

[178] A. W. Snyder, J. D. Love, *et al. Optical waveguide theory*, vol. 175 (Chapman and hall London, 1983). 90

[179] E. K. Sharma, J. P. N. Nath, and N. Dhingra. *Coupled mode theory and coupled mode photonic devices: A review.* Asian Journal of Physics **30**(5), 00 (2021). 90, 92

[180] R. Diener, S. Nolte, T. Pertsch, and S. Minardi. *Effects of stress on neighboring laser written waveguides in gallium lanthanum sulfide.* Applied Physics Letters **112**(11) (2018). 91, 93

[181] W.-J. Chen, S. M. Eaton, H. Zhang, and P. R. Herman. *Broadband directional couplers fabricated in bulk glass with high repetition rate femtosecond laser pulses.* Optics Express **16**(15), 11470 (2008). 93, 95

[182] K. Jinguji, N. Takato, A. Sugita, and M. Kawachi. *Mach-zehnder interferometer type optical waveguide coupler with wavelength-flattened coupling ratio.* Electronics Letters **17**(26), 1326 (1990). 94

[183] L. Pierre, S. I. Najafi, *et al. New method to design directional coupler dual wavelength multi/demultiplexer with bends at both extremities.* Optics communications **111**(1-2), 43 (1994). 94

[184] N. Takato, K. Jinguji, M. Yasu, H. Toba, and M. Kawachi. *Silica-based single-mode waveguides on silicon and their application to guided-wave optical interferometers.* Journal of lightwave technology **6**(6), 1003 (1988). 94

[185] M. Olivero and M. Svalgaard. *Direct uv-written broadband directional planar waveguide couplers.* Optics Express **13**(21), 8390 (2005). 95

[186] J. Berger, P. Haguenauer, P. Kern, K. Perraut, F. Malbet, I. Schanen, M. Severi, R. Millan-Gabet, and W. Traub. *Integrated optics for astronomical interferometry-iv. first measurements of stars.* Astronomy & Astrophysics **376**(3), L31 (2001). 107

[187] E. Serabyn, J. Wallace, H. Nguyen, E. Schmidtlin, and G. Hardy. *Nulling interferometry: working on the dark fringe.* In *Working on the Fringe: Optical and IR Interferometry from Ground and Space*, vol. 194, p. 437 (1999). 110

[188] E. Serabyn. *Nulling interferometry.* In *The WSPC Handbook of Astronomical Instrumentation: Volume 3: UV, Optical & IR Instrumentation: Part 2*, pp. 71–89 (World Scientific, 2021). 110, 111

[189] J. LeBouquin, K. Rousselet-Perraut, P. Kern, F. Malbet, P. Haguenauer, P. Kervella, I. Schanen, J. Berger, A. Delboulbé, B. Arezki, *et al. First observations with an h-band integrated optics beam combiner at the vlti.* Astronomy & Astrophysics **424**(2), 719 (2004). 112

[190] I. Zorin, P. Gattinger, A. Ebner, and M. Brandstetter. *Advances in mid-infrared spectroscopy enabled by supercontinuum laser sources.* Optics Express **30**(4), 5222 (2022). 119

[191] N. Cvetojevic, F. Martinache, and S. Lacour. *20— kernel nulling self-calibration.* 2023 Astrophotonics Roadmap: pathways to realizing multi-functional integrated astrophotonic instruments **5**(4), 042501 (2023). 130

[192] T. Velusamy, R. P. Angel, A. Eatchel, D. Tenerelli, and N. Woolf. *Single and*

double bracewell nulling interferometer in space. In *Earths: DARWIN/TPF and the Search for Extrasolar Terrestrial Planets*, vol. 539, pp. 631–636 (2003). 130

[193] P. M. Chingaipe, F. Martinache, N. Cvetojevic, R. Ligi, D. Mary, M. N'Diaye, D. Defrère, and M. J. Ireland. *High-contrast detection of exoplanets with a kernel-nuller at the vlti.* arXiv preprint arXiv:2304.14193 (2023). 130

[194] P. M. Chingaipe, F. Martinache, and N. Cvetojevic. *4-input photonic kernel-nulling for the vlti.* In *Optical and Infrared Interferometry and Imaging VIII*, vol. 12183, pp. 448–457 (SPIE, 2022). 130

[195] L. Labadie, E. Le Coarer, R. Maurand, P. Labeye, P. Kern, B. Arezki, and J.-E. Broquin. *Mid-infrared laser light nulling experiment using single-mode conductive waveguides.* Astronomy & Astrophysics **471**(1), 355 (2007). 137

[196] N. Pogson. *Magnitudes of thirty-six of the minor planets for the first day of each month of the year 1857.* Monthly Notices of the Royal Astronomical Society, Vol. 17, p. 12-15 **17**, 12 (1856). 138

[197] V. Coudé du Foresto, G. Perrin, and M. Boccas. *Minimization of fiber dispersion effects in double fourier stellar interferometers.* Astronomy and Astrophysics, Vol. 293, p. 278-286 (1995) **293**, 278 (1995). 149

Declaration of contributions

I hereby declare that the work in this thesis was undertaken between Macquarie University, Australia and the University of Cologne, Germany, under a Cotutelle PhD agreement. Throughout my thesis, I focused on developing a functional 4-telescope beam combiner for the upcoming instrument ASGARD/NOTT. This instrument is going to be the first long-baseline self-calibrating nulling instrument at the VLTI (Paranal, Chile), operating in a mid-infrared astronomical band, utilising the ultrafast laser inscription (ULI) technique in gallium lanthanum sulphide (GLS) glass.

The fabrication process was conducted at Macquarie University, encompassing pre- and post-processing of the GLS glass material and femtosecond laser direct writing under the guidance of Dr Simon Gross. During my stay at Macquarie University, I underwent training in adopting the inscription technique, performing simulations for designing photonic components, particularly achromatic Y-junctions, using BeamProb of Rsoft, and identifying the required Y-junctions experimentally as a part of my original contribution. I also developed a characterisation bench from scratch to identify the mode-field profile of the fabricated waveguides at Macquarie University. The writing recipe employed for low-loss optical waveguides used from the PhD work of Dr Thomas Gretzinger, a former PhD student in my group at Macquarie University and my work can be seen as an extension of his preliminary investigation, maturing it for on-sky implementation.

Additionally, most of my efforts were dedicated to characterising the fabricated photonic components at the University of Cologne under the supervision of Professor

Dr Lucas Labadie. I was engaged in the development of 2-beam and 4-beam spectro-interferometric lab benches for extensive on-demand characterisation in collaboration with the ASGARD team led by Professor Dr Denis Defrère from KU Leuven, Belgium, to comprehend the chromaticity and other sensitivities of the photonic components and measure their performance for on-sky astronomy. The insights from these characterisations were used to drive upgrades to the fabrication process with interaction. Moreover, utilising these benches, I also developed and modified experimental approaches to examine 2-telescope and 4-telescope beam combination nulling interferometry of astrophotonic devices in the L' astronomical band as another part of my original work. Additionally,

This thesis is submitted in fulfilment of the requirements for the degree of Cotutelle Doctor of Philosophy in Physics at Macquarie University and the University of Cologne and has not been submitted for a higher degree to any other university or institution.

I certify that to the best of my knowledge, all sources used and assistance received in the preparation of this thesis have been acknowledged. This thesis does not contain any material which is defamatory of any person, form or corporation and is not in breach of copyright or breach of other rights which shall give rise to any action at Common Law or under Statute.

Declaration

Hiermit versichere ich an Eides statt, dass ich die vorliegende Dissertation selbstständig und ohne die Benutzung anderer als der angegebenen Hilfsmittel und Literatur angefertigt habe. Alle Stellen, die wörtlich oder sinngemäß aus veröffentlichten und nicht veröffentlichten Werken dem Wortlaut oder dem Sinn nach entnommen wurden, sind als solche kenntlich gemacht. Ich versichere an Eides statt, dass diese Dissertation noch keiner anderen Fakultät oder Universität zur Prüfung vorgelegen hat; dass sie - abgesehen von unten angegebenen Teilpublikationen und eingebundenen Artikeln und Manuskripten - noch nicht veröffentlicht worden ist sowie, dass ich eine Veröffentlichung der Dissertation vor Abschluss der Promotion nicht ohne Genehmigung des Promotionsausschusses vornehmen werde. Die Bestimmungen dieser Ordnung sind mir bekannt. Darüber hinaus erkläre ich hiermit, dass ich die Ordnung zur Sicherung guter wissenschaftlicher Praxis und zum Umgang mit wissenschaftlichem Fehlverhalten der Universität zu Köln gelesen und sie bei der Durchführung der Dissertation zugrundeliegenden Arbeiten und der schriftlich verfassten Dissertation beachtet habe und verpflichte mich hiermit, die dort genannten Vorgaben bei allen wissenschaftlichen Tätigkeiten zu beachten und umzusetzen. Ich versichere, dass die eingereichte elektronische Fassung der eingereichten Druckfassung vollständig entspricht.

List of Publications

- Germain Garreau, Azzurra Bigioli, Romain Laugier, Gert Raskin, Johan Morren, Jean-Philippe Berger, Colin Dandumont, Harry-Dean Kenchington Goldsmith, Simon Gross, Michael Ireland, Lucas Labadie, Jérôme Loicq, Stephen Madden, Guillermo Martin, Marc-Antoine Martinod, Alexandra Mazzoli, Ahmed Sanny, Hancheng Shao, Kunlun Yan, Denis Defrère *Asgard/NOTT: L-band nulling interferometry at the VLTI. II. Warm optical design and injection system.* Journal of Astronomical Telescopes, Instruments, and Systems **10(1)**, 015002-015002 (2024)

- Marc-Antoine Martinod, Denis Defrère, Michael J. Ireland, Stefan Kraus, Frantz Martinache, Peter G. Tuthill, Azzurra Bigioli, Emilie Bouzerand, Julia Bryant, Sorabh Chhabra, Benjamin Courtney-Barrer, Fred Crous, Nick Cvetojevic, Colin Dandumont, Steve Ertel, Tyler Gardner, Germain Garreau, Adrian M. Glauser, Lucas Labadie, Tiphaine Lagadec, Romain Laugier, Alexandra Mazzoli, Daniel J. Mortimer, Barnaby R. M. Norris, Gert Raskin, Gordon Robertson, Ahmed Sanny, Adam Taras *High-angular resolution and high contrast observations from Y to L band at the Very Large Telescope Interferometer with the Asgard Instrumental suite.* insert journal name **9(2)**, 025007 (2023)

- Romain Laugier, Denis Defrère, Julien Woillez, Benjamin Courtney-Barrer, Felix A. Dannert, Alexis Matter5, Colin Dandumont, Simon Gross, Olivier Absil, Azzurra Bigioli, Germain Garreau, Lucas Labadie, Jérôme Loicq, Marc-Antoine

Martinod, Alexandra Mazzoli, Gert Raskin and Ahmed Sanny *Asgard/NOTT: L-band nulling interferometry at the VLTI I. Simulating the expected high-contrast performance.* Astronomy Astrophysics, **671**, A110 (2023)

- Ahmed Sanny, Lucas Labadie, Simon Gross, Michael Withford, Romain Laugier, Marc-Antoine Martinod, Germain Garreau, Denis Defrère *Development status of the L'-band 4-telescope integrated optics nulling beam combiner for NOTT.* SPIE. Optical and Infrared Interferometry and Imaging IX **13095**, 13095-26 (2024)

- Ahmed Sanny, Simon Gross, Michael Withford, Denis Defrère Lucas Labadie *Towards the development of the self-calibrating nulling interferometry beam combiner for the VLTI instrument ASGARD to detect exoplanets.* The European Conference on Lasers and Electro-Optics (CLEO), Munich, Germany (2023)

- Ahmed Sanny, Lucas Labadie, Michael Withford, Simon Gross *Development of an mid-infrared integrated optics 4-telescope beam combiner for the Hi-5 instrument.* Australian and New Zealand Conference on Optics and Photonics (ANZCOP), Adelaide, Australia (2022)

- Ahmed Sanny, Simon Gross, Lucas Labadie, Denis Defrère, Azzurra Bigioli, Romain Laugier, Colin Dandumont, Michael Withford *Development of the four-telescope photonic nuller of Hi-5 for the characterization of exoplanets in the mid-IR.* Proc. SPIE 12183, Optical and Infrared Interferometry and Imaging VIII **1218316**, page (2022)